Rydberg atoms for quantum simulation

Document status and date:
Published: 27/11/2020

Document Version:
Publisher's PDF, also known as Version of Record (includes final page, issue and volume numbers)

Please check the document version of this publication:

• A submitted manuscript is the version of the article upon submission and before peer-review. There can be important differences between the submitted version and the official published version of record. People interested in the research are advised to contact the author for the final version of the publication, or visit the DOI to the publisher's website.
• The final author version and the galley proof are versions of the publication after peer review.
• The final published version features the final layout of the paper including the volume, issue and page numbers.

Link to publication

Rydberg Atoms for Quantum Simulation

PROEFSCHRIFT

ter verkrijging van de graad van doctor aan de Technische Universiteit
Eindhoven, op gezag van de rector magnificus, prof. dr. ir. F.P.T. Baaijens,
voor een commisie aangewezen van het College voor Promoties in het
openbaar te verdedigen op vrijdag 27 november 2020 om 13:30 uur

door

Rasmus Vestergaard Skannrup

geboren te Skanderborg, Denemarken

Dit proefschrift is goedgekeurd door de promotoren en de samstelling van de promotiecomissie is als volgt:

Voorzitter: prof.dr.ir. G.M.W. Kroesen
1^e promotor: dr.ir. S.J.J.M.F. Kokkelmans
Copromotor: dr.ir. E.J.D. Vredenbregt
Leden: prof.dr. A. Fiore
                  prof.dr. K. Mølmer
                  prof.dr. T. Lange
                  dr. R.J.C. Spreeuw

Het onderzoek of ontwerp dat in dit proefschrift wordt beschreven is uitgevoerd in overeenstemming met de TU/e Gedragscode Wetenschapsbeoefening.

Rydberg Atoms for Quantum Simulation

Front cover: Wavefront on the surface of a placid lake due to a small stone. When the stone impacts the water's surface, water is ejected and creates both droplets flying away as well as this beautiful wavefront, reminiscent of a trilobite Rydberg wavefunction. Water waves are of course well known, but here the waters surface is excited to a very high degree, and we see a phenomenon that seems to defy common sense. So exactly the same concept as Rydberg physics, we might understand small excitations and have intuition on how it works, but high excitation leads to exciting new physics. Photograph by Thomas Jensen and Rasmus Vestergaard Skannrup.

"

There is a theory which states that if ever anybody discovers exactly what the Universe is for and why it is here, it will instantly disappear and be replaced by something even more bizarre and inexplicable...

Douglas Adams

"

Summary

As a topic, quantum simulations and computing has been around since the 1980's, but recent years have seen a lot of progress towards the development of actual physical quantum devices. This thesis provides an introduction to quantum computing for the layman as well an overview of the current state and near future of the field. This future will be dominated by so-called NISQ devices, noisy quantum devices that are able to provide the insights and experience needed for the eventual development of fault tolerant universal quantum computers. The thesis explains in some detail why the universal quantum computer is to physicists, what the sirens' song were to Odysseus, a luring call, promising a future so bright and so plentiful that no man can resist it.

The thesis continues in the following chapter by delving into the realm of Rydberg physics *i.e.* the physics of highly excited atoms. Here core concepts such as scaling relations, interactions blockade, facilitation and crystallization are explained using toy models and minimal examples. This chapter also provides introductions into some of the methods used in conducting the research behind this thesis, namely stochastic variation and Monte Carlo simulation. While these methods are perhaps well known to some, the treatment here is specific to the following chapters.

Chapters 3 and 4 are primarily concerned with theoretical treatment of constructing quantum hardware, *i.e.* physical objects that can perform quantum simulation or quantum computation. These chapters show that it is theoretically possible to confine spatially extended Rydberg atoms in very tight magnetic traps and that it is possible to make such trapped Rydberg atoms interact via phonons in a way, which is directly analogous to the interaction between ions in the well established Mølmer-Sørensen gate. These results are useful as an offset for future research, since they hold the promise of scalable quantum devices with small dependence on the temperature of the quantum hardware, thereby reducing system noise and improving the quality of the quantum operations performed.

Chapters 5 and 6 are primarily concerned with characterizing systems that we want to investigate in a full quantum simulation but are also simple or simplified enough that we can make predictions on the quantum behavior of the systems. These papers predict the quantum behavior of Rydberg atoms excited in geometries with reduced dimensionality. These chapters make predictions on a variety of different phenomena, such as crystalization, the quantum Debye length and insulator conductor crossover, which could be investigated using quantum simulation.

Future research into this topic, based on the contents of this thesis, will hopefully cooperate and experimentally validate the results presented here. The fields of quantum simulation and computing are in rapid development and much progress

towards demonstrating quantum supremacy has been made during the time of work on this thesis. The future is bright and perhaps quantum devices are just around the corner, ready to change the fundamentals of computation in ways, we cannot even imagine, yet.

Contents

Entering the Age of Quantum Simulation and Computing

In the late 1800's physics seemed to many a completed discipline, with the only improvements being in precision. However the theory was, in the words of Lord Kelvin, obscured by two clouds [Tho10]. One, the constant speed of electromagnetic waves predicted by Maxwell's equation, led to Einstein's theories of relativity. The other, the so-called ultraviolet catastrophe, was solved by Max Plank and led to the development of quantum mechanics. Problems in quantum mechanics are notoriously difficult to solve and only a few problems can be solved exactly or by hand.

Various methods have been developed to approximately solve complex quantum problems such as perturbation theory and the variational principle, but even solving these approximated problems can be prohibitively difficult. Exact simulations with all degrees of freedom included are limited to describe a few quantum particles in full detail. Usually we reduce the complexity of the problem by truncating state space, reducing the number of effective degrees of freedom, applying mean field theory or using semi-classical approaches, where only certain parts of the problem are solved within the quantum formalism and the rest is treated classically.

These methods have been developed over many years and have historically been very successful, but for some quantum systems, especially the strongly correlated systems, the classical computational resources are insufficient to keep up with the exponential scaling in the degrees of freedom of the required resources. For such systems, we have no useful description and thus understanding. Often these systems are of extreme interest both from a technological/application viewpoint, but also on a fundamental level of understanding.

Luckily, the way forward has been laid out in the 1980's, where Richard Feynman claimed (1982) that in order to simulate quantum systems, we need a device, which does not only simulate the rules of quantum mechanics, but obeys them; a quantum simulator [Fey82]. Such a device, developed to efficiently solve a specific quantum mechanical problem, has a Hamiltonian, which can be tuned to model a variety of related model Hamiltonians, too complicated to currently be simulated. Such systems can be a stepping stone to solve a wide range of outstanding quantum problems, like high T_c superconductors or protein folding.

1.1 Quantum computing for the layman

Devices to aid computation have been made since ancient times, with some of the earliest examples (apart from fingers or other body parts) including the abacus and, of course, the Antikythera Mechanism, by some considered the world's oldest

(analogue) computer, from around 100 BCE [Fre06]. In Europe devices of such complexity were not seen again until the late Middle Ages. The Antikythera Mechanism, however, was nowhere near a Turing complete programmable computer that honour is usually given to Charles Babbage's Analytical Engine proposed in 1837 [GC10, Cop17]. This all mechanical machine was never built (there are, however, ongoing efforts) and the programmable computers would not be realized until the first digital computers were conceptualized by Alan Turing [Tur37] and built in the first half of the 20th century [Cop17]. Even if Babbage's Analytical Engine had been built the first digital computer was not only more powerful, but also cheaper and smaller. The advent of digital computers was made possible by the preceding development of the vacuum tube. Later the transistor and integrated circuits made vacuum tubes obsolete and today's digital computer is millions of times as powerful as the first computers. Today we are entering a new era. Hopefully, once again we will be able to construct devices that are millions of times more powerful than those currently available, at relatively low cost and size, namely quantum computers.

To understand why quantum computers will potentially improve our computational capabilities, it is important to first understand the limitations of current computers, which we shall call classical computers henceforth. On the most basic level, the inner workings of a classical computer are essentially just switches, known as transistors. Currents going through these transistors represent the data, in units called bits, and are either turned off, denoted by 0 or turned on, denoted by 1. Classical computers use these switches to perform three logical operations on the bits, one is a single bit operation, which negates a single bit, ie. changing its value from 0 to 1 or vice versa, called the NOT-gate. The two other operations are two bit operations, they output one bit for two input bits. One gate, called the AND-gate for obvious reasons, takes two inputs, each having a value of either 1 or 0, and outputs the value 1 if and only if both inputs have value 1, otherwise the output value is 0. The other gate, called the OR-gate, outputs value 0 if and only if both inputs have value 0, otherwise the output value is 1. In reality, computer chips only implement one type of logic gate, a so-called universal gate, since any of the three logic gates can be broken down into sequences consisting entirely of either NAND (not-AND) gates or NOR (not-OR) gates [Raj11]. This is known as NAND-logic or NOR-logic respectively, and has the benefits of smaller and faster circuits [Raj11].

A quantum computer, on the other hand, works with so-called qubits, which obey quantum mechanical rules. This means that we have to adapt our notation

$$0 \rightarrow |0\rangle$$
$$1 \rightarrow |1\rangle. \tag{1.1.1}$$

Do not worry about the meaning of "|" and "⟩". It is simply how we tell that something is a quantum property, and not just a number, we call this notation a ket and the reverse ⟨ | a bra. We need to distinguish the notation of the state from the binary value it represents, since a qubit is not restricted to one of these qubit states[1], but (can) have a fraction of each, known as a superposition state. We

---

[1]In this chapter, "qubit state" means $|0\rangle$ or $|1\rangle$, not the (general) state of the qubit.

write such a superposition state like this

$$|\psi\rangle = a_0|0\rangle + a_1|1\rangle \qquad (1.1.2)$$

where a_0 and a_1 are complex numbers satisfying the condition $|a_0|^2 + |a_1|^2 = 1$, called coefficients. The numbers are complex since the superposition is not just some fraction of each qubit state, but the different components can have different phases, meaning that the coefficients do not have to add up to any specific number or even a real number. When we perform a quantum algorithm, and want to know the result, we have to measure what state the qubit is in. And this is where the proverbial shoe pinches. If we imagine a quantum algorithm, with ψ from eq. (1.1.2) as its output state, and measure the qubit to figure this out, the state collapses to either $|0\rangle$ or $|1\rangle$, and we only ever get one of these two answers. If we do this many times, we can figure out the probability of getting $|0\rangle$, which is $|a_0|^2$. (Of course this also works for finding the probability of getting $|1\rangle$.) So what is all the fuss about? What can a quantum computer do that a normal computer can't?
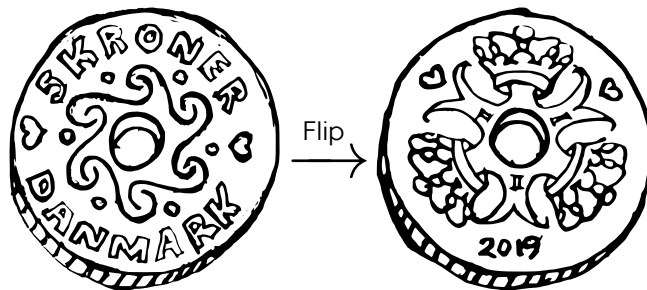
Figure 1.1: *Heads (left) and tails (right) of a Danish 5 kroner coin. Flipping the coin changes the side facing up from heads to tails or vice versa.*

To answer this, let us make an example. Imagine a game you play against a friend, where your friend hides a coin in a box and the two of you now take turns at either flipping the coin or not, see Figure 1.1, or not flipping the coin without the other knowing, whether the coin is flipped or not. After you both have had the chance to flip the coin, you open the box and see who won; heads: your friend wins, tails: you win. It is easy to see that you both have a 50% chance of winning, see Table 1.

Table 1: Outcome of coin flip game, "H" is heads, "T" is tails, "F" denotes a flip and "-" no flip. The outcome is half heads, half tails.

Initial	H	H	H	H	T	T	T	T
Your move	F	F	-	-	F	F	-	-
Friends move	F	-	F	-	F	-	F	-
Outcome	H	T	T	H	T	H	H	T

So far, so good; a computer can easily model this, and indeed you can design a computer program to play this game fairly, with the coin being modelled by

a single bit. But if your friend is unsatisfied with his odds, he might want to try something different, like a quantum coin, where you could model the coin with a qubit.

This does not change the rules of the game or, in itself, the probabilities of the different outcomes. Let us say that if the quantum coin is heads, the qubit state is $|0\rangle$ and if the quantum coin is tails, the qubit state is $|1\rangle$. Flipping the quantum coin is no different from flipping the regular coin, see Figure 1.1

$$|0\rangle \xrightarrow{\text{Flip}} |1\rangle$$
$$|1\rangle \xrightarrow{\text{Flip}} |0\rangle. \tag{1.1.3}$$

However, your friend is both sneaky and acutely aware of the possibilities of the quantum world, and he places the quantum coin, not in one of the two qubit states, but in a superposition of them

$$|\text{Coin}\rangle = \frac{1}{\sqrt{2}} (|0\rangle + |1\rangle), \tag{1.1.4}$$

by means of something called a Hadamard operation. Think of it like putting the coin on its edge, see Figure 1.2, but keep in mind that the outcome is dependent on what axis you rotate the coin around. If you try to flip this state

$$|\text{Coin}\rangle = \frac{1}{\sqrt{2}} (|0\rangle + |1\rangle) \xrightarrow{\text{Flip}} \frac{1}{\sqrt{2}} (|1\rangle + |0\rangle) = |\text{Coin}\rangle, \tag{1.1.5}$$

it does not change, and no matter what you do, see Figure 1.2, and your friend can simply turn the quantum coin to heads, using the same Hadamard operation. Now, if you try to look if your friend has placed the quantum coin in the superposition state, it collapses into one of the two qubit states (think of it as the coin falling over, see Figure 1.2), and you will see heads half the time and tails half the time. So you cannot detect, whether your friend is cheating or not except, of course, that he wins all the time.

While, perhaps, a bit frivolous in terms of effort spent to win a simple game, this illustrates a key difference between a classical computer and a quantum computer. The ability to put the qubit in a superposition state, and thereby change the rules of the game, is the strength of the quantum computer. The quantum computer can create and carry out algorithms on superposition states, without collapsing the superposition state into one of the qubit states. However, the quantum computer has one more trick up its sleeve. This trick is, of course, also founded in quantum mechanics and has to do with how we treat multiple qubits. If we have two qubits, each of them can be in the $|0\rangle$ or $|1\rangle$ qubit state, or in a superposition state. We write the two-qubit state, with the two qubits being in states $|\psi_1\rangle = a_0|0\rangle + a_1|1\rangle$ and $|\psi_2\rangle = b_0|0\rangle + b_1|1\rangle$ as a so-called product state

$$|\Psi\rangle = |\psi_1\rangle \otimes |\psi_2\rangle = a_0 b_0 |00\rangle + a_1 b_0 |10\rangle + a_0 b_1 |01\rangle + a_1 b_1 |11\rangle, \tag{1.1.6}$$

where a_0, a_1, b_0 and b_1 are complex numbers satisfying $|a_0|^2 + |a_1|^2 = 1$ and $|b_0|^2 + |b_1|^2 = 1$. The symbol $\otimes$ merely means that we take two different things and combine into one. You can think of it a bit like taking a street name and house

4
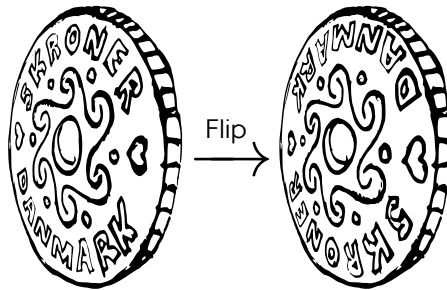
Figure 1.2: *Danish 5 kroner coin placed on its side. In contrast to Figure 1.1, 'flipping' the coin now rotates the coin around an axis perpendicular to the obverse and going through the centre of the coin. This only changes the orientation of the coin, but not the direction the heads side of the coin faces. Moreover, the coin is placed in an unstable equilibrium, any disturbance will make it fall over and show one of the sides at 50-50 probability.*

number and combine them into an address. However, to avoid unnecessary complication of the notation, we will mostly use the notation where the two-qubit states are in the same bracket "$| \ \rangle$", rather than the $\otimes$-notation, see Table 2.

Table 2: The four states describing a system of two qubits with individual qubits in the single qubit states.

$\otimes$	$|0\rangle$	$|1\rangle$
$|0\rangle$	$|00\rangle$	$|01\rangle$
$|1\rangle$	$|10\rangle$	$|11\rangle$

It is important to note here that the number of two-qubit states is not two, but four. You would need four classical bits to describe a two-qubit state. If we introduce a third qubit, we get eight three-qubit states $|\Psi\rangle \otimes |\psi_3\rangle$, two for each of the two-qubit states, by combining it with either $|0\rangle$ or $|1\rangle$, and this trend continues. If you want to model N qubits on a classical computer, you need 2^N complex coefficients, each stored in a number of classical bits, quickly reaching a number so big that no classical computer could ever possibly model the system, when N gets large.

Just like in the single qubit case, the two-qubit system can also be brought into a superposition of the two-qubit states from Table 2. As an example, consider such a two-qubit superposition state

$$|\Psi\rangle = \frac{1}{\sqrt{2}} \left(|00\rangle + |11\rangle \right), \tag{1.1.7}$$

which is fundamentally different from the state described in eq. (1.1.6). No matter the choice of a_0, a_1, b_0 or b_1 we can never construct this state as a product of two superposition states, but only as a superposition of two product states. We call such a state an entangled state.

Having seen what a quantum computer can do, it is also important to understand what it can not do. A common misconception is that a quantum computer can

calculate everything at once, since you just input a superposition state of all possible input. Without going into detail on whether this is at all feasible or whether the outcome would be a superposition of all answers, this would not speed up calculation in a sort of super-parallelization, since the output state would collapse upon measurement, and we would only get a single answer. Just like on a classical computer.

Instead, a quantum computer can apply quantum logic gates, like the Hadamard operation in the example with the coin flip game, which are unitary quantum operations, to the qubits. These quantum counterparts of the classical logic gates, ideally, preserve the quantum nature of the qubits and do not collapse the superposition states or break entanglement, unless needed. However, since the number of quantum gates is much larger than the three classical logic gates, it is impractical to implement every single possible quantum logic gate. Luckily, we draw inspiration from the NAND- and NOR-logic of the classical computer, where the usual implementation only makes use of one of these so-called universal logic gates, which can be combined to make all three basic logic gates.

A similar set of universal quantum gates can be chosen for the quantum computer, since any unitary quantum operation can be decomposed into a series of two-level unitary operations [Bar95], i.e. operations, which only act on two of the multi-qubit states. Such a set is not unique, but a common example consists of the C-NOT, Hadamard and $\pi/8$ gates [Nie11]. This is sometimes known as C-NOT logic. Several approaches to constructing a C-NOT gate have been developed, but possibly the best was proposed by Mølmer and Sørensen [Sø99, Sø00] for ions; an atomic version of this is described in chapter 4.

The Hadamard gate, which we made a brief acquaintance with earlier in the coin flip game, creates superposition states from single qubit states and vice versa

$$a_0|0\rangle + a_1|1\rangle \xrightarrow{\text{Hadamard}} \sqrt{\frac{1}{2}}\Big((a_0 + a_1)|0\rangle + (a_0 - a_1)|1\rangle\Big). \qquad (1.1.8)$$

The $\pi/8$-gate gives a complex phase to the $|1\rangle$ part of the state

$$a_0|0\rangle + a_1|1\rangle \xrightarrow{\pi/8} a_0|0\rangle + e^{i\pi/4}a_1|1\rangle. \qquad (1.1.9)$$

Sometimes, an additional gate, called the phase gate, is included in the universal set, due to its importance in fault tolerant implementation, but since it is equivalent to applying the $\pi/8$ twice, we will not go into further detail here. Finally, we have the C-NOT gate, which takes two qubits and changes the state of one depending on the state of the other

$$a_{00}|00\rangle + a_{01}|01\rangle + a_{10}|10\rangle + a_{11}|11\rangle \xrightarrow{\text{C-NOT}} a_{00}|00\rangle + a_{01}|01\rangle + a_{11}|10\rangle + a_{10}|11\rangle. \qquad (1.1.10)$$

Applying these gates is what makes universal quantum computing powerful. We can approximate any unitary operation by a series of these universal operations, and hence implement quantum algorithms and explore the field quantum logic, where counterintuitive givens, result in counter-intuitive conclusions.

To recap, a quantum computer can take advantage of qubit superposition states as well as entanglement and apply algorithms that work on these without collapsing the superposition states or untangling the qubits. This allows the quantum

computer to perform its task with different rules from those applying for a classical computer. There is no known classical algorithm, which can efficiently model a quantum computer with a large number of qubits and we do not expect one to be found [Pre18]. The number of classical bits needed grows exponentially with the number of qubits, which means that we need a lot of computing power to (inefficiently) model a quantum computer with the algorithms of today. A quantum computer with around 50 qubits is at the edge of quantum supremacy, i.e. beyond what we can model on a classical computer [Pre18], and 100 qubits is past what we can hope to achieve with future classical computers just in terms of memory. All together this means that a quantum computer can perform tasks in a regime that no classical computer ever will be able to.

1.2   Noisy Intermediate-scale Quantum Era

So, where are we today? And where will we go in the next decade or so? In a 2017 keynote address [Pre18], John Preskill describes the near future of quantum computing, the so-called Noisy Intermediate-scale Quantum Computing (NISQ) era. This term covers quantum computer implementations, where we just have to live with noise in the system and accept that computations can fail or be unreliable and some can not be performed at all. The hope is that we can use the experience and knowledge we gain from these NISQ devices to construct a second generation of quantum computers that rely on a (large) number physical qubits to simulate a small(er) number of virtual qubits [Lom00, Chap. 3] along with quantum error correction [Ste96] to make them more reliable. So why is this an interesting concept? To answer the question, we must first understand, not only what a NISQ-device is, but also what the potential of NISQ-devices is.

 NISQ-devices are noisy devices, meaning that they are prone to influences from both inside and outside the quantum computer. Such influences will inevitably break the carefully constructed quantum entanglement the quantum computer relies on [Lad10, Pre18]. For quantum calculations, losing entanglement is equivalent to losing information, resulting in a breakdown of the entire computation. Isolation from outside influences are not all we worry about, though. We also have to consider how well we can control the quantum systems we use for qubits. Bad control of the qubits might result in errors due to imperfect operations or long operation times for quantum gates [Pre18]. Long operation times do not only slow down the quantum computation, making the whole exercise pointless, but can also lead to errors due to finite lifetime effects of internal qubit states. Imperfect operations, even with small errors, can build up over many gate operations, resulting in very large final errors for complicated programs. For quantum codes requiring a large number of qubits, each qubit will add to the error of the entire computation, limiting the number of qubits that can be successfully implemented and used in a device.

 A final source of errors come from the initialization and readout of the qubits [Pre18]. Not being able to fully trust that the questions we ask or the answers we get are transferred to and from the quantum device will reduce the trust in the answers we get, but does not make the NISQ device completely useless. By performing the same computation many times and statistically comparing the

answers, we can limit the effect of wrongful encoding or readout.

Apart from purely academic research, some of the big tech companies of the world, including Google [Dun18, Nei18], IBM [Har19, IMB, Qis], Intel in collaboration with QuTech [Fu18] and Microsoft [Aas16, Kar17] are leading in the development of the quantum computer. There are, though, many other types of qubits, some are at this point purely theoretical while others have been demonstrated in experiments or prototypes. As evident from the big-tech investments, both superconducting and topological qubits are very promising, but also ion- or atomic qubit devices show promise. Currently ion-qubit quantum gates, like the Mølmer-Sørensen gate [Sø99, Wan01, Sø00], which in chapter 4 is developed into an atomic version, show some of the highest fidelities, but are hard to scale up, due to the Coulomb interaction between the ions. Atomic qubit devices, like those based on Rydberg atoms [Bar16, Bro16, Jak00a, Lab16, Luk01a] show promise in their scalability, and are the focus of much academic research, including this thesis where chapter 3 treats magnetic trapping Rydberg atoms and chapters 5 and 6 treat their use in quantum simulation.

However, we must recognize that current state of the art quantum computers and devices (eg. [Hua19]) fall into the NISQ category [Lad10]. For now and the near future, it is all we have got. The goal of the NISQ-game is not to eliminate the noise, that dream is far off in the future, but to reduce it to a tolerable level, in tandem with making quantum error correcting code [Ste96] and devices [Lom00, Chap. 3]. We will just have to live with the noise for now, and accept the limitations that come with it.

1.2.1 Quantum supremacy

But, if NISQ-devices are so prone to error and are so hard to scale up, why not just skip the step? We can work with classical computers until a fault-tolerant quantum computer is ready. What is the gain? Well, fault-tolerant quantum computers are many years into the future [Pre18] and NISQ-devices might help us get there, both with experience and results. In fact, we have very few quantum algorithms right now, and NISQ-devices will be a development platform for such algorithms. Also, there is the scaling argument from Section 1.1, if you want to simulate N two-level quantum systems, you need 2^N classical bits. Thus we can never hope to simulate a, say 300 qubit quantum computer on a classical computer, since $2^{300} \approx 10^{90}$ is larger than the estimated number of atoms in the observable universe, meaning that even if every single atom in the universe was used for a classical bit, we would still run out of memory. We can simply never hope to simulate large quantum computers on classical computers, noisy or not. Today's largest supercomputers can simulate up to 48 qubits [Boi18], which means that even NISQ devices can go beyond the best classical computing has to offer.

We have defined the term 'quantum supremacy', to describe when quantum computers outperform classical computers [Geo14, Har17, Boi18, Pre18]. For a long time it was an open question, what quantum supremacy really means, but Harrow *et al.* [Har17] have set four requirements to experiments that show quantum supremacy

1. A well-defined computational task
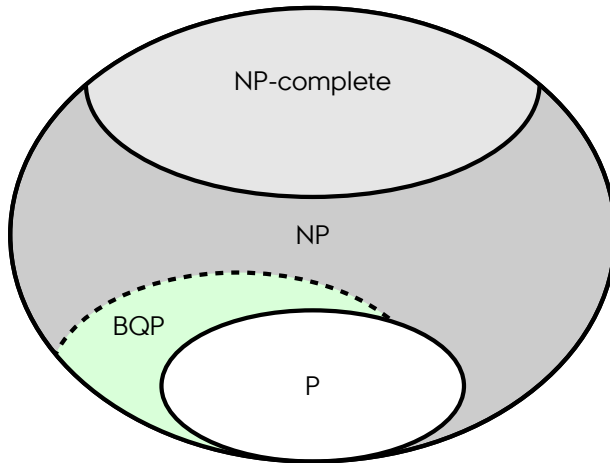
Figure 1.3: *Computational complexity groups. The group NP contains the problems, where we can easily check if an answer is right. Inside NP we have two subgroups that are completely contained within NP. The group P, which contains the problems that can 'easily' be solved on a classical computer, and the group NP-complete, which contains all the hardest problems in NP. It is an open question, whether all of these groups contain exactly the same elements. Further groupings exist outside of P, which contains problems like the games chess and go. With quantum computers we can expand the group of problems we can easily solve to the group BQP, which extends to some problems outside of NP, but probably does not contain any problems from NP-complete.*

2. A quantum algorithm, which can be run on near-term quantum devices (NISQs)

3. An amount of resources allowed to any classical competitor

4. An assumption from complexity-theory, supporting a quantum supremacy hypothesis in the given experiment

along with the optional requirement

5. A verification method that can easily distinguish the quantum algorithm from its classical competitors

The task need not be of any practical use except for showing quantum supremacy, which is, in its own right, a worthy goal [Pre18]. However, the task must be sufficiently hard that we can be confident that no classical computer can do it. Analogue quantum simulators can already outperform classical computers at simulating certain quantum properties [Che16, Har17], we are just not sure whether classical computers could perform better yet.

To make sure the classical computer will not outperform its quantum counterpart, in performing our test task, we need some computational complexity arguments that it is a hard task for any (hypothetical but realisable) classical computer.

Currently we think some problems are 'easy' for a computer to solve. Here easy means that the time it takes a computer to find the solution to the problem is a polynomial of the number of bits in the problem, so-called polynomial time. We call this group of problems P, see Figure 1.3. However, some problems are not apparently easy to solve and we suspect it is because these problems are hard. For some of the hard problems, we can easily check if a given solution is right, it is just difficult to find the solution. We call these problems NP. Over the years, some problems we thought were hard turned out to be easy, we just needed a good algorithm for solving the problem. Therefore it is an open question whether P and NP are actually the same group of problems or, as we suspect there are NP problems we can never solve easily. If it turns out that P and NP are indeed not the same, then we know that some of the problems not in P are harder than others. Among the problems in NP there is a subgroup, which we call NP-complete. A problem L in NP is NP-complete, if every problem in NP is reducible to L, *i.e.* if we have an algorithm solving L, this algorithm can be used as part of an algorithm solving every other NP problem. With quantum computers we can expand the group of problems we can easily solve to the group BQP, which extends to some problems outside of P, but probably does not contain any problems from NP-complete [Ber97, For99]. To prove quantum supremacy we therefore have to find a problem, which we believe is beyond the ability of even a hypothetical future classical computer, and show that a quantum computer can solve it with less resources.

Some proposals have been made for experiments that could, within reasonable time, show quantum supremacy [Har17, Boi18]. But for now, let us consider two of the more famous examples, though they are unlikely candidates to first demonstrate quantum supremacy.

Shor's algorithm

One of the problems from NP (but not NP-complete), which today we assume is beyond classical computers, is finding the prime factors of very large integers. This problem is so hard that we use it for encryption [Riv78]. Any integer N can be factored into prime numbers $2, 3, 5, 7, \ldots, p_i, \ldots$. This means that we can write N as the product of a finite number of primes

$$N = p_1 \cdot p_2 \cdots p_{\text{final}}, \tag{1.2.1}$$

where p_{final} is the final prime number. Each prime may be in the list several times or not at all. We call the numbers $p_1, \ldots, p_{\text{final}}$ the prime factors of N. Numbers with only one prime factor, which is necessarily the number itself, are prime numbers. Finding the prime factors of small integers, say $15 = 3 \cdot 5$, is easy [Van01], but the problem gets extremely difficult for large numbers with hundreds of digits [Van01]. An efficient, fully classical algorithm could be found in the future, but we think it is unlikely.

In 1994 Peter Shor published a quantum algorithm [Sho94, Sho99], which could easily find the prime factors of numbers, barred a few constraints. This algorithm, which has famously come to be known as Shor's algorithm, combines a classical part, which can be done on a classical computer, with a quantum period finding algorithm based on the quantum Fourier transform [Bea03], which requires the

use of a quantum computer. Shor's algorithm has been shown experimentally to work [Van01], albeit only to factor 15=3·5, which is still done with fewer resources on a classical computer. Nevertheless, it was an important demonstration of a working quantum algorithm, leading the way for further development of quantum algorithms. However, Shor's algorithm is not a good showcase for quantum supremacy, since according to [Har17], we would need around 4000 virtual or fault tolerant qubits to show quantum supremacy using Shor's algorithm. The impact of a large-scale implementation of Shor's algorithm on society would be enormous, as such an implementation would be able to break our currently most used encryption system, the RSA encryption [Riv78].

Grover's algorithm

Another quantum algorithm, which has achieved fame in the world of quantum information, is a database search algorithm by Lov Grover [Gro96, Gro99], known as Grover's algorithm. Grover's algorithm works by asking 'all questions at once' with a superposition state and then adjusting phases, such that successful queries reinforce each other while the others interfere randomly [Gro96]. However, it can only be used to find unique elements and requires the right formatting of the databases. There is not yet any efficient way to implement the quantum operations for making the right phase shift. Grover's algorithm also has the backing of experimental realization [Jon98].

Though Grover's algorithm also finds uses in cryptoanalysis [Kap16], the database search is still an illustrative example of a quantum algorithm. The algorithm can be explained in a few steps for searching a database with elements of size N bits, which can be encoded to a quantum system with N qubits and state-space dimension 2^N. We need a quantum operation C, which rotates the phase of the state we are seeking by π and the diffusion transform D, where the ij^{th} element is $D_{ij} = 2/N - \delta_{ij}$ (δ_{ij} is the Kronecker delta). Prepare N qubits on a quantum computer in the superposition state $|\psi_0\rangle = \frac{1}{\sqrt{2^N}}(|0,\ldots,0\rangle + |1,0,\ldots,0\rangle + |1,\ldots,1\rangle)$ and then apply the following steps on the order of $\sqrt{N}$ times [Gro97]

1. Apply the phase shift operation $|\phi\rangle = C|\psi_i\rangle$.

2. Apply the diffusion transform $|\psi_{i+1}\rangle = D|\phi\rangle$.

3. If $i = \sqrt{2^N}$ stop the iteration otherwise add 1 to i and go to point 1.

When the algorithm is performed, the most likely state to measure is the one corresponding to the object we seek, see Figure 1.4.

The example in Figure 1.4 shows the key feature of Grover's algorithm. Finding the right answer in a database search with more than 50 % probability would require, on average, 2^{N-1} lookups with a classical computer, but with Grover's algorithm we only need $2^{N/2}$ lookups. Therefore is of interest to tech-companies, such as Google [Nei18, Dun18], because it can possibly reduce the computer power needed for one of their main objectives, searching databases.

Recently papers claiming to prove quantum supremacy have been published [Aru19, Vil20], heralding the beginning of the quantum era. We have confidence that this will mean a huge step forward in our understanding of the world, partly
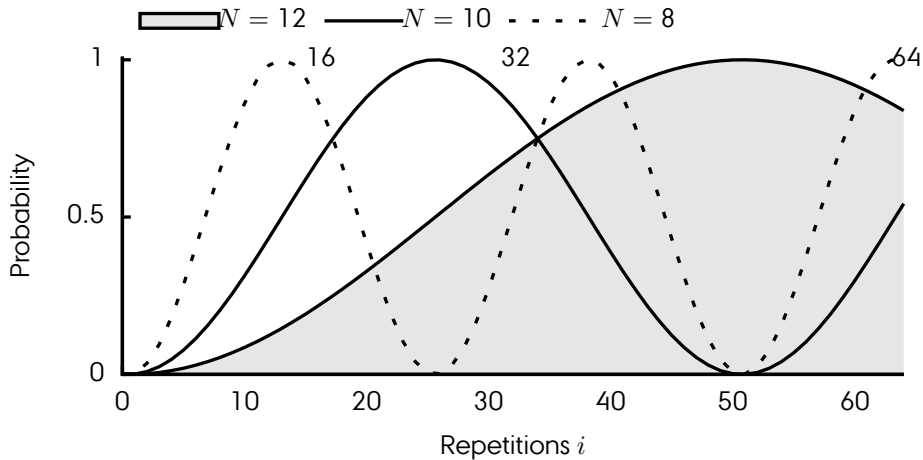
Figure 1.4: *Probability of getting the 'right answer' in a simplistic simulation of Grover's algorithm of databases of bit-sizes $N = 8$, $N = 10$ and $N = 12$. Labels mark $\sqrt{2^8}$, $\sqrt{2^{10}}$ and $\sqrt{2^{12}}$. The right answer is achieved periodically with the first occurrence showing up just before $\sqrt{2^N}$ repetitions. At $\sqrt{2^N}$ repetitions the probability is more than half, meaning that the right answer is more probable than all others combined.*

because quantum computers can simulate any local quantum system [Llo96] and we do not think classical computers can [Fey82]. Therefore, we have good reasons to expect that quantum computing will significantly increase the computational power available to humanity [Kan17]. A wide variety of technologies are being developed for quantum computation [Lad10], but they all have their faults and strengths, and none will be perfect from the start. It is the task of the NISQ-devices to demonstrate quantum supremacy and to serve as a testing bed for quantum algorithms. Classical computers have a 70-odd year head start, but quantum computers are gaining momentum and will in a few years time surpass their older cousins.

1.3   Types of quantum computing

Feynman's original claim from 1982 [Fey82] that quantum simulators can simulate any local quantum system has been shown to be correct [Llo96]. But quantum computers are not just quantum computers. Just like classical computers come in many flavours, like desktop, laptop, gaming console, calculator or server, depending on the specific tasks they are intended to do, so are quantum computers envisioned in many flavours.

1.3.1 Quantum simulation

In the lecture 'Simulating physics with computers' in 1981, the basis for [Fey82], Feynman made the argument that we can never hope to efficiently simulate quantum physics on classical computers. Instead, we would need a quantum computer, which operates according to the laws of quantum mechanics, and can exactly imitate any quantum system [Cir12, Geo14], by discretizing time and breaking each time step down to a series of quantum operations. We know from classical simulations and the great technological progress of society in general over the past 100 years or so that we often only need certain physical properties of a quantum system, such as densities, magnetization per lattice site, few-body correlation and phase diagrams [Cir12], to understand and develop a technology. A device, which does not make an exact replication of the quantum system but can give us a specific set of physical quantities, is what we call a quantum simulator.

To do this, we take a well-understood and controllable quantum system, initially described by a Hamiltonian $\hat{H}_{\text{sim}}$, and in the state $|\psi\rangle$, map the system we are interested in, described by Hamiltonian $\hat{H}$ with time dependent state $|\phi(t)\rangle$ onto the well-understood system

$$|\phi(0)\rangle = M|\psi(0)\rangle. \tag{1.3.1}$$

The time evolution of the system we want to simulate is described by the propagator

$$U = \exp\left[-i \int_0^t \hat{H} \, dt'\right], \tag{1.3.2}$$

and we find the state of the system at a later time by applying the propagator, which is a unitary transformation, to the state $|\psi(t)\rangle = U|\psi\rangle$. The idea is now to evolve the simulator, such that at the time steps of interest $t_1 \ldots, t_{\text{end}}$, the state of the simulator exactly maps back to the state we are looking for. We achieve this by applying a series of external influences, such as lasers and electric fields, in sequence. Each of these applications gives rise to a unitary transformation U_i and the state of the simulator at time t_i is given by

$$|\psi(t_i)\rangle = U_i \ldots U_1|\psi(0)\rangle, \tag{1.3.3}$$

where $U_1, \ldots, U_i$ are the unitary transformations due to the individual influences, and U_j propagate the system from time step t_{j-1} to t_j. This state can then be mapped back to the state of the system we are simulating

$$|\phi(t_i)\rangle = M^{\text{inv}}|\psi(t_i)\rangle, \tag{1.3.4}$$

where M^{inv} inverts the mapping.

The naïve way would be to apply the propagator of a system wide Hamiltonian $\hat{H}_i(t) = \hat{H}_{\text{sim}}(t) + \hat{H}_i'(t)$, including the Hamiltonian of the external influences $\hat{H}_i'(t)$, as the unitary transformation

$$U_i = \exp\left[-i \int_{t_{i-1}}^{t_i} \hat{H}_i(t') \, dt'\right]. \tag{1.3.5}$$

This is known as analogue quantum simulation and has been used to simulate Fermionic systems [Ger10, Geo14]. However, there is another way. If we, instead of system wide operators, have a fixed set of (universal) unitary operators $u_1, \ldots$ that only act on one or two qubits at a time, we call these quantum gates. Applying these quantum gates to specific qubits in the right finite sequence can then model the system wide operators (of Analogue quantum simulation)

$$U_i = u_{i_1} u_{i_2} \ldots u_{i_{\text{end}}}, \qquad (1.3.6)$$

where the subscripted i's takes a predetermined sequence of u_j's. This way is more versatile than the analogue version [Cir12] and we call it digital quantum simulation [Geo14]. In reality, we also consider multi qubit quantum gates for digital quantum simulation, as we can often reduce the number of operations needed to execute an algorithm. Both analogue and digital quantum simulators have been realized [Ger10, Lan11, Geo14] and other platforms for quantum simulation have been proposed or are in development [Geo14] including platforms based on Rydberg atoms [Saf10a].

1.3.2 Universal quantum computers

The digital quantum simulator is a remarkable device and in many ways mirror the workings of a digital classical computer, but it begs the question 'What will we need to solve other problems like applying Shor's algorithm?'. The answer is a Turing complete quantum simulator, a fully programmable version of the digital quantum simulator, capable of performing any quantum algorithm we give it [Deu85]. We call this a universal quantum computer.

To go from a digital quantum simulator to a fault-tolerant universal quantum computer, the device must fulfil the five DiVincenzo criteria [DiV00]

1. Scalability with a well-characterized qubit.

2. The ability to confidently initialize to a simple state.

3. Coherence times much longer than the gate operation time.

4. A finite universal set of quantum gates.

5. A qubit-specific measurement capability.

However, since the original publication of these criteria, quantum computing has come a long way and quantum computer implementations today are error-correcting like NISQs [Pre18]. The third DiVincenzo criteria is therefore of less concern and the rest can be rephrased, keeping decoherence 'small enough' [Lad10]. The main concerns for quantum computer implementations are then scalability and fidelity of the quantum gates with error-correcting initialization and read-out [Lad10]. As long as the error-rate in the quantum computer operation is beneath a certain limit, we can use quantum error-correction [Lad10]. The error-rate can be kept low by use of virtual qubits [Pre18], but this presents a new challenge as the number of physical qubits needed grow very fast with respect to the number of available virtual qubits [Pre18], greatly reducing scalability.

A number of platforms that promise to deliver universal quantum computing have been developed [Lad10], with big tech companies in the lead. Google leads research into superconducting qubits program [Dun18, Nei18] and in October 2019 claimed to have demonstrated quantum supremacy [Aru19] on their 53 qubit Sicamore chip. IBM also develops superconducting qubit quantum computing [Har19] with a special focus on developing quantum algorithms through their Qiskit [LaR19], which is open to all [IMB, Qis]. Microsoft collaborates with the university of Copenhagen, Denmark on topological qubits [Aas16, Kar17], which show some promise in being particularly resistant against loss errors due to the environment. Perhaps the future of quantum computing lies down the same path as classical computers in silicon quantum gates, as single qubit silicon quantum gates have exceeded fidelities of 99.9% and two-qubit silicon quantum gates have reached fidelities of 98% [Hua19]. The Intel/QuTech collaboration is currently looking into this type of qubit along their existing research on superconducting qubits. However, the fully programmable quantum computer is still a distant dream [Pre18].

1.3.3 Other methods

Other types of quantum computing exist with experimental backing, like the variational quantum eigensolvers [Kan17] (VQE) and the quantum annealing.

VQEs are hybrid approaches, used to study a quantum system described by the Hamiltonian $\hat{H}$. A quantum simulator is used to prepare a variational trial state $|\psi_\alpha\rangle$ dependent on the set of parameters α and the expectation value of an operator $\hat{O}$ is found $E_\alpha^O = \langle\psi_\alpha|\hat{O}|\psi_\alpha\rangle$ and used in a classical optimizer to find an improved set of parameters α', which can be fed into the quantum computer for the next trial state [Per14, McC16, Kan17]. Among the advantages is the ability to prepare trial states beyond what purely classical methods are capable of [Kan17], while significantly reducing the need for coherent evolution compared to the fully quantum methods [Per14, McC16].

The other type, quantum annealing, is closely related to the classical technique of simulated annealing [Fin94], useful for finding global minima of multivariate functions. Both rely on the concept of thermal annealing, where the density of configurations of a cooling system tends to condensate at the lowest potential energies. Simulated annealing treats the problem as fully classical and lowers the temperature of the model slowly to find the global minimum. Quantum annealing, on the other hand, treats the problem at zero temperature and slowly increases the mass of the system, thereby effectively turning off the quantum mechanical spread of the energy, which condensates at the lowest configuration [Fin94]. Perhaps the most famous implementations of quantum annealers are the D-Wave 1 and D-Wave 2 commercial quantum computing devices by the Canadian company D-Wave Systems, although the quantum nature of these devices has been brought into question [Shi14, Alb15].

1.4 Contents of this thesis

This thesis contains eight chapters of which the first two cover the techniques and concepts behind the research reported in the following four chapters. Chapters

three through six contain papers written by the author and various collaborators. Each chapter contains one paper, which is published in or submitted to a peer review journal.

 Chapter 1 is this chapter and provides an introduction to quantum computing, intended for a layman that is a person with no prior knowledge of quantum mechanics or quantum computing, as well as an overview of the current state of development of quantum computers and simulators.

 Chapter 2 contains a summary of the concepts and methods that have been used in the research behind the following chapters. There is a general introduction to Rydberg atoms including wavefunctions, excitation, scaling relations, interactions and blockade/facilitation phenomena. This chapter also explains the basics of stochastic variation, time-evolution and Monte Carlo simulation in some detail. Stochastic variation on correlated Gaussians is used in chapter 6 to find upper bounds on the energies in a one dimensional Coulomb system. This method provides the means of finding approximate ground states of quantum systems without being particularly demanding in computer resources. Coherent time-evolution describes the time dependence of well-isolated quantum systems and is used in chapter 4. For systems where the time dependence of the system is not completely governed by the Schrödinger equation like in chapter 5, incoherent time-evolution is used. Here the master equation describes the time dependence of the system and it is possible to treat finite life times and external influences on the system. Monte Carlo methods can be applied to find time dependent statistical information on a quantum system. The system is randomly realized many times over and the averages of these realizations are taken to describe the system. This technique is used in chapter 5. The final section is a short explanation to diffraction light shaping with spatial light modulators in mind. Shaped light is an important component in the experimental work reported in chapter 5.

 Chapter 3 is published in Phys. Rev. A 97 [Boe18] and theoretically explores the possibility of confining Rydberg atoms in tight magnetic microtraps. The trapping frequencies for Rydberg atoms are expected to be influenced strongly by magnetic-field gradients. The chapter shows that there are regimes where Rydberg atoms can be trapped. Moreover, it is shown that so-called magic trapping conditions can be found for certain states of rubidium, where both Rydberg atoms and ground-state atoms have the same trapping frequencies. Magic trapping is highly beneficial for implementing quantum gate operations that require long operation times.

 Chapter 4 studies the possibility of creating phonon-mediated spin-spin interactions between neutral atoms trapped in optical tweezers in theory. By laser coupling the atoms to Rydberg states, collective modes of motion appear. The chapter shows that these can be used to mediate effective spin-spin interactions or quantum logic gates between the atoms in analogy to schemes employed in trapped ions. In particular, the chapter employs Rydberg dressing in a novel scheme to induce the needed interaction, and it is shown that it is possible to replicate the working of the Mølmer-Sørensen entanglement scheme. The Mølmer-Sørensen gate is widely used in emerging quantum computers using trapped ion qubits and currently features some of the highest fidelities of any quantum gate under consideration. Arbitrarily high fidelity for the coherent time evolution of the two-atom state even at non-zero temperature is shown.

Chapter 5 investigates formation of structures of Rydberg atoms excited from a disordered gas of ultra-cold atoms, using rate equations for two-photon Rydberg excitation in a single atom without eliminating the intermediate state. The chapter explores the validity range of these rate equations and defines a simple measure to determine whether our model is applicable for a given set of laser parameters. These rate equations are applied in Monte Carlo simulations of ultra-cold gases, for different laser beam profiles, and the results of these simulations are compared to experimental observations, where we find a general agreement.

Chapter 6 investigates how Rydberg atoms can be used to simulate quantum plasmas and insulator-conductor crossovers. Starting from a one dimensional Rydberg crystal, the electrons will, if excited highly enough, have enough kinetic energy to pass through the potential barrier between the atoms, and the system can transition into an ordered quantum plasma. Using a 1D model we find crossovers between insulators and conductors and quantum plasma states, as well as universal scalings of the lengths and energies, dependent on principal quantum number n.

In chapter 7 I would like to say a few words on the process of making this thesis and express my gratitude to the people who helped make it a reality.

2

Background for this thesis

The papers included in this thesis all cover the subject of Rydberg atoms used for quantum simulation. This requires a variety of techniques and, of course, a good background knowledge of Rydberg atoms. In this chapter, we will go over the basics of Rydberg atoms and the employed techniques in some detail.

2.1 Rydberg atoms

Rydberg atoms are atoms where one electron is excited to a very high principal quantum number n, usually we talk about Rydberg atoms when $n \gtrsim 30$. These highly excited atomic states are now found in labs around the world, but are also found in the interstellar medium [Gne09]. Rydberg atoms have been studied for their fascinating behaviour and strong scaling for many years [Ste76, Zim79, Gal94]. The last decade, though, has seen a renewed and unrivalled interest, due to both advances in experimental techniques and theoretical work, covering the application of Rydberg atoms in quantum information [Jak00a, Luk01a], quantum sensing [Car12, Deg17], exploring exotic quantum phases in many body systems [Qia13] and strongly correlated systems [Urv15], due to the strongly scaling dipole-dipole interactions. Especially the promise of applications in quantum information is interesting, for the reasons outlined in chapter 1.

The definition of 'highly excited' is, however, somewhat vague, as for most atomic species we have to consider which electron gets excited and what the consequences are. Much research focuses on atoms of alkali metals (lithium, sodium, potassium, rubidium, caesium and francium) [Noe00, Bet15, Bet09, Sin05, Kru02, The84, Mit03, Saf10a], as alkalis in general are best suited for laser cooling [Saf10a], but some researchers excite Rydberg ions from (singly ionized) alkaline-earth metals (Beryllium, Magnesium; Calcium, Strontium, Barium and Radium) [Mit03, McQ13, Lan91] or even Rydberg molecules [Bel13, Lv16]. The alkalis have the benefit of having only a single electron in the outermost shell, which is also the only enclosed shell in the atomic electron structure. This makes for relatively simple electronic structures, which can, in general, be described using quantum defect theory [Mar94, Sea83, Li03][Bra03, chap.9.4], where only small modifications to the hydrogen theory are necessary to explain these larger systems. That is, their energy levels follow the Rydberg formula with only minor modifications

$$E_{nlj} = -\frac{\text{Ry}^*}{n^{*2}} = -\frac{\text{Ry}^*}{(n - \delta_{nlj})^2}, \tag{2.1.1}$$

where Ry^* is the species specific Rydberg constant and δ_{nlj} is a state specific parameter, known as the quantum defects. The quantum defects are to a large
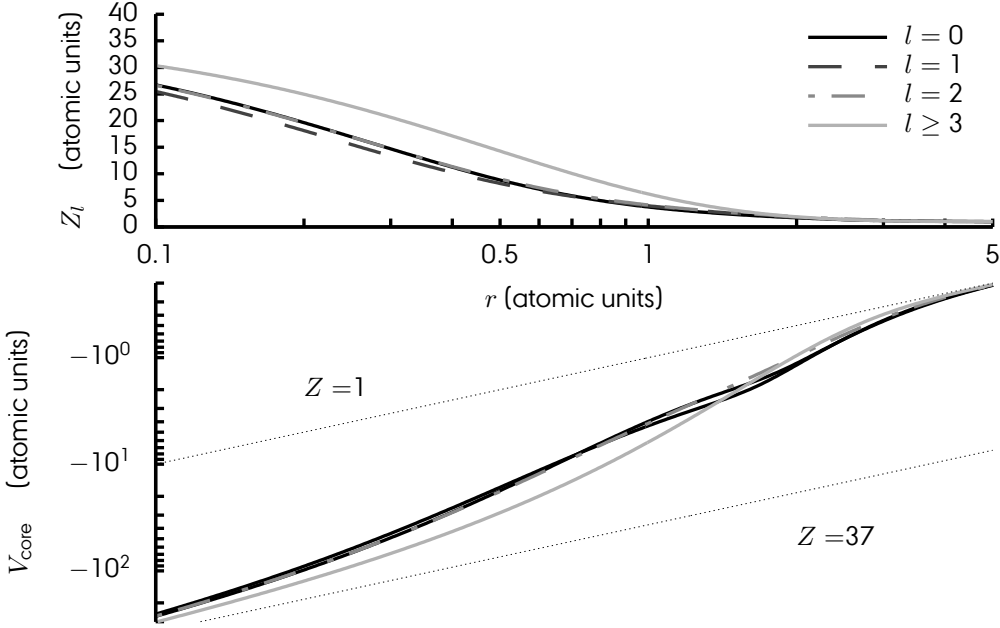
Figure 2.1: *Space charge distribution from the core of an rubidium atom as experienced by the valence electron in a given orbital angular (l) state (top), see eq. (2.1.4), and the resulting potential V_{core} (bottom), see eq. (2.1.3), with guides corresponding to Coulomb potentials with charges 37 and 1.*

extent only dependent on the orbital angular quantum number l [Bra03, chap.9.4] but can be more accurately determined by

$$\delta_{nlj}(n) = \delta_0 + \frac{\delta_2}{(n-\delta_0)^2} + \frac{\delta_4}{(n-\delta_0)^4} + \dots, \qquad (2.1.2)$$

where $\delta_0, \delta_2, \dots$ are dependent on l and j and must be determined from experiment, see for example [Li03].

To determine the wave functions of the outermost electron, commonly referred to as the Rydberg electron, subject to the combined electric potential of the nucleus and remaining (core) electrons, together called the (ionic) core, we use the model potential (in atomic units, which will be used throughout this thesis unless otherwise indicated)

$$V_{core} = -\frac{Z_l(r)}{r} - \frac{\alpha_c}{2r^4}\left(1 - e^{-(r/r_c)^6}\right), \qquad (2.1.3)$$

proposed in [Mar94] (see Figure 2.1) or alternatives like the one in [Gre91]. The first term in eq. (2.1.3) describes the Coulomb interaction between the Rydberg electron and the left-over charge of the nucleus, the so-called unshielded charge;

20

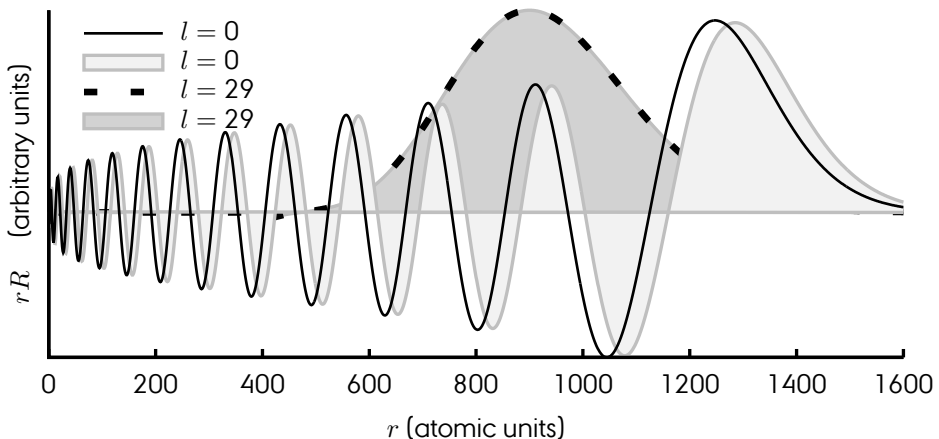Figure 2.2: *Numerical solutions to the radial Schrödinger equation at $n = 30$ and $j = l + 1/2$ using the potential V_{core} from eq. (2.1.3) (filled grey) compared to their hydrogenic counterparts (black). At low angular momentum ($l = 0$) the solutions differ significantly, and we have to take the spatial extent of the core into account. At maximal angular momentum ($l = 29$) the two solutions are practically identical.*

we will go over the spatial distribution of this in a moment. The second term in eq. (2.1.3) deals with the polarisability of the ionic core, α_c is the static polarisability of the core and r_c is a cut-off distance, both must be determined from experiment. Most of the nuclear charge is shielded by the core electrons, but the remaining unshielded nuclear charge is described by

$$Z_l(r) = 1 + (Z - 1)e^{-a_1 r} - r(a_3 + a_4 r)e^{-a_1 r}, \tag{2.1.4}$$

where Z is the total nuclear charge and the l-dependent constants $a_1, ..., a_4$ are determined from experiment, see [Mar94] and Figure 2.1.

In Figure 2.1 the unshielded charge Z_l (top) and the model core potential V_{core} (bottom) have been plotted for rubidium, with constants taken from [Mar94]. At $r = 0$ the Rydberg electron experiences the full nuclear charge, which is shielded at larger distances, and at $r = \infty$ the Rydberg electron experiences the core as a point elementary charge. Although there is a dependence on orbital angular momentum l in the unshielded charge and potential, this does not represent any practical difficulties [Mar94]. The model potential V_{core} shows some dependence on l, but when the centrifugal barrier term of the kinetic energy ($l(l+1)/r^2$) is taken into account, this will be the dominant term in the region, where the potential is strongly l-dependent ($r \lesssim \sqrt{l(l+1)}$). Figure 2.1 shows that the model potential quickly approaches the Coulomb potential of a single elementary point charge for $r \geq 5$.

21

This results in the Hamiltonian (in atomic units)

$$\hat{H} = \hat{T} + \frac{\alpha^2}{r^3}\hat{\boldsymbol{L}} \cdot \hat{\boldsymbol{S}} + V_{\text{core}}(r), \tag{2.1.5}$$

where $\hat{T}$ is the kinetic energy operator, α is the fine-structure constant, r is the distance between the core and the Rydberg electron, $\hat{\boldsymbol{L}}$ is the orbital angular momentum operator and $\hat{\boldsymbol{S}}$ is the spin operator. In this thesis the term hydrogenic will be applied to results stemming from this Hamiltonian, with the replacement $V_{\text{core}} \to -1/|r|$.

The solutions to the angular part of the Schrödinger equation are well-known, since the potential is still a central potential. The radial wavefunction, though, has to be found numerically, except in the hydrogenic case, and an example of the Rydberg electron radial wavefunctions (grey) R for Rydberg states $30l_{l+1/2}$ with $l = 0$ and $l = 29$, that is minimal and maximal angular momentum for $n = 30$, is shown in Figure 2.2, along with solutions to the hydrogenic Hamiltonian (black). For large angular momentum, the Rydberg electron does not penetrate the core, and the radial wavefunction is practically independent of the type of potential. For zero angular momentum, however, the Rydberg electron penetrates all the way to the core and we see a clear difference between the radial wavefunctions resulting from the two types of potential. In both the minimal and maximal angular momentum case, we see that the Rydberg electron has a very large orbital radius, on the order of 1000 Bohr radii, this is the crux of Rydberg physics.

2.1.1 Scaling relations

The Rydberg formula eq. (2.1.1) tells us that the energy of a Rydberg atom E_{nlj} increases roughly inverse square n^{-2} in principal quantum number n, and the energy spacing ΔE between two neighbouring principal quantum numbers is

$$\Delta E = \text{Ry}\left(\frac{1}{(n+1)^2} - \frac{1}{n^2}\right) = \text{Ry}\frac{n^2 - \left(n^2 + 2n + 1\right)}{n^4 + 2n^3 + n^2} \approx -2\frac{\text{Ry}}{n^3}, \tag{2.1.6}$$

for large n.

Rydberg atoms are also known for their very long (radiative) lifetimes τ_{nl}, which depends inversely on the overlap between the wavefunctions of the Rydberg and ground state. This overlap quickly decreases as the electron orbit is pushed further out, and therefore the radiative lifetime increases with n. The radiative lifetime τ_{nl}^{rad} can, according to [Gal94, Bet09, Saf10a] be roughly estimated, at zero temperature, by

$$\tau_{nl}^{\text{rad}} = \tau_l^{\text{rad}} n^3, \tag{2.1.7}$$

where τ_l^{rad} is the zero temperature l-dependent radiative lifetime. However, the interaction with black body radiation, that is the heat radiation of thermal bodies, becomes significant for states with high n and the total lifetime of a Rydberg atom is

$$\tau_{nl} = \left(\frac{1}{\tau_{nl}^{\text{rad}}} + \frac{1}{\tau_{nl}^{\text{BB}}}\right)^{-1}, \tag{2.1.8}$$

where τ_{nl}^{BB} is the lifetime due to decay stimulated by black body radiation. An extensive work, covering lifetimes for n up to 80 and l up to 2 at temperatures of 0K, 77K 300K and 600K for the stable alkalis, can be found in [Bet09].

In addition, we know by virtue of the virial theorem that the potential energy of the Rydberg electron is twice the kinetic energy with opposite sign

$$\left\langle nlj \middle| \hat{V} \middle| nlj \right\rangle = -2 \left\langle nlj \middle| \hat{T} \middle| nlj \right\rangle, \tag{2.1.9}$$

yielding an estimate for the expectation value of the potential energy

$$\left\langle nlj \middle| \hat{V} \middle| nlj \right\rangle = 2E_{nlj} \approx 2\frac{\text{Ry}}{n^2}. \tag{2.1.10}$$

From this we can make a classical estimate of the electron orbital radius r_{Orbit} as

$$-\frac{1}{r_{\text{Orbit}}} = \left\langle nlj \middle| \hat{V} \middle| nlj \right\rangle \approx 2\frac{\text{Ry}}{n^2} \qquad \Rightarrow \qquad r_{\text{Orbit}} \approx \frac{n^2}{2\text{Ry}}, \tag{2.1.11}$$

increasing very quickly with principal quantum number n. This means that for Rydberg atoms the classical orbital radius of the electron is more than 900 times larger than that of a ground state atom, agreeing very well with the observations in Figure 2.2. For comparison, this is roughly the size of vira. However, often we consider Rydberg atoms with $n \approx 100$, see Chapter 5, resulting in atoms the size of typical prokaryote cells. Displacing the Rydberg electron this much from the nucleus does not go unnoticed, though, but leads to a variety of effects all scaling with n. For actual calculations of Rydberg atoms, the species and state specific quantum defect are taken into account, but the general picture remains the same.

Many of the 'exaggerated' properties of Rydberg atoms stem from the large orbital radius of the Rydberg electron. A classical system with two charges at small but appreciable distances from one another will result in a dipole. Though we do not necessarily get a permanent dipole moment in an atom, which of course is a quantum system, at least the polarisability of the atom and the induced dipole moments must scale very strongly with n.

Due to the large orbital radius of the Rydberg electron, a Rydberg atom would classically (that is with the Rydberg electron being a localized particle) behave like a dipole. However, undisturbed Rydberg states are spherically symmetric and there is no preferred direction. Introducing a perturbator, which breaks the symmetry of the system, leads to strong responses, as the Rydberg atom gains a dipole moment. As an example, consider a weak electric field $\boldsymbol{F} = F\hat{z}$ oriented along the z-axis. The perturbation on the Rydberg atom by this electric field is described by the Hamiltonian

$$H' = -F\hat{z} \cdot \boldsymbol{r}. \tag{2.1.12}$$

Assuming hydrogenic Rydberg wavefunctions, we can use perturbation theory to find the response of the Rydberg atom to the electric field. The first order energy shift is zero, as hydrogenic wavefunctions are (a)symmetric along the z-axis resulting in an overall asymmetric integral. The first order change to a hydrogenic state $|nljm_j\rangle$ is then, assuming the states to be properly orthogonalized to lift the

23

degeneracy,

$$\widetilde{|nljm_j\rangle} = F \sum_{\text{other states}} \frac{\langle n'l'j'm'_j|\hat{z}\cdot\boldsymbol{d}|nljm_j\rangle}{E - E'}|n'l'j'm'_j\rangle, \qquad (2.1.13)$$

where $\boldsymbol{d} = -e\boldsymbol{r}$ is the dipole operator, E (E') is the energy of the state $|nljm_j\rangle$ ($|n'l'j'm'_j\rangle$) and the sum runs over all other (orthogonalized) hydrogenic states. From this we can make two observations: the perturbed state has an induced dipole moment and the second order energy shift is

$$E^{(2)} = F^2 \sum_{\text{other states}} \frac{|\langle n'l'j'm'_j|d_z|nljm_j\rangle|^2}{E - E'} \equiv \frac{1}{2}\alpha_0 F^2, \qquad (2.1.14)$$

where α_0 is the polarisability of the atom. This leads to a very strong scaling with n as the dipole matrix elements, when non-zero, scale as the orbital radius of the Rydberg electron $\langle r \rangle \propto n^2$ and the energy spacing as n^{-3}, yielding

$$\alpha_0 \propto n^7. \qquad (2.1.15)$$

One of the most fascinating and useful properties of Rydberg atoms is the very strong interaction between them. Since Rydberg atoms are electrically neutral, the primary interaction channel is the dipole-dipole interaction between the to atoms. Assuming the atoms are separated beyond the dissociation limit (usually taken to mean beyond the LeRoy radius), such that the interaction can be modelled classically [LeR70, LeR74], we can model the interaction as a dipole-dipole interaction

$$V_{dd} = \frac{\boldsymbol{d}_1\cdot\boldsymbol{d}_2}{R^3} - 3\frac{(\boldsymbol{d}_1\cdot\boldsymbol{R})(\boldsymbol{d}_2\cdot\boldsymbol{R})}{R^5}, \qquad (2.1.16)$$

where $\boldsymbol{d}_1$ $(\boldsymbol{d}_2)$ is the dipole (position) operator for the valence electron in atom 1 (2) and R is the distance between the (centres mass of the) two atoms.

Again, we will use perturbation theory to examine the interaction of the nearby Rydberg atoms. Consider a system of two Rydberg atoms, where both atoms are excited to the same Rydberg state, the combined two-atom state is then $|nljm_j\rangle \otimes |nljm_j\rangle$, and the interatomic axis and the quantization axis are both the z-axis. The matrix elements of the dipole-dipole operator are given by

$$M_{dd} = \langle n''l''j''m''_j|z_2|nljm_j\rangle\langle n'l'j'm'_j|z_1|nljm_j\rangle, \qquad (2.1.17)$$

The diagonal elements are always zero, as the Rydberg states have no permanent dipole element, but the interaction with other states might be finite. Assuming the Rydberg state to be an nS state, the only allowed dipole transitions are to the $n'P$ states. For simplicity we reduce the system to a toy model, where the Rydberg atoms are interacting via a single other two-atom state $|n'P\rangle \otimes |n''P\rangle$. Writing out the perturbation Hamiltonian in matrix form

$$H' = \begin{pmatrix} 0 & (1-3)\frac{\widetilde{M_{dd}}}{R^3} \\ (1-3)\frac{\widetilde{M^*_{dd}}}{R^3} & \Delta E, \end{pmatrix} \qquad (2.1.18)$$

where $\widetilde{M}_{dd}$ is the matrix element eq. (2.1.17) between the two-atom Rydberg state and the two-atom state $|n'P\rangle \otimes |n''P\rangle$, and ΔE is the energy difference between the two two-atom states. From this we find the energy

$$E^{(2)} = \frac{\Delta E}{2} \pm \sqrt{\left(\frac{\Delta E}{2}\right)^2 + \frac{|\widetilde{M}_{dd}|^2}{R^6}} \qquad (2.1.19)$$

$$= \begin{cases} -\frac{|\widetilde{M}_{dd}|^2}{\Delta E R^6} \\ \Delta E + \frac{|\widetilde{M}_{dd}|^2}{\Delta E R^6} \end{cases} \qquad \Delta E >> |\widetilde{M}_{dd}|^2/R^6, \qquad (2.1.20)$$

which results in a $\pm |\widetilde{M}_{dd}|^2/(\Delta E R^6)$ interaction, which is known as the Van der Waals interaction, for $\Delta E >> |\widetilde{M}_{dd}|^2/R^6$. The strength of this interaction can be further quantified by use of eq. (2.1.14), since both Rydberg atoms are in the same state, the interaction strength C_6 is proportional to

$$C_6 \equiv \frac{|\widetilde{M}_{dd}|^2}{\Delta E} = 4\frac{(E - E')(E - E'')}{\Delta E}\alpha_0^2 \propto \frac{n^{-3}n^{-3}}{n^{-3}}n^7 n^7 = n^{11}. \qquad (2.1.21)$$

This is a remarkably strong scaling with principal quantum number n and, despite the simplicity of this toy model, consistent with experimental observation [Sin04, Saf10a].

In reality, the interaction between Rydberg atoms is somewhat more complicated, and the interaction can be both attractive and repulsive [Sin05]. At shorter distances the interaction is dominated by resonant dipole-dipole interactions [Saf10a] and is sensitive to Zeeman degeneracy and hence the magnetic quantum number m_j [Wal08]. These long-range interactions can lead to macro molecules [Boi02, Boo15] and find applications in quantum information [Saf10a].

2.1.2 Excitation - blockade and facilitation

Rydberg atoms can be excited from ground state alkali atoms either directly [Han14] in a single-photon process or via an intermediate state [Bra03, chap. 4] in what is known as a two-photon excitation, see Figure 2.3. In both cases we use the (electric) dipole approximation [Bra03, chap. 4.3] to find the interaction between the photon and the valence electron of the atom. This approximation is valid, when the wavelength of the light is much longer than the size of the atom. Typical wavelengths of the lasers involved are in the visible spectrum, 400-800nm, much larger than a ground state atom, which has orbital radius 50pm.

Using this approximation, we can calculate the transition matrix elements of an atom subject to a monochromatic classical laser field with vector potential $\boldsymbol{A}$ in the Coulomb gauge, following the approach of [Bra03], for weak laser fields we get the perturbation Hamiltonian

$$H' = \boldsymbol{A} \cdot \boldsymbol{p} = \frac{A_0}{2} \left(\exp\left[i(\boldsymbol{k} \cdot \boldsymbol{r} - \omega t)\right] + \exp\left[-i(\boldsymbol{k} \cdot \boldsymbol{r} - \omega t)\right]\right)\hat{\varepsilon} \cdot \boldsymbol{p}, \qquad (2.1.22)$$

where $\boldsymbol{p}$ is the momentum operator, A_0 is the amplitude of the vector potential, $\boldsymbol{k}$ is the photon wave number, ω is the photon frequency t is the time and $\hat{\varepsilon}$ the polarization vector.
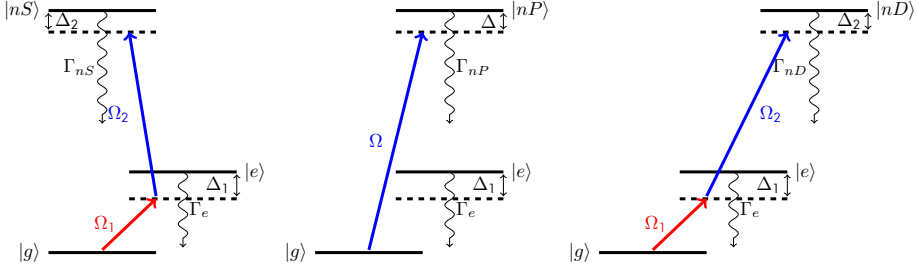
Figure 2.3: *Excitation schemes with one or two photons. Left, two-photon excitation to an nS Rydberg state. Middle, single photon excitation to an nP Rydberg state. Right, two-photon excitation to an nD Rydberg state.*

To apply the dipole approximation, we ignore the dependence of the electric field of the laser on position $\boldsymbol{r}$

$$\exp\left[i(\boldsymbol{k}\cdot\boldsymbol{r} - \omega t)\right]\hat{\boldsymbol{\varepsilon}}\cdot\boldsymbol{p} \approx \exp(-i\omega t)\hat{\boldsymbol{\varepsilon}}\cdot\boldsymbol{p}. \tag{2.1.23}$$

We now use that $\boldsymbol{p} = d\boldsymbol{r}/dt$ and remember that

$$i\hbar\frac{d\boldsymbol{r}}{dt} = [\boldsymbol{r}, H_0] \Rightarrow \left\langle a\left|\frac{d\boldsymbol{r}}{dt}\right|b\right\rangle = -i\left\langle a|\boldsymbol{r}H_0 - H_0\boldsymbol{r}|b\right\rangle = i(E_b - E_a)\left\langle a|\boldsymbol{r}|b\right\rangle, \tag{2.1.24}$$

where $|a\rangle$ and $|b\rangle$ are some appropriate states with associated energies E_a and E_b respectively, since H_0 is by far the dominant term in the Hamiltonian.

We have now reduced the matrix elements of the perturbation Hamiltonian eq. (2.1.22) to

$$\langle a|H'|b\rangle = iA_0\left(E_b - E_a\right)\cos\left(\omega t\right)\hat{\boldsymbol{\varepsilon}}\cdot\langle a|\boldsymbol{r}|b\rangle, \tag{2.1.25}$$

which is only dependent on the matrix element $\langle a|\boldsymbol{r}|b\rangle = \boldsymbol{r}_{ab}$. This is the dipole matrix element in atomic units, which we will call $\boldsymbol{D}_{ab} = -e\boldsymbol{r}_{ab}$, since the elemental charge e is not one in other unit systems. This is a commonly used approximation, and the dipole matrix elements give rise to the well-known selection rules of dipole transitions. Details on evaluating the dipole matrix elements are commonplace, see *e.g.* [Bra03]. For alkali atoms the ground state is always an S-state, i.e. a zero orbital angular momentum state ($l = 0$). In dipole transitions, each photon changes the orbital angular momentum l of the atom by ± 1, hence the single photon excitation can only reach nP-states ($l = 1$), whereas two-photon excitations can reach both nS-states ($l = 0$) and nD-states ($l = 2$). We focus on the two-photon transitions, as the nP Rydberg levels are shorter lived and we prefer the spherical symmetry of the nS levels.

Figure 2.3 illustrates the three different paths to Rydberg excitations via dipole transitions. We see how the different excitation schemes can reach the three different l-states. Since many states are unreachable via any specific dipole transition, we truncate the state space to only include the states that can be
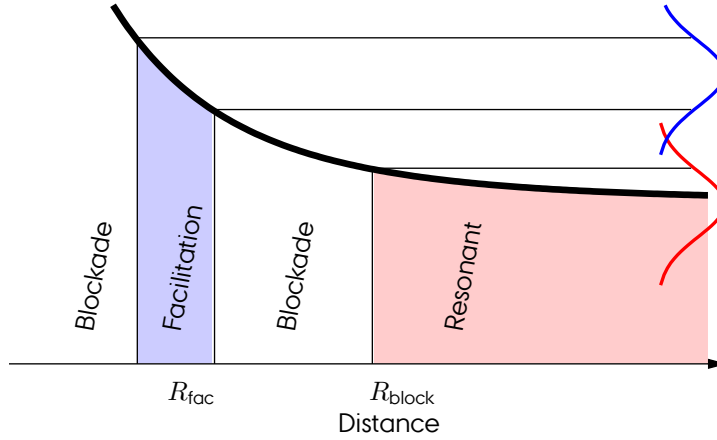
Figure 2.4: *Schematic of the Rydberg excitation regimes using either resonant excitation (red curve) or slightly blue detuned excitation (blue curve). Far from existing Rydberg atoms, a new Rydberg atom can be resonantly excited (red area). The dipole-dipole interaction with a nearby Rydberg atom shifts the energy level (thick black) out of resonance and a new Rydberg atom can not be excited resonantly if too close to an existing atom (white area), the crossover between the resonant and blocked excitation happens at the so-called blockade radius. With a blue detuned excitation laser, new Rydberg atoms will be resonantly excited in a thin region (blue) at a distance known as the facilitation radius R_{fac} from an existing Rydberg atom in a process known as facilitation.*

reached, and write the Hamiltonian in matrix form

$$H = \begin{pmatrix} 0 & \Omega_1 & 0 \\ \Omega_1^* & -\Delta_1 & \Omega_2 \\ 0 & \Omega_2^* & -\Delta_2 \end{pmatrix} \qquad \text{or} \qquad H = \begin{pmatrix} 0 & \Omega \\ \Omega^* & -\Delta \end{pmatrix}, \qquad (2.1.26)$$

for two and single photon transitions respectively. The Rabi frequencies $\Omega_{(i)}$ are determined from eq. (2.1.22), taking advantage of the dipole approximation and the detunings are the energy in the atom-photon system as a whole. The spontaneous decay rate from the intermediate level Γ_e (for two-photon approaches) is very large, therefore we usually keep the detuning from this state Δ_1 large, which ensures an insignificant population transfer to the intermediate state and we can, in general, ignore the decoherence induced by the decay from this state. However, in Chapter 5 we will use another approach to take this decoherence into account. The large detuning also allows us to ignore the intermediate state completely by adiabatic elimination.

The detuning of the Rydberg state, however, leads to vastly different physics for the Rydberg atoms, see Figures 2.4 and 2.5. Here we, for the sake of argument, consider rubidium atoms being excited to nS Rydberg states. The two atoms are so far apart that we can safely assume that the electron clouds do not overlap and that we can treat their effective interaction classically. The dipole-dipole

interaction between these states results in an increase in energy, which we here will assume is of the Van der Waals type, giving the total energy

$$E(R) = E_0 + \frac{C_6}{R^6},$$ (2.1.27)

where E_0 is the energy of the Rydberg state, C_6 is a positive constant, see eq. (2.1.21), and R is the distance to an existing Rydberg atom. With zero Rydberg detuning $\Delta_2 = 0$, the excitation of a new Rydberg atom far away from all existing Rydberg atoms (if any) is resonant, which means that exciting this new Rydberg atom is as likely as exciting the first Rydberg atom. However, nearer to an existing Rydberg atom, the dipole-dipole interactions start to shift the energy levels of our potential Rydberg atom by C_6/R^6 (eq. (2.1.27)). When the energy shift becomes larger than the line width σ_{nS} of the Rydberg state $|nS\rangle$, excitation of new Rydberg atoms becomes severely suppressed. This leads to a volume of space surrounding existing Rydberg atoms, where new Rydberg atoms are unlikely to to be excited. We call this volume the blockaded region, and we define the so-called blockade radius R_{block}, within which Rydberg excitation is suppressed

$$\sigma = \frac{C_6}{R_{\text{block}}^6} \qquad \Leftarrow \qquad R_{\text{block}} = \sqrt[6]{\frac{C_6}{\sigma_{nS}}}.$$ (2.1.28)

In Figure 2.4 the region of resonant excitation is indicated by red and the blockaded region by white. If the excitation laser is slightly negative detuning, what is known as red detuning, this picture still holds, but the excitation probability drops off with increasing magnitude of the detuning. The blockade radius approaches infinity, but it will still be much more likely to find well separated Rydberg atoms rather than close neighbours.

An additional possibility is represented in Figure 2.4, namely that the excitation laser is positively detuned from the Rydberg transition, what is known as blue detuning. If the detuning is larger than the line width of the Rydberg state, it is unlikely to excite a Rydberg atom, however, if one already exists, either by chance or seeding, we can define a distance in analogy to the blockade radius R_{block} in eq. (2.1.28)

$$R_{\text{fac}} = \sqrt[6]{\frac{C_6}{\Delta_2}},$$ (2.1.29)

which we call the facilitation radius, because existing Rydberg atoms facilitate the excitation of new Rydberg atoms at this distance. In reality, facilitation happens in a thin shell around R_{fac}, blue in Figure 2.4, due to the finite line width of the Rydberg state. Both inside and outside this shell Rydberg excitation is blocked.

The difference between these two situations, red detuned blockade ($\Delta_2 = 0$ MHz) and blue detuned facilitation ($\Delta_2 = 1$ MHz), is shown in Figure 2.5, which has been created using the same methods as in Chapter 5. In this figure, the blue dots represent ground state rubidium atoms in a cold atomic gas in a thin sheet measuring $125\,\mu$m $\times$ $125\,\mu$m $\times$ $1\,\mu$m. The atoms are assumed to be motionless on the timescales of the simulation. The red dots indicate atoms that have been excited to the $99S_{1/2}$ Rydberg state.
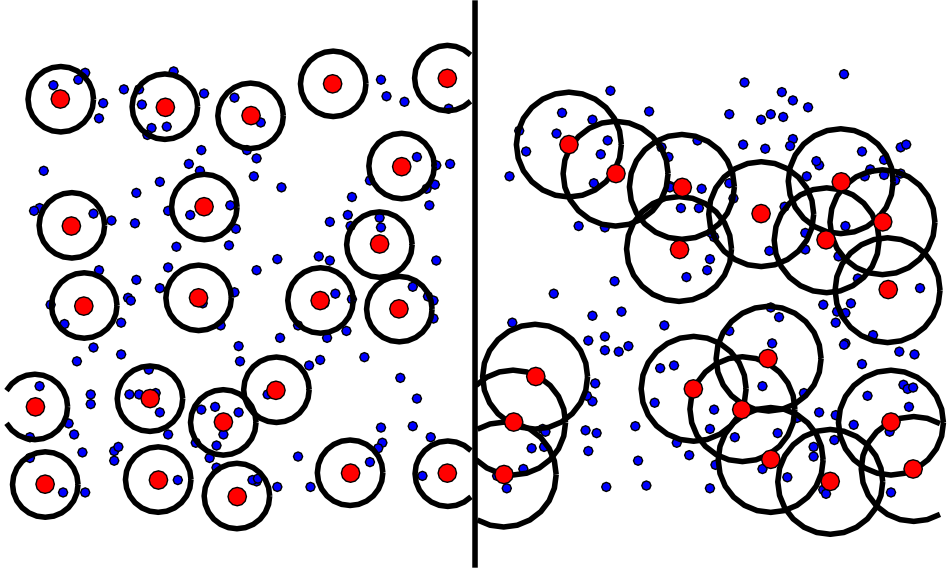
Figure 2.5: *Rydberg atoms (red) excited from an ultra-cold background gas (blue) using the methods of Chapter 5. Left hand side shows the Rydberg atoms in the blockade regime are randomly distributed, but never within the blockade radius of one another (black circles are at half a blockade radius). Right hand side shows the Rydberg atoms in the facilitation regime are distributed in clusters with distances within a cluster being the facilitation radius (black). This figure has been made using the simulations reported in chapter 5, with a $150\mu m$ square of laser light exciting to the intermediate state intersecting a $1\mu m$ thin sheet of laser light exciting the Rydberg state.*

The left hand side of Figure 2.5, shows the distribution of Rydberg atoms under red detuning. The black circles are drawn at a distance of $R_{\text{block}}/2$ from the Rydberg atoms. None of the black circles overlap, indicating that Rydberg atoms are located at least R_{block} apart, and evenly distributed in the atomic cloud.

On the right hand side of Figure 2.5, the same simulation has been done, but with blue detuning. The black circles here are drawn R_{fac} from the Rydberg atoms. In this case the Rydberg atoms come in clusters each originating from a single off-resonant excitation, known as a seed, the seed then facilitates the resonant excitation of new Rydberg atoms in the facilitation shell around it. The new Rydberg atom also has a facilitation shell, where resonant excitation occurs, growing the cluster of evenly spaced Rydberg atoms. However, the combined effect of two or more Rydberg atoms moves the facilitation shell just a bit further away, making the Rydberg spacing slightly uneven.

In both the red and blue detuning cases, we can imagine that the space fills up with Rydberg atoms and the blockaded region around them. In this case all the atoms in the cloud are either Rydberg atoms or blocked from excitation by a Rydberg atom. This is known as the jamming limit, and leads to a clear signature when analysing the number of Rydberg atoms in the cloud statistically,

simply because the number of ways to distribute Rydberg atoms in a way that fills up the volume is limited. If there was no blockade region (and the number of atoms in the cloud is very large) we expect the number of Rydberg atoms to be completely random, and excitation events are independent of both each other and time. This results in a Poisson distribution of the number of Rydberg atoms, when considering many realizations of the experiment or simulation. However, when taking the blockade effect into account, we reach the jamming limit and we need (more or less) the same number of Rydberg atoms to reach the jamming limit, resulting in very small variance on the number of Rydberg atoms. We call this distribution subpoissonian.

2.2   Stochastic variation

Stochastic variation is a technique suitable for optimizing a finite basis set with a large parameter space to span the eigenstates, with extreme eigenvalues, of an operator, by making random changes to the basis. Usually, but not necessarily, the operator in question is the Hamiltonian, and optimization is for lowest energy.

The Mini-Max theorem [Suz98] tells us that, by random optimization, our initial basis will converge on a basis spanning the eigenfunctions of the operator, whose eigenvalues we are optimizing against. Provided that care is taken in the implementation of the optimization, we can hope to span many eigenfunctions of the operator.

Stochastic variation is not suitable for operators that are easily diagonalized or when the parameter space of the basis functions is easily searched, usually because it has low dimensionality. However, parameter space is often riddled with local minima making deterministic minimization techniques practically useless for determining the optimal configuration in parameter space. The power of stochastic variation is this ability to find global minima in parameter spaces of high dimensionality and large numbers of local minima. This makes stochastic variation very suitable for systems with high degree of correlation. Such systems often require explicitly correlated basis functions, resulting in extremely complicated parameter space landscapes, full of local minima [Suz98].

Imagine a set of k functions $S_k = \{f_1, \ldots, f_k\}$ each with a set of parameters α_i $(i = 1, \ldots, k)$, which are randomly chosen from a infinitely large set set $S_\infty \supset S_1$ of linearly independent functions forming a complete basis for L^2. The set of chosen functions will form the basis of a k-dimensional subspace $V_k \subset L^2$, which we restrict our operator $\hat{Q}$ to, denoted $\hat{Q}_{V_k}$. By virtue of the Mini-Max theorem, the eigenvalues of the restricted operator are then upper bounds for the eigenvalues of the unrestricted operator. By taking another random selection $S_2 \subset S_\infty$, which will also form the basis of a k-dimensional subspace $W_k \subset L^2$ ($W_k \neq V_k$), we can compare the eigenvalues of the operator when restricted to each subspace. The idea is then to pick the subspace providing the more desirable set of eigenvalues, we will shortly approach on what this means, and do the same thing over and over again, until the eigenvalues no longer improve. The eigenfunctions of the operator restricted to the subspace providing the most optimal set of eigenvalues are then taken to represent the eigenfunctions of the unrestricted operator corresponding to the k eigenvalues we optimized against. In reality, though, the actual number
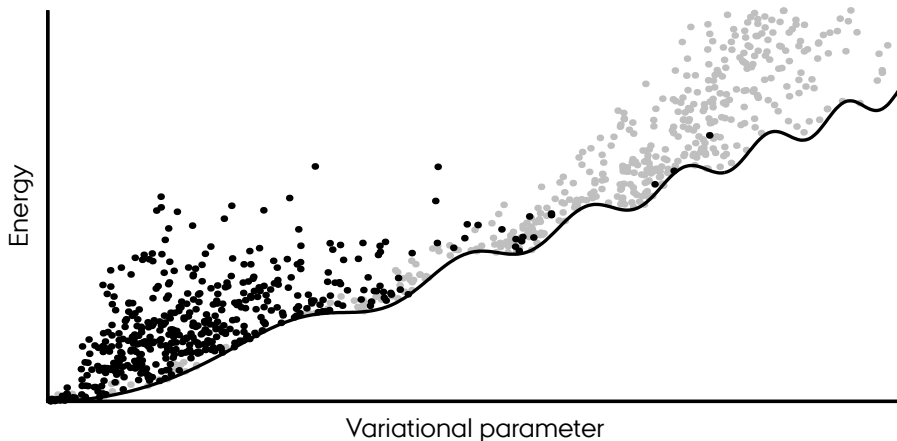
Figure 2.6:   *Energy landscape as function of some variational parameter. By stochastically picking starting points (grey) and performing random changes to the variational parameter, we can get estimates for the lowest energy of the system, without getting into trouble with local minima.*

of suitable eigenfunctions and -values is lower than k.

However, we are still left with the somewhat ill-defined notion of a more desirable set of eigenvalues. Since the operator in question for the implementation used in chapter 6 is the Hamiltonian, the eigenvalues are canonically referred to as the energies, and we are always concerned with finding the lowest energy states, the most desirable set of eigenvalues is the one containing the lowest value. This approach of simply optimizing by always choosing the lowest single value, is often good enough to ensure good representations of the first few excited states too, see Figure 2.6.

The method described above basically works by probing a large number of points in the parameter space, and choosing the one providing the answer one might deem best. However, assuming we are fairly close to a basis that already spans the eigenfunction with the lowest energy, it might be more effective to only make small variations to the basis set. Rather than picking a completely new basis set, we will sequentially replace each basis function one at a time. If a given replacement does not lower the lowest energy of the restricted Hamiltonian, we reject the replacement and try replacing the next function in the basis set. If, on the other hand, the replacement does lower the lowest energy, we admit the replacement to the basis and start over from the first function, since any of the earlier optimized functions might be optimized better, when taking this latest replacement into account. When we reach the end of the sequence without making any replacements, we can assume that we have reached the lowest possible energy. This algorithm can be captured in the following steps

1. Randomly pick a set of ordered basis functions $\{f_1, \ldots, f_k\}$ from a family of

linearly independent functions F forming a complete basis for L^2, set $i = 1$.

2. Calculate (a representation of) the restricted Hamiltonian and determine the (lowest) energy E_{low}

3. Replace f_i with a randomly chosen trial function $g \in F$ and determine the new restricted Hamiltonian and its lowest energy E_{test}

   If: $E_{\text{low}} > E_{\text{test}}$, make the substitutions $g \to f_i$ and $E_{\text{test}} \to E_{\text{low}}$, set i to 1 and go to 3.

   If: $E_{\text{low}} \leq E_{\text{test}}$ and $i < k$, set i to $i + 1$ and go to 3.

4. We are done

While this method works in theory, reliability can be improved drastically in two ways. One, instead of just using a single trial function to find a replacement to a basis function, we can randomly pick a set of trial functions, try out all these as a replacement in our basis, and then pick the best one as the replacement. Of course only if any of the trial functions are better than the one already in the basis. Two, we can require that the sequence can be completed several times without making any new admissions to the basis, before we assume to have reached the optimal basis. In principle we could calculate the parameter space gradient at this point and do a deterministic optimization, but it is often of limited use and involves extended computation. Instead, it proves more useful to repeat the algorithm from a different start basis and see if this can provide a better estimate for the lowest energy. This ties in to an important fact to keep in mind, when designing a stochastic variational algorithm: Determination of the restricted operator eigenvalues has to be fast and accurate. If we can not determine these eigenvalues fast enough, to out-compete other algorithms, why then bother with a variational approach? If we can not do it accurately enough, we could build up errors and possibly end up with impossibly low energies, i.e. energies below the ground state energy of the system, as we optimize for error rather than energy.

So far we have not considered this implementation, but rather kept the treatment abstract. We will now delve into the specific details of the implementation used in writing chapter 6. We will start out by choosing a family of functions to build our basis from. As discussed above, there are three properties we need this family of functions to have:

1. Linear independence

2. Form a complete basis of L^2

3. Fast and accurate determination of (a representation of) the restricted Hamiltonian

We intend to use this algorithm to explore two-electron systems and therefore prefer a set of basis functions, which includes correlations inherently, i.e. the chosen set of multi-body basis functions is not simply the direct product of several sets of single-body basis functions, taking advantage of the strengths of stochastic variation. When considering the three points above in connection with the aim for inherently correlated basis functions, we have settled on so-called explicitly
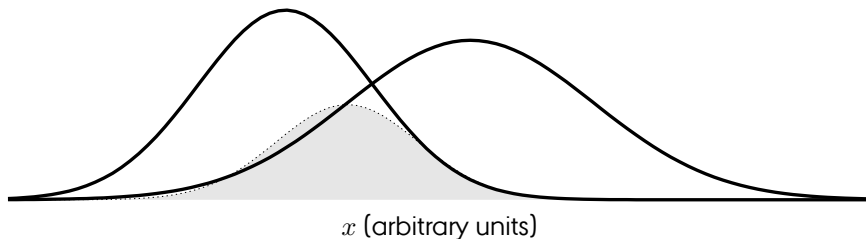
x (arbitrary units)

Figure 2.7: *Two Gaussian functions (black solid) and their product (grey). Products of Gaussian functions are themselves Gaussian functions.*

correlated Gaussians as the function family we pick our basis sets from [CGm]. These are functions of the form

$$\psi(\boldsymbol{x}) = \exp\left[-\frac{1}{2}(\boldsymbol{x} - \boldsymbol{a})^T A (\boldsymbol{x} - \boldsymbol{a})\right], \tag{2.2.1}$$

where $\boldsymbol{x}$ is the position vector of the electrons, A is a symmetric, real valued, positive definite matrix generating both the correlations between the electrons and the overall shape of the multi-dimensional Gaussian in position space, $\boldsymbol{a}$ is a vector responsible for shifting the peak of the Gaussian in position space.

Though (correlated) Gaussians are non-orthogonal, this need not be a problem. Start by considering an arbitrary function f_c in the subspace V_k spanned by the set $S_k = \{\psi_1, \ldots, \psi_k\}$ of k correlated Gaussians, we can write f_c in terms of the basis functions

$$f_c = \sum_{i=1}^{k} c_i \psi_i, \tag{2.2.2}$$

we can then define the vector $\boldsymbol{c} = (c_1, \ldots, c_k)^T$, containing the expansion coefficients of f_c. We shall say this vector characterizes f_c. Let us further define the overlap matrix $N \in \mathbb{R}^{k \times k}$, whose elements are

$$N_{ij} = \int_{-\infty}^{\infty} \psi_j(x) \cdot \psi_i(x)\, dx, \tag{2.2.3}$$

and the Hamiltonian matrix H, with elements

$$H_{ij} = \int_{-\infty}^{\infty} \psi_j(x)\hat{H} \cdot \psi_i(x)\, dx. \tag{2.2.4}$$

We remark that both N and H are real valued and symmetric and N is positive definite. Since the basis functions are non-orthogonal, we know that the overlap between two functions f_v and f_u, characterized by vectors $\boldsymbol{v}$ and $\boldsymbol{u}$ correspondingly, is given by

$$\sum_{i=1}^{k}\sum_{j=1}^{k} \int_{-\infty}^{\infty} v_j \psi_j(x) \cdot u_i \psi_i(x)\, dx = \boldsymbol{v}^T N \boldsymbol{u}. \tag{2.2.5}$$

33

Assuming f_u to be an eigenfunction of $\hat{H}$ with eigenvalue E, we get

$$\sum_{j=1}^{k} \int_{-\infty}^{\infty} v_j \psi_j(x) \cdot f_u \, dx = E \sum_{j=1}^{k} \int_{-\infty}^{\infty} v_j \psi_j(x) \cdot f_u \, dx$$

$$= E \sum_{i=1}^{k} \sum_{j=1}^{k} \int_{-\infty}^{\infty} v_j \psi_j(x) \cdot u_i \psi_i(x) = E \boldsymbol{v}^T N \boldsymbol{u}, \qquad (2.2.6)$$

i.e. if f_u is an eigenfunction of $\hat{H}$ then $\boldsymbol{u}$ is the solution to the generalized eigenvalue problem

$$H\boldsymbol{u} = EN\boldsymbol{u}. \qquad (2.2.7)$$

This sort of problem can readily be solved by MATLAB's `eig()` function, by (for real symmetric matrices such as H and N) exploiting the Cholesky decomposition

$$N = LL^T, \qquad N \text{ positive definite}, \qquad (2.2.8)$$

and defining

$$\tilde{H} = L^{-1} H L^{-T}, \quad \tilde{\boldsymbol{u}} = L^T \boldsymbol{u}. \qquad (2.2.9)$$

This leads to the ordinary eigenvalue problem

$$\tilde{H}\tilde{\boldsymbol{u}} = L^{-1} H L^{-T} L^T \boldsymbol{u} = L^{-1} H \boldsymbol{u} = EL^{-1} N \boldsymbol{u}$$

$$= EL^{-1} LL^T \boldsymbol{u} = EL^T \boldsymbol{u} = E\tilde{\boldsymbol{u}}. \qquad (2.2.10)$$

We will not go into detail with calculations of operator matrix elements in a correlated Gaussian basis, but only give a general idea of how do it. We start by noting that the product of two Gaussians is also a Gaussian (see Figure 2.7)

$$\exp\left[-\frac{1}{2}(\boldsymbol{x} - \boldsymbol{a})^T A (\boldsymbol{x} - \boldsymbol{a})\right] \exp\left[-\frac{1}{2}(\boldsymbol{x} - \boldsymbol{b})^T B (\boldsymbol{x} - \boldsymbol{b})\right]$$

$$= \exp\left[-\frac{1}{2}\left(\boldsymbol{x}^T(A+B)\boldsymbol{x} + \boldsymbol{a}^T A \boldsymbol{a} + \boldsymbol{b}^T B \boldsymbol{b} - 2\boldsymbol{x}^T(A\boldsymbol{a} + B\boldsymbol{b})\right)\right]$$

$$= \exp\left[-\frac{1}{2}(\boldsymbol{x} - \boldsymbol{v})^T C (\boldsymbol{x} - \boldsymbol{v}) - \frac{1}{2}\left(\boldsymbol{a}^T A \boldsymbol{a} + \boldsymbol{b}^T B \boldsymbol{b} - \boldsymbol{v}^T C \boldsymbol{v}\right)\right], \qquad (2.2.11)$$

with $C = A + B$ and $\boldsymbol{v} = C^{-1}(A\boldsymbol{a} + B\boldsymbol{b})$. We can continue from here by making the substitution $\boldsymbol{y} = K(\boldsymbol{x} - \boldsymbol{v})$, since $C = K^T K$ is also symmetric, real valued and positive definite, and simply integrate coordinate-wise, since the Gaussian is uncorrelated in $\boldsymbol{y}$-coordinates.

Thus, the non-orthogonality of the correlated Gaussians does not represent a problem, and working with this type of basis function has a lot of benefits. As already explained, the correlated Gaussians inherently treat correlated states. More importantly though, the matrix representations of operators can be expressed analytically, which allows for fast and accurate evaluation of these matrices and hence their eigenvalues. For an extensive overview see [Suz98] or the online resource [CGm]. This leads to fast a repetition rate of the algorithm outlined above, and thus a good coverage of parameter space in a limited amount of time.

2.3 Monte Carlo simulation with shaped laser fields

Apart from the lasers and Rydberg atoms themselves, one of the most useful tools in the Rydberg physicists toolkit is the ability to shape the excitation lasers, as the requirements of trapping, detection and manipulation lasers become more complex in response to the increasing complexity of experiments [Bij13, Chap. 4]. The two-photon excitation (Figure 2.3) allows in its own right for some spatial control, as the blue Rydberg excitation laser can be shaped into a sheet, which has a Gaussian intensity profile in the z-direction with a width of typically 7 μm, while practically infinite in the remaining directions (x and y) [Wer17]. Such a thin sheet gives us a plane of Rydberg excitations, but more novel excitation patterns can be achieved by carefully moulding the red intermediate state excitation laser into a specific shape in the plane of the blue sheet [Bij13, Chap. 4].

In the work presented in this thesis, laser light has been imagined to be shaped by use of Spatial Light Modulators (SLM). As examples of a diffractive optical element, which spatially modulate the phase of the laser light without affecting the amplitude, SLMs can be dynamically shaped to provide an almost limitless laser pattern in the focal plane of a lens [Bij13, Chap. 4]. Other methods include interference between multiple laser beams [Gri03] and masking the laser into a specific shape, which is often used in laser lithography techniques [Wag10]. This might seem intuitive, but one has to keep in mind the loss of laser power due to only a part of the light interacting with the atomic cloud.

Diffractive optical elements are, somewhat simplified, slabs of material that a coherent laser beam can either pass through or reflect upon, but in the process of doing so, gains a phase pattern depending on the position on the element [Bij13, Chap. 4]. Such elements can be made using a transparent material of varying thickness that the laser must pass through, acquiring a phase shift depending on the thickness of the material. Another approach to obtaining this spatially dependent phase shift is the SLM, which has a surface that can be controlled to make phase shifts at request. SLMs can be made using a variety of techniques including physical deformation of mirrors [Hor90] and the use of liquid crystal materials [Col89].

Both SLMs and other diffractive optical elements employ a spatially dependent phase shift to obtain a spatial intensity pattern in the far field or alternatively focal plane of a lens. As an example, let us assume a transmitting SLM, located one focal length f away from a lens, is imprinting a phase pattern $\phi(x, y)$, with x and y spanning the plane of the SLM, on a laser beam with intensity profile $U(x, y, z)$, which has uniform phase across the plane of the SLM surface, $U(x, y, -f) = U_0(x, y)$ with U_0 being some 2D intensity profile. In principle we should consider both the finite size and resolution of the SLM as well as the resulting diffraction, but these will all be neglected here. Since the SLM is placed exactly one focal length from the lens, the intensity profile U_f in the (other) focal plane of the lens can be found using a Fourier transform

$$U_f(X, Y) = \mathcal{F}\left[U(x, y, -f)e^{\phi(x,y)}\right](X, Y). \qquad (2.3.1)$$

For a specific desired shape U_f, there is no canonical way of finding the required imprint phase pattern $\phi(x, y)$.

The resolution of the shaped light is high enough, that addressing of individual atoms is possible [Zup16] and is used in both optical tweezers [Gri03, Wul06], Rydberg physics, where control over excitation volume geometry [Bij15, Lee16, Sel18] and single site addressability is important [Bij15, Bru15b]. Arbitrary light patterns can be engineered [Bre00], even with multiple wavelengths of light [Bru15a] and aberrations can be controlled by feedback to the SLM [Bru15b].

In chapter 5, we investigate crystal formation of a cloud of rubidium atoms under the influence of such shaped laser fields. We capture the dynamics of the system using incoherent time evolution, since we have to consider processes, such as decay from the intermediate and Rydberg states, which do not conserve the coherence of the ensemble. We model the time evolution of the system, using the Master Equation in Lindblad form where the state $|n\rangle$ decays with decay rate $\Gamma_{n,m}$ to the state $|m\rangle$

$$\frac{\partial}{\partial t}\rho = i[\rho, \hat{H}] + \sum_{n,m} \Gamma_{n,m} \left(|n\rangle\langle m|\rho|m\rangle\langle n| - \frac{1}{2}\left\{ |n\rangle\langle n|, \rho \right\} \right), \qquad (2.3.2)$$

with the curly brackets being the anticommutator.

The Master Equation provides a powerful tool to explore the time evolution of quantum systems, but since the density matrix scales quadratically with the number of states in the system, the problem quickly becomes prohibitively large to solve. Remember that for a system of N two-level quantum particles, the number of states of the system is 2^N leading to a number of free parameters in the density matrix of $2^{2N-1} + 2^{N-1} - 1$, since the matrix is Hermitian and the trace is 1.

To remedy this, we will use a Monte Carlo approach, which, for a set of fixed laser parameters, see Figure 2.3, uses random sampling to obtain a numerical simulation of the time evolution of a large number of atoms being excited to a Rydberg state. We will implement and use this approach in Chapter 5, and the specific implementation has been described in detail in [Wee17].

Our large quantum system consists of a cloud of many ultra-cold atoms with transitions of the internal states of the atoms being described by Figure 2.3. Since we only drive transitions between three internal states of each atom, we assume that they can each be described by a three-level quantum system. Further, we assume that the effect of one atom on any other is fully described via the state dependent dipole-dipole interaction eq. (2.1.16) as a Van der Waals potential $V_{VdW} = C_6/R^6$. The probability of any given atom transitioning to or from the Rydberg state is dependent on its own state, the laser parameters and the state of the rest of the cloud, but independent of time. The transition event is thus a memoryless stochastic variable.

We now make the following iterative process

1. Randomly pick N random three dimensional coordinates $r_1, \ldots, r_N$ in the cloud volume, N being the number of atoms in the cloud.

2. Construct the N-dimensional initial state-vector σ (usually a zero vector indicating no Rydberg excitations).

3. Calculate the matrix V with elements $V_{ij} = C_6/(|r_i - r_j|^6)$ if $i \neq j$ and zero otherwise.

4. Calculate the vector $\boldsymbol{\delta} = \Delta_2 + V\boldsymbol{\sigma}$.

5. Determine, for each atom i in the cloud, an excitation rate $\gamma_\uparrow(\delta_i)$ and a de-excitation rate $\gamma_\downarrow(\delta_i)$, both functions of the laser parameters with the replacement $\Delta_2 \to \delta_i$, using the Master Equation of a single atom. And determine the probability of change for atom i as $\gamma_i(\sigma_i) = (1 - \sigma_i)\gamma_\uparrow(\delta_i) + \sigma_i\gamma_\downarrow(\delta_i)$.

6. Generate a random time step Δt from an exponential distribution with mean $\sum_{i=1}^{N} \gamma_i(\sigma_i)$ at which the next transition will occur.

7. Randomly select an atom k with the probability of picking atom i being $\gamma_i(\sigma_i)$.

8. Set $\sigma_k \to 1 - \sigma_k$ and $t \to t + \Delta t$ and go back to 4, unless we reach the end time t_{end}.

This algorithm will realize one instance of the time evolution of the system. Two examples of such realizations at a specific time step, but with different laser parameters can be seen in Figure 2.5. By redoing the algorithm a large number of times, each with a new random outcome, we get statistical information on the time evolution of a cloud of ultra-cold atoms under the influence of the lasers in Figure 2.3.

Trapping of Rydberg Atoms in Tight Magnetic Microtraps
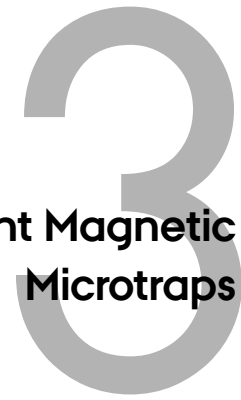
A. G. Boetes, R. V. Skannrup, J. Naber, S. J. J. M. F. Kokkelmans and R. J. C. Spreeuw

Abstract

We explore the possibility to trap Rydberg atoms in tightly confining magnetic microtraps. The trapping frequencies for Rydberg atoms are expected to be influenced strongly by magnetic field gradients. We show that there are regimes where Rydberg atoms can be trapped. Moreover, we show that so-called magic trapping conditions can be found for certain states of rubidium, where both Rydberg atoms and ground state atoms have the same trapping frequencies. Magic trapping is highly beneficial for implementing quantum gate operations that require long operation times.

3.1 Introduction

Atoms with one electron excited to a high principal quantum number n, commonly known as Rydberg atoms [Gal05], have been proposed as the basis for quantum simulators and quantum information processing [Saf10a, Mül11]. An idea going back to Richard Feynman [Fey82], a quantum simulator is an easily manipulated quantum system onto which the Hamiltonian of other quantum problems can be mapped. Ever since, quantum simulation and information processing has been driven by the promise of access to complex quantum systems as well as applications in quantum technology [fla17].

In this context, Rydberg atoms attract a lot of attention due to their extreme properties like n^{11} scaling of the C_6 Van der Waals coefficient and the blockade effect, providing strong interactions and the essential mechanism for quantum gates [Saf10a, Luk01a, Jak00a]. An important issue is to achieve so-called magic trapping, identical trapping potentials for the ground state and the Rydberg state. Magic trapping conditions can suppress decoherence due to atomic motion during quantum gate protocols, much needed for high-fidelity quantum operations [Wil10a, Saf16a]. However, this is challenging to realize for alkali atoms in optical traps [Zha11, Top14].

In this paper we show that magic trapping conditions can be achieved more easily in magnetic lattice traps [Wan16]. Both ground state and Rydberg atoms can be trapped in magnetic fields arising from microwires on a fabricated chip [Rei99, Fol00, Fol02, Rei02], or from a patterned magnetic film giving rise to an array of microtraps [Leu14, Whi09, Wan17]. These microtraps have very strong magnetic field gradients, hence are very tight, and can be arranged into different lattice geometries, such as square or hexagonal. Field gradients can be particularly strong using patterned magnets. Whereas gradients above microwires are typically 10-100 T/m, with magnetic film chips they can be readily two orders of magnitude higher. If the blockade radius is comparable to, or larger than, a single trap, each trap effectively becomes a single excitation site. In this paper we investigate the magnetic trappability of alkali Rydberg atoms, and address the issue of achieving magic trapping conditions.

For ground state atoms the magnetic field can be assumed to be uniform across the atom. However, the large classical electron orbit radii of the Rydberg atoms and the large gradients of the microtraps make this approximation invalid. Magnetic trapping of Rydberg atoms in other magnetic configurations has been studied by other authors [Cho05, Sin08, Les05a, Les05b, Sch07, Hez06, Hez07, May09b, May09a]. Our paper is related to the work performed by Mayle, Lesanovsky and Schmelcher (MLS) [May09b, May09a], however, our work is focused on the strong gradient regime of the microtraps, requiring a higher order expansion of the magnetic fields.

In this work we base our calculations on ^{87}Rb atoms, however, the treatment is generally applicable to other species as well. For a 50 kHz trap the oscillator length of a rubidium atom (34 nm) is much smaller than the rms radius of a $n = 50$ electron orbit (132 nm). The strong magnetic field gradient then results in a magnetic field difference of 0.9 G across the size of the atom, resulting in an energy difference of about 1.3 MHz, much larger than the trapping frequency. This paper therefore considers the effect of the spatial extent of the electronic wave

function on the trappability of the Rydberg atom in a magnetic trap.

In accordance with the Born-Oppenheimer approximation, we assume that the motion of the Rydberg electron and the atomic core can be separated, and that the light Rydberg electron will react instantly to any movement of the heavy core. We then use perturbation theory in the fine structure basis to find the energy of the Rydberg electron as function of the position of the core in the trap. These energies can be regarded as potentials for the core, which we call Potential Energy Surfaces (PES). We have expanded these potentials as harmonic traps around their respective minima and found feasible trapping conditions for a wide range of Rydberg states.

This paper is divided into six sections. In section 3.2 we provide a detailed description of the magnetic field configuration used in this work. In section 3.3 we provide the model Hamiltonian in Jacobi coordinates and discuss some of the differences to the earlier work by MLS. Furthermore, we discuss the perturbative treatment of the system. In sections 3.4 and 3.5 we discuss the outcome of the previous sections, with focus on trapping Rydberg atoms and magic trapping conditions. In section 3.6 we conclude on our work.

3.2   Parametrization of the magnetic traps

In the following two sections we use atomic ($\hbar = m_e = a_0 = 1$) units and summation over repeated indices for the sake of readability. We model the magnetic field as a Ioffe-Pritchard configuration around the trap minimum [Ger06]

$$\boldsymbol{B}(\boldsymbol{x}) = \begin{pmatrix} 0 \\ 0 \\ \mathcal{B} \end{pmatrix} + \mathcal{G} \begin{pmatrix} x_1 \\ -x_2 \\ 0 \end{pmatrix} + \frac{1}{2} \hat{\boldsymbol{e}}_i c_{ijk} x_j x_k. \qquad (3.2.1)$$

We shall call these terms constant $\boldsymbol{B}_c$, linear $\boldsymbol{B}_l$ and quadratic $\boldsymbol{B}_q$ respectively. The strength of the constant term is set to 3.23G. At this field the differential Zeeman shift between the two qubit states $|F = 1, m_F = -1\rangle$ and $|F = 2, m_F = 1\rangle$ vanishes [Dav02].

Expanding the magnetic fields to quadratic order goes beyond existing works in literature [May09b]. This is necessary for the systems with strong magnetic gradients we explore. This provides further accuracy for systems already investigated with linear only expansions, which can never explain axial trapping.

The linear term coefficient $\mathcal{G}$ provides confinement in the tight transverse directions. This coefficient has a value of 900 T/m for microtraps in a hexagonal lattice [Leu14]. In the remainder of this paper we use microtrap parameters as relevant for this hexagonal lattice. This is much greater than that of more conventional Z-wire magnetic chip traps with $\mathcal{G} \approx 7$ T/m [Nab16].

The curvature tensor c_{ijk}, which determines the strength of the quadratic term of the magnetic field, is symmetric under permutation of its indices and all partial traces vanish. This leaves 7 independent components. For the microtraps the non zero components of c_{ijk} are on the order of 10^7 T/m^2, again much larger than for a typical Z-wire trap, where the non zero components are on the order of 10-100 T/m^2.

Choosing the Coulomb gauge we find the vector potential corresponding to Eq. (3.2.1)

$$\boldsymbol{A}(\boldsymbol{x}) = \frac{\mathcal{B}}{2} \begin{pmatrix} -x_2 \\ x_1 \\ 0 \end{pmatrix} + \mathcal{G} \begin{pmatrix} 0 \\ 0 \\ x_1 x_2 \end{pmatrix} + \frac{1}{8} \hat{\boldsymbol{e}}_i \epsilon_{ijk} c_{jlm} x_l x_m x_k, \qquad (3.2.2)$$

with ϵ_{ijk} the fully antisymmetric Levi-Civita tensor. We retain the naming convention from the magnetic field, i.e. the curl of the 'linear' term of the vector potential corresponds to the linear term of the magnetic field $\nabla \times \boldsymbol{A}_l = \boldsymbol{B}_l$ etc. It is convenient to define "residual terms" for the magnetic field and the vector potential respectively, as follows

$$\tilde{\boldsymbol{B}}(\boldsymbol{R}, \boldsymbol{r}) = \boldsymbol{B}(\boldsymbol{R} + \boldsymbol{r}) - \boldsymbol{B}(\boldsymbol{R}) - \boldsymbol{B}(\boldsymbol{r}) \qquad (3.2.3)$$
$$\tilde{\boldsymbol{A}}(\boldsymbol{R}, \boldsymbol{r}) = \boldsymbol{A}(\boldsymbol{R} + \boldsymbol{r}) - \boldsymbol{A}(\boldsymbol{R}) - \boldsymbol{A}(\boldsymbol{r}). \qquad (3.2.4)$$

Note that these do not describe the fields at any position, but merely express the difference between the sum of fields at two positions and the field at the sum of those two positions.
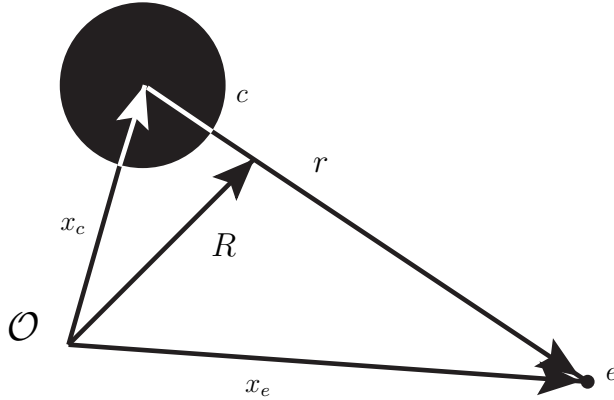
3.3   Hamiltonian and perturbation terms

Figure 3.1: *Schematic of the coordinates used in this paper. $\mathcal{O}$ denotes the origin. $\boldsymbol{x}_e$ and $\boldsymbol{x}_c$ are the position vectors of the electron and core respectively in the Ioffe-Pritchard frame. $\boldsymbol{r}$ and $\boldsymbol{R}$ denotes the relative and center of mass coordinates respectively. Since the mass is almost entirely contained in the core we approximate $\boldsymbol{R}$ with $\boldsymbol{x}_c$.*

Our approach builds on a spin and minimal coupling scheme for the valence electron with position $\boldsymbol{x}_e$, momentum $\boldsymbol{p}_e$ and mass $m_e = 1$ and the core with position $\boldsymbol{x}_c$, momentum $\boldsymbol{p}_c$ and mass M in an external magnetic field. We reexpress this Hamiltonian using Jacobi coordinates $((x, y, z)^T = \boldsymbol{r} = \boldsymbol{x}_e - \boldsymbol{x}_c,$ $(X, Y, Z)^T = \boldsymbol{R} = \boldsymbol{x}_e/M + \boldsymbol{x}_c$, see Fig. 3.1). Since the mass ratio is large, about

1.6×10^5 for ^{87}Rb, we identify the core $\boldsymbol{x}_c$ and center of mass coordinate $\boldsymbol{R}$ as an approximation. This leaves us with the Hamiltonian

$$
\begin{aligned}
\mathcal{H} =& \mathcal{H}_{\mathrm{ff}} + \boldsymbol{A}\left(\boldsymbol{R}+\boldsymbol{r}\right) \cdot \boldsymbol{p} + \boldsymbol{S} \cdot \boldsymbol{B}\left(\boldsymbol{R}+\boldsymbol{r}\right) \\
& + \frac{\boldsymbol{P}^2}{2M} + \frac{1}{M}\left[\boldsymbol{A}\left(\boldsymbol{R}+\boldsymbol{r}\right) - \boldsymbol{A}\left(\boldsymbol{R}\right)\right] \cdot \boldsymbol{P} \\
& + \frac{1}{2}\boldsymbol{A}^2\left(\boldsymbol{R}+\boldsymbol{r}\right) + \frac{g_I}{2}\boldsymbol{I} \cdot \boldsymbol{B}\left(\boldsymbol{R}\right),
\end{aligned} \tag{3.3.1}
$$

with $\mathcal{H}_{\mathrm{ff}}$ being the (field free) fine structure Hamiltonian, $\boldsymbol{P}$ the center of mass momentum operator, $\boldsymbol{S}$ the electron spin, $\boldsymbol{I}$ the nuclear spin and g_I the nuclear Landé g-factor. We apply degenerate perturbation theory in the fine structure basis $|\kappa\rangle = |nLjm_j\rangle$ to this Hamiltonian, coupling to all states within one L-manifold.

At this point, in previous work [May09b, May09a] a unitary transformation is applied: $U_{\mathrm{lit}} = \exp(-i(\boldsymbol{B}_c \times \boldsymbol{r}) \cdot \boldsymbol{R}/2) = \exp(i\boldsymbol{A}_c(\boldsymbol{R}) \cdot \boldsymbol{r})$. This removes, what they consider the most dominant perturbation terms in the linear field approximation, $\boldsymbol{A}_c^2(\boldsymbol{R})/2$ and $-\boldsymbol{A}_c(\boldsymbol{R}) \cdot \boldsymbol{p}$, which are of similar magnitude but opposite sign, making the perturbative treatment more robust. However, this transformation complicates the diamagnetic terms unnecessarily. If we consider Eq. (20) in Ref. [May09b] along the line $X = Y$ we obtain $E_\kappa^{(2)}(\boldsymbol{R}) \approx C_z \mathcal{G}^2 X^4$ with $C_z \approx -1/2$, within 10% for $35 \leq n \leq 45$ and $l \leq 4$. But if we consider the term $\boldsymbol{A}_l^2(\boldsymbol{R})/2 = \mathcal{G}^2 X^2 Y^2/2$, which is implicitly neglected by MLS, we find the same value but with opposite sign along $X = Y$. Thus the main Rydberg contribution is countered by a neglected term.

Instead we use a more general unitary transformation that does not rely on any explicit field to be introduced, and is inspired by the previous

$$
U = \exp\left(i\boldsymbol{A}(\boldsymbol{R}) \cdot \boldsymbol{r}\right). \tag{3.3.2}
$$

We apply this to the Hamiltonian: $H = U\mathcal{H}U^\dagger$. The transformation (3.3.2) removes the terms $\boldsymbol{A}^2(\boldsymbol{R})/2$ and $-\boldsymbol{A}(\boldsymbol{R}) \cdot \boldsymbol{p}$, in their entirety in contrast to the standard transformation U_{lit}.

The resulting Hamiltonian can be split into four parts $(H = H_{R,r} + H_R + H_r + H_{r,P})$ according to their dependence on the Jacobi operators

$$
\begin{aligned}
H_{R,r} =& H_{\mathrm{ff}} + \left(\boldsymbol{S} + \frac{1}{2}\boldsymbol{L}_r\right) \cdot \boldsymbol{B}(\boldsymbol{R}) + \frac{1}{2}\tilde{\boldsymbol{A}}^2(\boldsymbol{R},\boldsymbol{r}) \\
& + \boldsymbol{A}(\boldsymbol{r}) \cdot \tilde{\boldsymbol{A}}(\boldsymbol{R},\boldsymbol{r}) + H_{\mathrm{small}},
\end{aligned} \tag{3.3.3}
$$

$$
H_R = \frac{\boldsymbol{P}^2}{2M} + \frac{1}{2}g_I \boldsymbol{I} \cdot \boldsymbol{B}(\boldsymbol{R}), \tag{3.3.4}
$$

$$
\begin{aligned}
H_r =& \left(\boldsymbol{B}_l(\boldsymbol{r}) + \boldsymbol{B}_q(\boldsymbol{r})\right) \cdot \boldsymbol{S} + \left(\boldsymbol{A}_l(\boldsymbol{r}) + \boldsymbol{A}_q(\boldsymbol{r})\right) \cdot \boldsymbol{p} \\
& + \frac{1}{2}\boldsymbol{A}^2(\boldsymbol{r}),
\end{aligned} \tag{3.3.5}
$$

$$
H_{r,P} = \frac{1}{M}\left[\boldsymbol{A}(\boldsymbol{R}+\boldsymbol{r}) - \boldsymbol{A}(\boldsymbol{R}) + \nabla_R\left(\boldsymbol{A}(\boldsymbol{R}) \cdot \boldsymbol{r}\right)\right] \cdot \boldsymbol{P}, \tag{3.3.6}
$$

with H_{small} [2] collecting some terms we can neglect in perturbation theory, and $\boldsymbol{L}_r$ being the electron angular momentum operator. For the ground state, only the $\boldsymbol{B}(\boldsymbol{R})$ term of Eq. (3.3.3) contributes significantly to the energy, as $\langle |\boldsymbol{r}| \rangle \approx 0$, and the magnetic trapping field is assumed to be constant across the atom. This is sharply contrasted for large Rydberg states, where terms dependent on $\boldsymbol{r}$ become important, since $\langle |\boldsymbol{r}| \rangle \propto n^2$ is large, and the terms

$$\frac{1}{2} \tilde{\boldsymbol{A}}^2(\boldsymbol{R}, \boldsymbol{r}) + \boldsymbol{A}(\boldsymbol{r}) \cdot \tilde{\boldsymbol{A}}(\boldsymbol{R}, \boldsymbol{r}) + H_r, \tag{3.3.7}$$

which we call the "Rydberg term", become important. These terms are mostly extra terms compared to the MLS approach, and together constitute the Rydberg specific part of the Hamiltonian.

We work in a frozen gas setting where $P/M \approx 0$. This has the direct consequence that we can neglect the $H_{r,P}$. Furthermore, this setting is well explored with the Born-Oppenheimer approximation, where the electrons are assumed to react instantly to any core movement. In accordance with the Born-Oppenheimer approximation we assume the eigenstates to be product states of a $\boldsymbol{r}$ dependent part and a $\boldsymbol{R}$ dependent part

$$|\psi\rangle = |\psi_{\boldsymbol{r}}\rangle |\psi_{\boldsymbol{R}}\rangle = \sum_{\kappa} c_{\kappa} |\kappa\rangle |\psi_{\boldsymbol{R}}\rangle, \tag{3.3.8}$$

where c_{κ} are expansion coefficients for $\psi_{\boldsymbol{r}}$ in the fine structure basis.

By applying the electronic parts (i.e. the parts dependent on the relative coordinate) of the Hamiltonian, we find an energy dependent on the core position $\boldsymbol{R}$

$$(H_{R,r} + H_r) |\psi\rangle = E(\boldsymbol{R}) |\psi\rangle. \tag{3.3.9}$$

We specifically use degenerate perturbation theory to find the electronic energies $E(\boldsymbol{R})$ at any given core position $\boldsymbol{R}$. We use a set of all fine structure states $|\kappa\rangle = |nLjm_j\rangle$ (the eigenstates of H_{ff}), within one n, L- manifold, as basis for our perturbative treatment, as the energy contribution from the fine structure Hamiltonian is, by far, most dominant. We have found that coupling between states with different n or L quantum numbers is not significant for the parameter space we are considering, and we have not included this in our model.

The complexity of this computation can be greatly reduced by carefully examining and understanding the couplings between different states. The expressions become quite simple and $S_{1/2}$ states can be solved analytically. We include

---

[2] We have neglected a number of terms in Eq. (3.3.3), part of the perturbation Hamiltonian

$$H_{\text{small}} = \boldsymbol{S} \cdot \tilde{\boldsymbol{B}}_q(\boldsymbol{R}, \boldsymbol{r}) + \frac{\alpha^2}{2r} \frac{dV_l(r)}{dr} (\boldsymbol{A}(\boldsymbol{R}) \times \boldsymbol{r}) \cdot \boldsymbol{S}$$
$$+ \frac{i}{2} \mathcal{G} \big(X \, [H_{\text{ff}}, yz] + Y \, [H_{\text{ff}}, xz] \big)$$
$$+ \frac{i}{2} \partial_j^R \boldsymbol{A}_{q,k}(\boldsymbol{R}) \, [H_{\text{ff}}, r_j r_k] + \boldsymbol{A}_q^{(2)}(\boldsymbol{R}, \boldsymbol{r}) \cdot \boldsymbol{p},$$

which have all been estimated to give only minor contributions. With the exception of $\boldsymbol{S} \cdot \tilde{\boldsymbol{B}}_q(\boldsymbol{R}, \boldsymbol{r})$ term, all have higher order than 3 in the relative coordinates.

mixing between different j states within one L manifold, as they are sufficiently close in energy for the principal quantum numbers of interest.

Since the energy in Eq. (3.3.9) is dependent on the core position $\boldsymbol{R}$ we interpret it as a potential and construct a total potential W seen by the core

$$\langle \psi_{\boldsymbol{r}} | H | \psi \rangle = [H_R + E(\boldsymbol{R})] | \psi_{\boldsymbol{R}} \rangle$$
$$= [T_R + W(\boldsymbol{R})] | \psi_{\boldsymbol{R}} \rangle. \tag{3.3.10}$$

We call these potentials $W(\boldsymbol{R})$ Potential Energy Surfaces (PES). Since the micro-traps are designed to trap ground state atoms with only little spatial extent, it can be expected that trapping is mostly provided by the unperturbed Hamiltonian. However, there are exceptions leading to anti-trapping, as we will explain below.

3.4 Potential energy surfaces

We have calculated PES states that are reachable via a standard two-photon excitation process (S- and D states) from the rubidium ground state. We consider only states where $n \leq 80$ in order to keep perturbations small compared to the fine structure energies and to not break the Born-Oppenheimer approximation. For nD_j states mixing becomes significant when $n > 80$ and the finestructure states are no longer good quantum states. Thus the results for nD_j with $n > 80$ are unreliable. In the remainder of this paper we no longer use atomic units, but rather SI units.

In Fig. 3.2 we present the PES for the $70L_j$ states with all different positive m_j up to a distance of 0.75 μm from the trap center in the radial plane ($Z = 0$). These have been rescaled by $m_j g_j$ to make them comparable. The approximate symmetry with respect to the $X = Y$ line is due to this line being normal to the chip surface. In Fig. 3.3 we see the Z dependence of the PES for the same states to a distance of 4 μm from the trap center along the $X = Y = 0$ line. The choice of the $70L_j$ states is motivated by being well within the limits of our methods while the high n makes the Rydberg specific contributions clearly visible. This is seen in the strong dependence on the angular state, which is not evident for $n < 40$. When going to even higher n these effects become more pronounced and we eventually loose trapping for the $nD_{3/2}$ potentials, whereas the $nD_{5/2}$ states transition to quartic trapping potentials.

The $nS_{1/2}$ state trapping potentials do remain fairly similar to that of the ground state, not surprising as the electron is more tightly confined near the core.

The $70D_{3/2}$ states stand out among the PES by being antitrapping on the micrometer scale in both the $Z = 0$ plane and along the $X = Y = 0$ line. The PES of these states are more strongly influenced by the diamagnetic terms in the Hamiltonian, leading to both the antitrapping behavior and the structure in the positive potential region of the $m_j = 1/2$ state, by coupling to (j, m_j)-states of different angular symmetry. This structure makes the state unsuitable for quantum simulation but shows the importance of the Rydberg nature of the atom to the PES.

We see a small bump near the origin in the PES of the $70D_{5/2}$, $m_j = 1/2$ state. For higher n this bump becomes a regular peak turning the potential a Mexican hat shape.
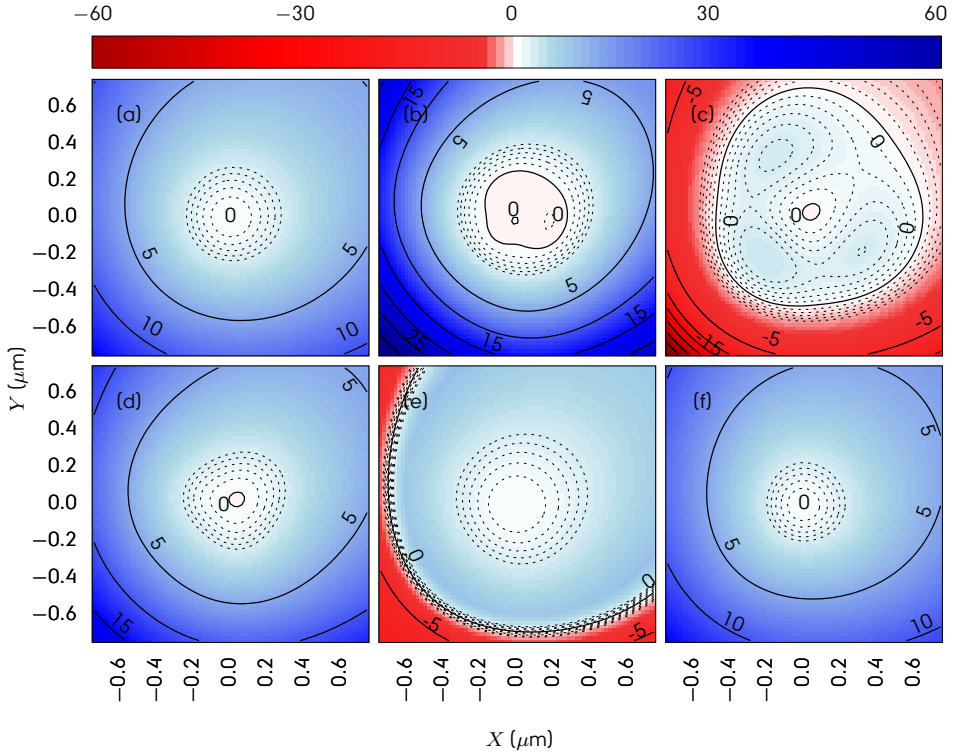
Figure 3.2: *Potential Energy Surfaces (PES) for the different angular states with $n = 70$ in the Ioffe-Pritchard plane ($Z = 0$) scaled by $m_j g_j$. These represent results for a typical magnetic potential of the hexagonal magnetic lattice. Solid contours at every 5 MHz and dashed contours at every 0.2 MHz in the interval -1 to 1 (limits included) are shown. Near the origin we observe positive curvature, meaning that the state is trappable, for all but the $70D_{5/2}$ with $m_j = 1/2$ state; where a small bump indicates a crossover to a Mexican Hat type potential. At higher n this will be more pronounced. For both $70D_{3/2}$ states we observe strong downwards gradients for large $|R|$, due to the strong influence of the diamagnetic term. The noticeable asymmetry in the plots is due to the fact that the coordinates are rotated with respect to the atom chip surface. The $X = Y$ direction is normal to the surface.*

In our analysis of the PES of the $n = 35$, 45, 55, 65, and 75 states, we fitted a polynomial to the contributions of the Rydberg specific terms in Eq. (3.3.7). This showed that, though highly state dependent, the effect of the Rydberg terms can be reduced to an offset and an R^2 dependent term for the $nS_{1/2}$ and $nD_{5/2}$ states. When $n > 73$, however, this simple picture fails for the $nD_{3/2}$ states, and higher order terms are needed to describe the behavior.

We predict that one can encounter this effect in spectroscopic measurements, even for weaker traps, as long as the magnetic field is well described by the second order expansion of our model.
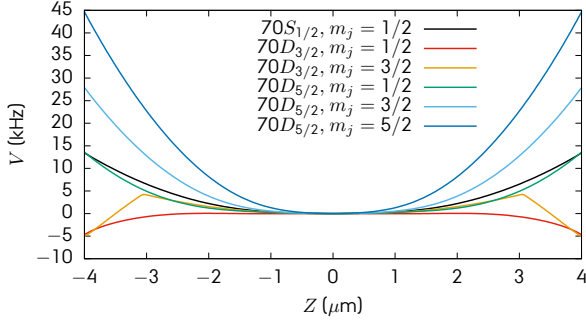
Figure 3.3: *Trapping potential in the Z direction at $X = Y = 0$ for the different angular states with $n = 70$. Parameters of the hexagonal lattice microtraps have been used [Leu14]. Trapping along this direction is much weaker than in the X, Y plane. All states shown have local, albeit weak, minima near $Z = 0$.*

Our results show that in general, the PES of the $nS_{1/2}$ and $nD_{5/2}$ states are always trapping on micrometer length scales for atoms with $n < 80$. The $nD_{3/2}$ states also show trapping PES, but for $n > 50$ the PES become of antitrapping nature on the micrometer scale, and we only observe local trapping on sub micrometer scales, and rich structure appearing near the center of the PES, when $m_j = 1/2$ and $n > 60$.

3.5 Trapping conditions

We now analyze the trapping conditions for different Rydberg states as function of principal quantum number n and angular state. We investigate in particular whether Rydberg states with trapping conditions identical to the ground state conditions can be found. This is particularly relevant for the implementation of various quantum information protocols based on Rydberg interactions. Rydberg atoms and ground state atoms experience different trapping potentials, which leads to motional decoherence. We denote a Rydberg atom in internal state $|r\rangle = |nLjm_j\rangle$ in a certain motional state $|\nu\rangle$ by $|r, \nu\rangle$. During the Rydberg excitation that same motional state $|\nu\rangle$ will be a non-stationary state in the Rydberg trap. When de-exciting the atom the motional state will have changed under time evolution and no longer be identical to $|\nu\rangle$. Therefore it is of great interest if we can suppress this decoherence mechanism by realizing conditions of magic trapping, where ground and Rydberg state atoms would experience identical trapping potentials.

First, we define the rotated coordinates away from the surface of the chip $\tilde{X} = \sqrt{\frac{1}{2}}(X + Y)$ and $\tilde{Y} = \sqrt{\frac{1}{2}}(X - Y)$ parallel to the surface.

$$V(\tilde{X}, \tilde{Y}, Z) = C + \frac{1}{2}m\omega_{\tilde{X}}^2(\tilde{X} - \tilde{X}_0)^2 + \frac{1}{2}m\omega_{\tilde{Y}}^2(\tilde{Y} - \tilde{Y}_0)^2$$
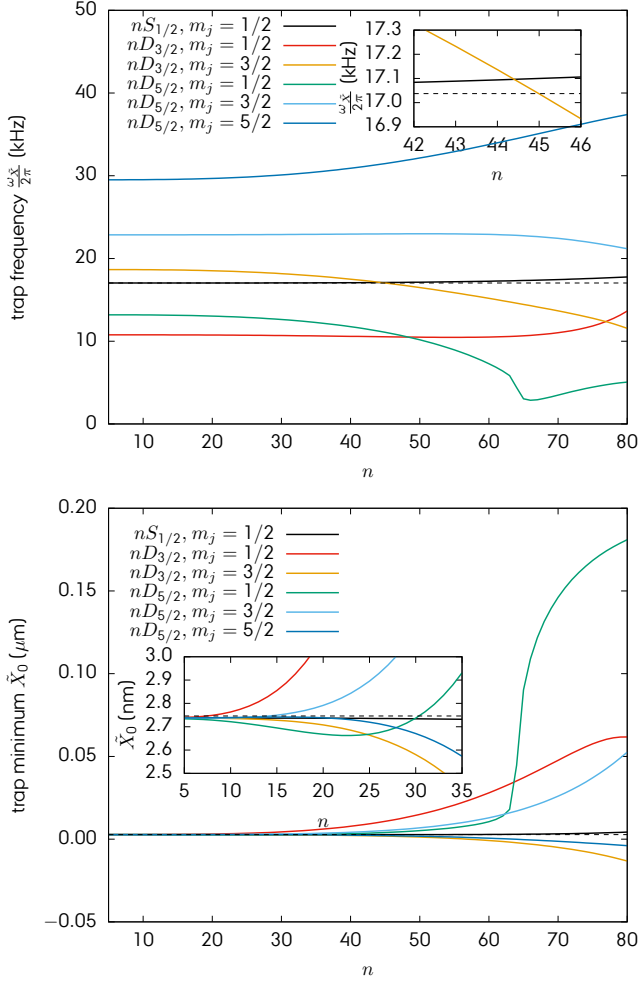$$+ \frac{1}{2}m\omega_Z^2(Z - Z_0)^2, \tag{3.5.1}$$

Figure 3.4: *(a) Radial trap frequency and (b) position of the local potential minimum as a function of n, both in the $\tilde{X}$ direction. The shift of the trap minimum away from the origin occurs gradually for low n but becomes very rapid for larger n. The rapid shift indicates crossover to a Mexican hat type potential. Dashed lines indicate the value of the $5S_{1/2}$, $m_j = 1/2$ state in all cases. Similar results are found in the $\tilde{Y}$ direction; whereas in the Z direction the trap is an order of magnitude weaker. Of special interest is the $45D_{3/2}$, $m_j = 3/2$ state, where the trapping frequency is very close to that of the ground state. This and the small value of X_0 lead to magic trapping conditions for the $45D_{3/2}$, $m_j = 3/2$ state.*

where C is some constant offset, $(\tilde{X}_0, \tilde{Y}_0, Z_0)$ is the minimum position of the trap and ω_i is the local trap frequency around the minimum in the $\tilde{R}_i$ direction. This is a good approximation over a distance of $0.3\mu m$ from the trap center, many times larger than the trap oscillator length. Analysis of the traps show that all states

have tens or hundreds of trap levels. With energy much lower than the potential walls, the center of mass will behave as in an infinitely deep potential. The lowest number of trap levels are found for the $nD_{3/2}, m_j = 1/2$ states, consistent with the antitrapping long range behavior.

Our analysis shows that the trap behaves harmonically for $n \leq 50$ and does not deviate significantly from the $n = 5$ trapping potential for any given angular state, see Fig. 3.4. In particular the changes in $nS_{1/2}$ state trapping frequency and minimum position remain insignificant over the whole n-range considered.

The $nD_{3/2}$ states show strong dependence on n and m_j. In the $m_j = 1/2$ states we find the trap bottom shift away from the origin but the effective trap frequency remains relatively stable until $n = 70$. The $m_j = 3/2$ states show consistently decreasing trap frequencies but the trap minima remain fairly centered. As seen from Fig. 3.4 magic trapping conditions, i.e. effective trapping similar to that of the ground state, are present for the $nD_{3/2}, m_j = 3/2$ states around $n = 45$. The effective trap frequency of these states are equal to that of the ground state in the $\tilde{X}$ direction. This means that the Rydberg excitation cycle can be performed with minimal motional decoherence. Since the PES for these states are nearly identical to that for the ground state, the CM wave function remains unchanged after the Rydberg excitation, see Fig 3.5.

The $nD_{5/2}$ states show rich behavior in the parameters of the effective trapping. The trap frequencies of states with $m_j = 1/2$ drop to around a quarter of the $n = 5$ value at $n = 66$. The minimum of the traps shift position away from the origin, very rapidly for $63 \leq n \leq 65$. Inspection of the PES shows that this is a crossover to a Mexican Hat type potential in the $Z = 0$ plane. The $m_j = 3/2$ state trapping frequencies remain stable, at around twice the value of the ground state trap frequency, across the entire n-interval considered, with a slight decrease for very large n. The minimum position shifts away from the origin. The $m_j = 5/2$ states show large, increasing trapping frequency, but no significant change in trap minimum position. The $nD_{5/2}$ states are not suitable for procedures requiring trap frequencies comparable to those of the ground state.

The trapping conditions that were found for the $\tilde{X}$ direction in Fig. 3.4 for the $45D_{3/2}, m_j = 3/2$ and nearby states (and similar conditions in the $\tilde{Y}$ and Z directions) are expected to strongly suppress motional decoherence in any gate protocol involving Rydberg excitation and de-excitation. A full analysis of gate fidelities should take into account the photon recoils upon (de-)excitation, considering also that these tight magnetic traps are in the Lamb-Dicke limit[Win98]. For the highest fidelities the anharmonicity of the traps may also play a role. Such full analysis of fidelities is beyond the scope of this paper.

As a first indicator, we have projected the motional ground state of the $5S_{1/2}$, $m_j = 1/2$ electronic state, denoted by $|g, 0\rangle$, onto the motional states of an electronically excited state,

$$|\psi\rangle = \sum_{\nu} |r, \nu\rangle \langle g, 0|r, \nu\rangle = \sum_{\nu} c_{\nu} |r, \nu\rangle, \qquad (3.5.2)$$

with $\nu = \{\nu_{\tilde{X}}, \nu_{\tilde{Y}}, \nu_Z\}$ being the motional quantum numbers in the indexed directions. We time evolve this projection $|\psi(t)\rangle = \exp(iHt/\hbar)|\psi\rangle$ and calculate the
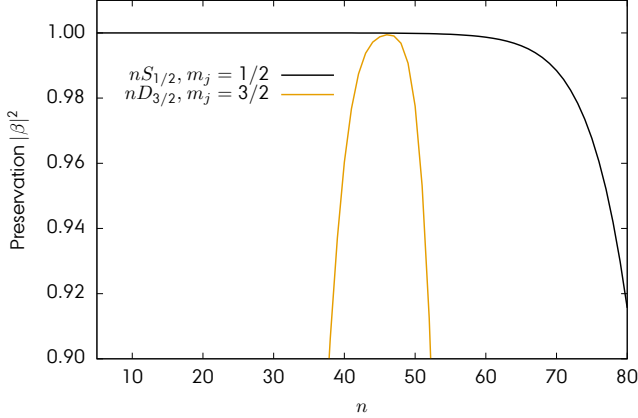
Figure 3.5: *Overlap of the center of mass ground state after 10 μs spent in an excited state, taking all directions into account. We bring the system into the Rydberg state and de-excite after 10 μs, we ignore all other decoherence effects like spontaneous emission. This determines the probability of finding the center of mass particle in the ground state after spending some time in a given excited electronic state.*

time delayed overlap

$$\begin{aligned}
\beta_t &= \langle \psi(0)|\psi(t)\rangle \\
&= \sum_\nu |c_\nu|^2 \exp\left[-i\left(\nu + \frac{3}{2}\right)\omega t\right],
\end{aligned} \tag{3.5.3}$$

where the coefficients c_ν are calculated using second order perturbation theory, and define the overlap of the state as $|\beta|^2 = |\beta_{10\mu s}|^2$. Thus $1 - |\beta|^2$ represents the probability of finding the atom in a different motional state after a 10 μs evolution time.

In Fig. 3.5 we see that this overlap reaches 0.9994, for the $46D_{3/2}, m_j = 3/2$ state, comparable to that of the $nS_{1/2}, m_j = 1/2$ states, which have overlaps exceeding 0.999 for $n \leq 58$. We have identified two angular configurations that are comparably good, around $n = 46$. Experiments therefore can choose between two angular states and therefore also between symmetric and directional blockade regions. The reason that the optimal overlap is found for $46D_{3/2}$, whereas Fig 3.4 would suggest $n = 45$ is due to a small shift of the trap minimum position.

This overlap allows for minimizing decoherence due to changes in effective trapping, making sure the effect of the excited state trap is not the limiting factor. This should be compared to losses due to other sources, which will be dominant, in particular spontaneous emission and transitions driven by black body radiation, with a lifetime of about 50 μs for the $n = 45$ states [Bet09].

3.6 Conclusion and outlook

We have studied Rydberg atoms in magnetic microtraps described by a second order expansion of the magnetic field. The magnetic microtraps are much tighter and have much stronger field gradients than more commonly used traps, such as Z-wire traps. This enhances the effects of the trap on the spatially extended Rydberg atoms.

Our work confirms the findings by Mayle *et al.* [May09b], that Rydberg atoms can indeed be magnetically trapped, and we have extended their model by including several new terms in the Hamiltonian, most importantly the diamagnetic term mixing the relative and center of mass coordinates. These terms constituted an unknown contribution to the trapping potentials of Rydberg atoms that, while negligible in weaker traps, are important in the context of microtraps. We have, however, also found the 'Rydberg term' of Ref. [May09b] to be almost zeroed by some of the additional terms.

We found that trapping of Rydberg atoms is possible for both S-states and D-states, but for high n effective trapping potentials become distorted, due to the anisotropic nature of the Rydberg contributions and the increased contribution from the diamagnetic terms.

We have found near-magic trapping conditions with more than 99% overlap for nS states with $n < 70$ and $nD_{3/2}$ states with $m_j = 3/2$ and $43 \leq n \leq 49$, with the highest overlap for the $n = 46$ state. This provides a choice between the two angular states, and therewith the angular dependence of the interaction. With magic trapping states available, a Rydberg equivalent of the Mølmer-Sørensen gate [Sø99, Sø00, Wan01], relying on such conditions, could be possible. Such a gate implementation will be of great value for quantum simulation and processing, and demands further research.

We have found that the spatially extended nature of Rydberg atoms has significant effects in the microtraps, and results significant modifications of the trapping potentials of the center of mass. In particular we have observed a strong n-dependence of the center of mass trapping potentials, with shallow trapping for $nD_{3/2}$ states and quartic trapping of $nD_{5/2}$ states.

Further research should consider the effect of the trap on the electronic wave function and, in turn, the effect on the Rydberg-Rydberg interaction.

Finally we remark that the methods employed in this work can readily be adapted to model other isotopes or elements. By adjusting the magnetic field parameters, we can model other magnetic trap configurations.

Acknowledgments

Phonon-mediated spin-spin interactions between trapped Rydberg atoms

R. V. Skannrup, R. Gerritsma and S. J. J. M. F. Kokkelmans

Abstract

We theoretically investigate the possibility of creating phonon-mediated spin-spin interactions between neutral atoms trapped in optical tweezers. By laser coupling the atoms to Rydberg states, collective modes of motion appear. We show that these can be used to mediate effective spin-spin interactions or quantum logic gates between the atoms in analogy to schemes employed in trapped ions. In particular, we employ Rydberg dressing in a novel scheme to induce the needed interaction, and we show that it is possible to replicate the working of the Mølmer-Sørensen entanglement scheme. The Mølmer-Sørensen gate is widely used in emerging quantum computers using trapped ion qubits and currently features some of the highest fidelities of any quantum gate under consideration. We find arbitrarily high fidelity for the coherent time evolution of the two-atom state even at non-zero temperature.

4.1 Introduction

The quest for scalable, high fidelity quantum logic gates is on [fla17]. State-of-the-art quantum gates based on trapped ions show the best fidelities in the field of quantum logic. A notable quantum gate protocol, inspiring this work, is the so-called Mølmer-Sørensen (MS) gate [Sø99, Wan01, Sø00], which uses trapped ions to create a quantum gate. It is based on phonon-mediated interactions, and in combination with the Hadamard- and $\pi/2$-gates the MS gate can be used to implement a C-NOT gate. This gate has been experimentally realized and has shown very high fidelities [Sac00, Lei03, Ben08, Kir09a, Gae16, Bal16], but trapped ion gates lack in terms of scalability, as it is difficult to control many trapped ions. On the other hand, quantum gates using neutral, highly excited Rydberg atoms [Jak00a, Mal15, Ise10a, Luk01a, Zha10, Wil10b, Cir95, Jau15], constitute a much more scalable platform [Saf16b, Saf10a], but show significantly lower experimental fidelities. Rydberg atom quantum gates rely on strong dipole-dipole interactions between electrically neautral Rydberg atoms to facilitate entanglement.

These considerations raise the question: "Can phonon-mediated interactions be used to implement quantum gates between neutral atoms in a similar way as between ions?" In this paper we will justify that the answer is "yes" and we present both a model and a recipe for the formation of maximally entangled Bell states of neutral atoms.

Phonon-mediated interactions between Rydberg atoms have been treated in a recently published paper by Gambetta *et al.* [Gam20]. This work, however, focuses on multi-body interactions in optical lattices, while our paper focuses on phonon-mediated two-body interactions, and we demonstrate that these interactions can be made independent of the temperature of the atoms in direct analogy to the trapped ion case [Sø99, Kir09b].

Although the external degrees of freedom play a central role in the trapped ion quantum system, their use has not been fully explored in ultracold Rydberg platforms. The recent [Gam20] work proposes the occurrence of non-binary interactions by electron-phonon coupling, while there has also been a number of works studying mediated interactions in self-assembled dipolar crystals *e.g.* [Büc07, Pup08]. Here we aim for a scalable high fidelity platform for the creation of Bell states using trapped, neutral, Rydberg-dressed rubidium atoms for our qubits, and rely on the strong dipole-dipole interactions to induce motion, like in the Mølmer-Sørensen trapped ion gate, where entanglement is achieved via phonon mediated interactions [Por04a, Fri08, Kim09a, Kim10, Ric14, Jur14, Zha17]. This is realized by transient mapping of the qubit states of the atoms onto a mode of collective motion. At the end of the sequence, the qubit state is disentangled from the motion again [Sø99, Wan01, Sø00]. This phonon-mediated interaction, treated in the original MS paper [Sø99], does not depend on the initial state of the phonon modes to lowest order. This makes for a reliable entanglement mechanism, even if the qubits are strongly coupled to a thermal reservoir [Sø99], and can possibly be used as the basis for a two-qubit quantum gate.

4.2 Model

Our approach starts with two (Rb) atoms with four distinct states each, two long lived states $|g_0\rangle$ and $|g_1\rangle$ and two Rydberg states $|r_0\rangle$ and $|r_1\rangle$, trapped in two well separated harmonic traps

$$V = \frac{1}{2}m\nu^2 \left[(x_1 - l/2)^2 + (x_2 + l/2)^2\right] + V_{\text{Ryd}}(x_1 - x_2), \qquad (4.2.1)$$

with x_j the position of atom j, l the distance between the the oscillator minima, m the mass of each atom and $V_{\text{Ryd}}(x) = C_6/x^6$ the state dependent, repulsive (in the case of rubidium nS-states) Rydberg-Rydberg van der Waals interaction. This can be rewritten in relative and center-of-mass (CM) coordinates

$$V = \frac{1}{2}\nu^2 \left[m_r(r - l)^2 + m_R R^2\right] + V_{\text{Ryd}}(r), \qquad (4.2.2)$$

where $m_r = m/2$ and r are the reduced mass $m_1 m_2/(m_1 + m_2)$ and relative coordinates and $m_R = 2m$ and R are the CM mass and coordinate.

In order to lift the degeneracy of the CM and relative modes, we will use Rydberg dressed qubit states. We therefore apply the excitation scheme sketched in Fig. 4.1, where the four internal states of the proposed qubits are coupled via four lasers (which could effectively be a combination of lasers in case of a two-photon transition). The parameter β is a small dimensionless number, indicating the ratio between the Rabi frequency for the ground state to ground state coupling connecting $|g_0\rangle$ and $|g_1\rangle$ and those of the dressing lasers, connecting $|g_j\rangle$ and $|r_j\rangle$ for $j = 0, 1$). Additionally, the Rabi frequency of the coupling laser that is connecting $|r_0\rangle$ and $|r_1\rangle$ is scaled by β^2. The interaction between the laser field and a single atom is described by the single atom Hamiltonian

$$H^{(1)} = \frac{\hbar\Omega}{1 + \beta^2} \times \qquad (4.2.3)$$

$$\left(e^{i(\eta_g(\hat{a}^\dagger + \hat{a}) - \omega_g t)}|g_1\rangle\langle g_0| \right.$$

$$+ \beta e^{i(\eta_0(\hat{a}^\dagger + \hat{a}) - \omega_0 t)}|r_0\rangle\langle g_0|$$

$$+ \beta e^{i(\eta_1(\hat{a}^\dagger + \hat{a}) - \omega_1 t)}|r_1\rangle\langle g_1|$$

$$\left. + \beta^2 e^{i(\eta_r(\hat{a}^\dagger + \hat{a}) - \omega_r t)}|r_1\rangle\langle r_0| \right) + \text{H.C.},$$

where β is the dressing parameter, Ω is the Rabi frequency, $\eta_l = k_l \cdot \hat{z}\sqrt{\hbar/2m\nu}$ is the lth transition Lamb-Dicke parameter (k_l is the wave number, $\hat{z}$ is a unit vector and $l = g, 0, 1, r$), $\hat{a}$ and $\hat{a}^\dagger$ are the ladder operators of the qubit trap and ω_l is the lth laser frequency. The exponential factors treat the effect of the lasers on the external/trap states, which we will initially ignore, and only consider their effect on the internal states, by expanding the exponentials in $H^{(1)}$ to zeroth order, denoted $\tilde{H}^{(1)}$.
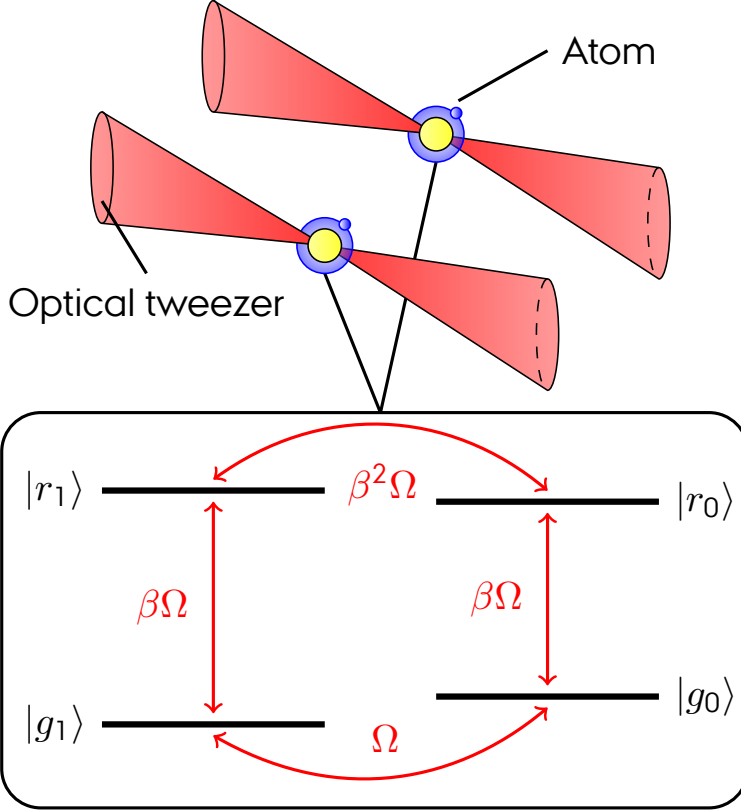
Figure 4.1: *Excitation scheme for using dressed qubits. The useful quantum states for qubits are the 'cross-dressed' states* $|O\rangle = (|g_0\rangle + \beta|r_1\rangle)/\sqrt{1 + \beta^2}$ *and* $|I\rangle = (|g_1\rangle + \beta|r_0\rangle)/\sqrt{1 + \beta^2}$.

The zeroth order single atom Hamiltonian has two dark states

$$|D_0\rangle = \frac{1}{\sqrt{1 + \beta^2}} \left(\beta|g_0\rangle - |r_0\rangle\right)$$

$$|D_1\rangle = \frac{1}{\sqrt{1 + \beta^2}} \left(\beta|g_1\rangle - |r_1\rangle\right), \tag{4.2.4}$$

which we will ignore, and two bright states

$$|O\rangle = \frac{1}{\sqrt{1 + \beta^2}} \left(|g_0\rangle + \beta|r_1\rangle\right)$$

$$|I\rangle = \frac{1}{\sqrt{1 + \beta^2}} \left(|g_1\rangle + \beta|r_0\rangle\right), \tag{4.2.5}$$

which we will use as qubit states, as $\tilde{H}^{(1)}|O\rangle = \hbar\Omega|I\rangle$ and $\tilde{H}^{(1)}|I\rangle = \hbar\Omega|O\rangle$. Initialization of the qubit states can be performed by appropriate laser pulses.

Rydberg dressing gives longer life times of our qubit states, compared to direct Rydberg excitation, and allows for a finer tuning of the interaction strength by means of adjusting the dressing parameter β in addition to choice of Rydberg state.

The interaction between the atoms and the laser light not only changes the internal state of the atom, but also their external state, *i.e.* the atoms gain momentum. Therefore we have to consider the full laser interaction Hamiltonian Eq. (4.2.3), including the exponential factors. Using the shorthand notation $\theta_l = \eta_l(\hat{a}^\dagger + \hat{a}) - \omega_l t$, and projecting $H^{(1)}$ onto the basis

$$S = (D_0, D_1, O, I) = \frac{1}{\sqrt{1 + \beta^2}} \begin{pmatrix} 0 & -\beta & 1 & 0 \\ -\beta & 0 & 0 & 1 \\ 1 & 0 & 0 & \beta \\ 0 & 1 & \beta & 0 \end{pmatrix},$$ (4.2.6)

constructed from the dark and qubit states of $\tilde{H}^{(1)}$, we get

$$S^{-1}H^{(1)}S = \hbar\Omega\Big(\beta(e^{-i\theta_0} - e^{-i\theta_g})|D_0\rangle\langle O|$$

$$+ \beta(e^{-i\theta_1} - e^{i\theta_g})|D_1\rangle\langle I| + e^{i\theta_g}|O\rangle\langle I|\Big) + H.C.,$$ (4.2.7)

ignoring terms higher than second order in β, since a realistic setup would be nS Rydberg states with $n \approx 100$, $l \approx 3\,\mu$m and $\nu \approx 2\pi \times 100$ kHz, we can expect $\beta < 0.1$, as we will explain below. Therefore neglecting these terms lead to errors on the order of 1%.

Additionally, assuming η_l to be small and taking the Lamb-Dicke approximation, we get

$$\Phi = \exp\left[-i\eta_k(\hat{a}^\dagger + \hat{a})\right] - \exp\left[-i\eta_l(\hat{a}^\dagger + \hat{a})\right]$$

$$\approx i\,(\eta_l - \eta_k)\,(\hat{a}^\dagger + \hat{a}) - \frac{1}{2}\,(\eta_l^2 - \eta_k^2)\,(\hat{a}^\dagger + \hat{a})^2.$$ (4.2.8)

We will here assume that η_0 and η_1 are not only small and comparable to $\eta_g \approx 0.05$, but in fact of equal absolute value. This is not only desirable, but also easily realizable as the Lamb-Dicke parameter can be tuned for two-photon transitions. With counter propagating dressing lasers and with Lamb-Dicke parameters close to that of the ground state to ground state coupling, $\eta_0 = \eta_g + \xi = -\eta_1$ (with dimensionless $|\xi| \ll \eta_g$), we can ensure that the exponential factors of the $|D_0\rangle\langle O|$ and $|D_1\rangle\langle I|$ terms in Eq. (4.2.7) are limited in absolute value, to leading order, by

$$\Phi \approx \beta\xi\left|i(\hat{a}^\dagger + \hat{a}) - \eta_g(\hat{a}^\dagger + \hat{a})^2\right|$$

$$\lesssim 0.001\left|i(\hat{a}^\dagger + \hat{a}) - \eta_g(\hat{a}^\dagger + \hat{a})^2\right|,$$ (4.2.9)

which we can neglect, for reasonably low vibrational states *i.e.* the CM mode quantum number $n_R < 10$, as they contribute on the order of 1% to the Hamiltonian, leaving

$$S^{-1}H^{(1)}S = \hbar\Omega e^{i(\eta_g(\hat{a}^\dagger + \hat{a}) - \omega_g t)}|O\rangle\langle I| + H.C.$$ (4.2.10)

With these approximations, $H^{(1)}$ only cycles between the two-qubit states. Allowing for a detuning of the ground state to ground state coupling and one of the dressing lasers, we add $D = -\hbar\Delta(|g_1\rangle\langle g_1| + |r_0\rangle\langle r_0|)$ to $H^{(1)}$, resulting in the qubit detuning

$$S^{-1}DS = -\hbar\Delta(|D_0\rangle\langle D_0| + |I\rangle\langle I|). \tag{4.2.11}$$

This dressing makes the Van der Waals interaction between the two atoms independent of state, while having long life time compared to bare Rydberg atom qubits. The Van der Waals interactions will lift the degeneracy of the CM and relative modes of motion, as the oscillator frequency of the CM mode remains unchanged and the relative mode frequency increases. This results in a simplified Hamiltonian, in the absence of laser light,

$$H_0 = \hbar\left[\nu_r\left(a_r^\dagger\hat{a}_r + \frac{1}{2}\right) + \nu\left(\hat{a}_R^\dagger\hat{a}_R + \frac{1}{2}\right)\right.$$
$$\left. + \sum_{\sigma\in S}\omega_\sigma|\sigma\rangle\langle\sigma|\right], \tag{4.2.12}$$

with ν_r the relative mode oscillator frequency, $\hat{a}_R$ ($\hat{a}_r$) and Hermitian conjugate are the CM (relative) mode ladder operators, the sum runs over the internal states and $\hbar\omega_\sigma$ is the energy of state σ.

The inter-particle Rydberg-Rydberg interaction will only affect the relative mode. The relative frequency and the shift in the relative minimum position are also a function of the trapping frequency ν and the distance between the traps l, and to fully characterize the mode splitting we have to take all four parameters ν, l, C_6, and β into account. We introduce the dressed interaction strength

$$W = \beta^4 C_6, \tag{4.2.13}$$

since the strength of the interaction between Rydberg dressed atoms is scaled by β^4 [ń17].

Ideally we would like to achieve a splitting ratio $\nu_r/\nu = \sqrt{3}$, as this would mimic to the ion-ion case. However, at the same time we have to minimize the shift in minimum position, realize sufficiently large life time (scaling with β^{-2}) and keep gate operation times low, therefore we have to consider splitting ratios smaller than $\sqrt{3}$. We find that the splitting needs to be larger than 1.15, in order to make a reliable transfer with good fidelity.

For a given dressed interaction strength W only one local minimum exists in the potential Eq. (4.2.2) for (real) positive relative coordinate, see Fig. 4.2. This minimum is located at r_{min}, which is the solution to

$$r_{\text{min}}^8 - lr_{\text{min}}^7 - 6\frac{\hbar W}{\nu^2 m_r} = 0. \tag{4.2.14}$$

Expanding the potential around this minimum, we find the splitting ratio $f_\nu = \frac{\nu_r}{\nu}$ as

$$f_\nu = \sqrt{8 - 7\frac{l}{r_{\text{min}}}}, \quad l > 0, \tag{4.2.15}$$
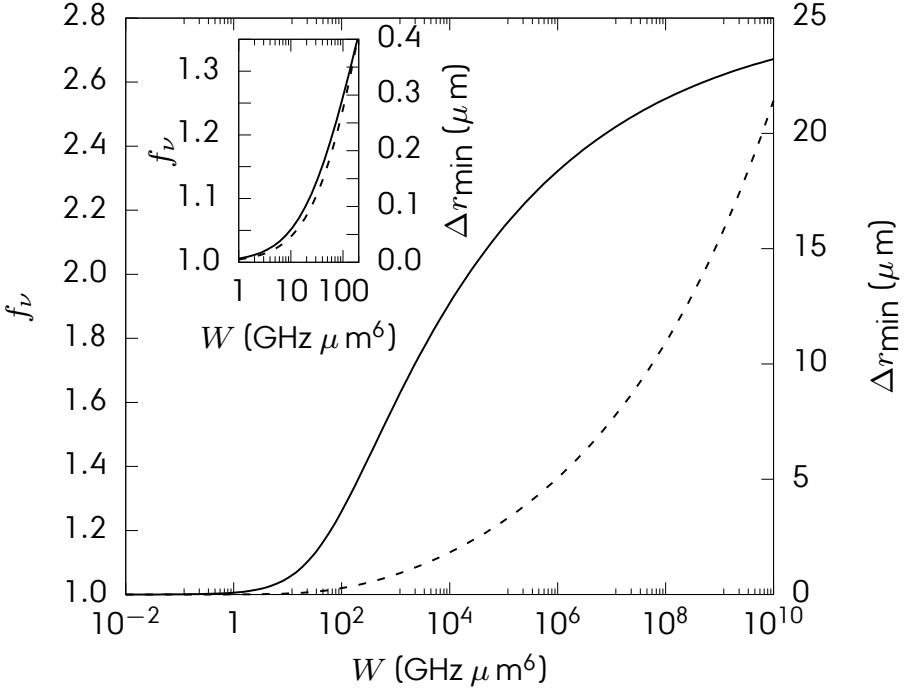
Figure 4.2: *Ratio of relative and CM mode oscillator frequencies $f_\nu = \nu_r/\nu$ as function of the dressed interaction strength W (solid) and the corresponding shift in relative mode minimum position (dashed). Inset shows the range of small W in greater detail.*

which is shown in Fig. 4.2. Since $r_{\min}$ grows monotonically for increasing W, the upper limit of the splitting fraction is $\sqrt{8}$ and lower limit is 1. This gives us a large range of controllable splitting fraction, limited the distance between the single atom traps. Inversely, it is more convenient to determine what strength is needed to result in a sufficient splitting fraction and the shift in minimum position can then be determined as

$$r_{\min} = \frac{7l}{8 - f_\nu^2}, \quad l > 0, \tag{4.2.16}$$

from which W can be derived, using Eq. (4.2.14). This treatment is limited by the validity of the harmonic approximation of the effective potential around the local minimum $r_{\min}$. However, for reasonable values of l and W the approximation holds for a large range around the minimum and a large number of bound states are consistent with this approximation.

4.3 Phonon interactions

We induce spin-spin interactions by letting both qubits interact with bichromatic laser light, slightly detuned both above and below resonance. Including the
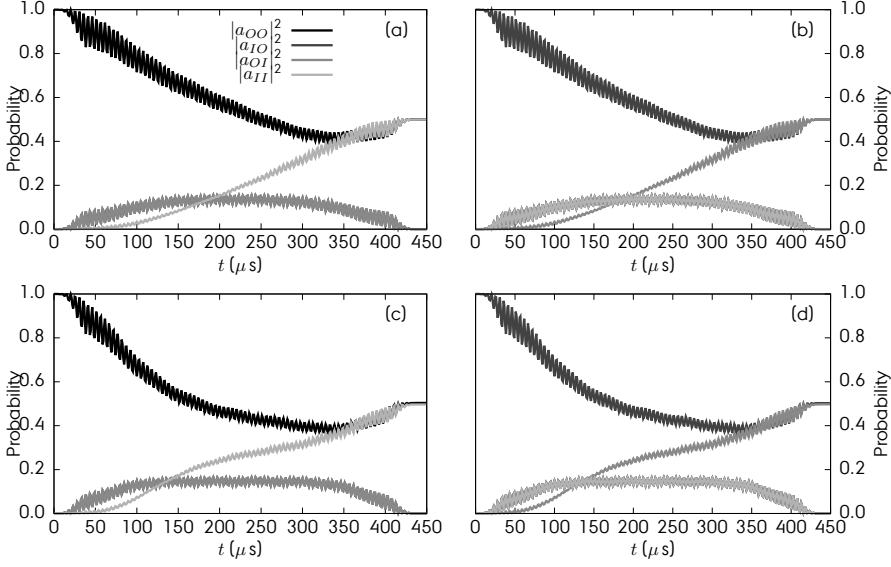
Figure 4.3: *Time evolution at finite temperature of the two-qubit populations with the vibrational motion traced out, obtained by propagating H_I (Eq. (4.3.3)). Labels denote the population of the indicated state, OO is the population of $|OO\rangle$ and so forth. The subfigures show populations of the time evolved states resulting in the creation of Bell states from pure qubit states $|OO\rangle \rightarrow \frac{1}{\sqrt{2}}(|OO\rangle + i|II\rangle)$ (a and c) and $|IO\rangle \rightarrow \frac{1}{\sqrt{2}}(|IO\rangle + i|OI\rangle)$ (b and d) at 0 temperature (a and b) and $5\,\mu K$ (c and d). The other input states mirror this behavior. These Bell states can be achieved with high fidelity at realistic cold atom temperatures, given the approximations made in this paper.*

photon recoil in the dressed frame, the effect of the laser light acting on both qubits, each with internal states $|O\rangle$ and $|I\rangle$ and trap states $|n_R, n_r\rangle$, where n_R (n_r) is the CM (relative) mode vibrational quantum number, can be expressed in the two-qubit Hamiltonian

$$H^{(2)} = \sum_j \sum_{k_j} \frac{\hbar\Omega_{k_j}}{2} \sigma_{+,j} e^{-i\omega_{k_j}t} \times$$

$$\exp\left[i\eta_{k_j} \left(\hat{a}_R^\dagger + \hat{a}_R - \frac{(-1)^j \sqrt{f_\nu}}{2}(a_r^\dagger + \hat{a}_r) \right) \right]$$

$$+ H.C., \tag{4.3.1}$$

where k_j is used to label the laser beams interacting with the j atom and $\sigma_{\pm,j}$ are the internal state step operator for atom j. We will use a sufficiently large mode splitting such that the relative mode is effectively frozen out. Changing to the interaction picture, we define the rotated creation operator

$$\hat{b}_j = e^{-i\nu t}\hat{a}_R - \frac{(-1)^j \sqrt{f_\nu}}{2} e^{-i\nu_r t}\hat{a}_r, \tag{4.3.2}$$

where $j = 1, 2$ is the atom site number, and get the two-qubit interaction picture Hamiltonian

$$H_I = \frac{\hbar}{2} \sum_j \sum_{k_j} \Omega_{k_j} e^{i\delta_{k_j}t} \sigma_{+,j} e^{i\eta_{k_j}\left(\hat{b}_j^\dagger + \hat{b}_j\right)}$$
$$+ \Omega_{k_j} e^{-i\delta_{k_j}t} \sigma_{-,j} e^{-i\eta_{k_j}\left(\hat{b}_j^\dagger + \hat{b}_j\right)}, \qquad (4.3.3)$$

where $\delta_{k_j} = \omega_{k_j} - \omega_{O \to I}$ is the detuning from the $|O\rangle \to |I\rangle$ transition. This Hamiltonian Eq. (4.3.3) reduces to a spin-spin interaction Hamiltonian [Kim09a, Por04a, Roo08]. Assuming $\eta_{k_j} = \eta$, $\Omega_{k_j} = \Omega$ and $|\delta_{k_j}| = \delta \approx \nu$, we can, in the Lamb-Dicke limit, simplify the interaction picture Hamiltonian

$$H_I \approx \frac{\hbar\Omega}{2} \sum_j \sum_{k_j} e^{i\delta_{k_j}t} \sigma_{+,j} \left[1 + i\eta \left(\hat{b}_j^\dagger + \hat{b}_j\right)\right] + H.C.,$$

which we further simplify by using

$$e^{i\delta_{k_j}t}\hat{b}_j = e^{i(\delta_{k_j} - \nu)t}\hat{a}_R - \frac{(-1)^j\sqrt{f_\nu}}{2}e^{i(\delta_{k_j} - \nu_r)t}\hat{a}_r, \qquad (4.3.4)$$

and by neglecting fast rotating terms. This results in

$$H_I \approx \Omega\left(2\hbar\cos(\delta t)J_x - \sqrt{2\hbar\nu m_R}\eta J_y\left(\cos(\nu t - \delta t)R\right.\right.$$
$$\left.\left. + \frac{\sin(\nu t - \delta t)}{m_R\nu}p_R\right)\right) - H_r, \qquad (4.3.5)$$

where J_x and J_y are collective spin operators, p_R is the CM mode momentum operator and

$$H_r = \sqrt{\frac{\hbar m_r\nu_r}{2}}\Omega\eta_r\tilde{J}_y\left(\cos(\nu_r t - \delta t)r\right.$$
$$\left. + \frac{\sin(\nu_r t - \delta t)}{m_r\nu_r}p_r\right), \qquad (4.3.6)$$

with p_r the relative mode momentum operator, $\tilde{J}_y = \sigma_{y,2} - \sigma_{y,1}$ and $\eta_r = \eta/\sqrt{f_\nu}$ the relative mode Lamb-Dicke parameter. If we ignore the fast rotating J_x term, we can write the propagator by virtue of the Zassenhaus formula

$$U(t) = \exp\left[-i\frac{\eta^2\Omega^2}{\nu - \delta}J_y^2 A(t)\right]\exp\left[-i\frac{\eta_r^2\Omega^2}{\nu_r - \delta}\tilde{J}_y^2 B(t)\right]$$
$$\times \exp\left[-i\alpha_R J_y\frac{\sin(\nu - \delta)t}{\nu - \delta}R\right]$$
$$\times \exp\left[-i\alpha_R J_y\frac{1 - \cos(\nu - \delta)t}{m_R\nu(\nu - \delta)}p_R\right]$$
$$\times \exp\left[i\alpha_r\tilde{J}_y\frac{\sin(\nu_r - \delta)t}{\nu_r - \delta}r\right]$$
$$\times \exp\left[i\alpha_r\tilde{J}_y\frac{1 - \cos(\nu_r - \delta)t}{m_r\nu_r(\nu_r - \delta)}p_r\right], \qquad (4.3.7)$$

with $\alpha_R = \sqrt{\frac{2m_R\nu}{\hbar}}\eta\Omega$ and $\alpha_r = \sqrt{\frac{2m_r\nu_r}{\hbar}}\eta_r\Omega$. $A(t)$ and $B(t)$ can be determined from the Schrödinger equation similar to $A(t)$ in Eq. (9) of ref. [Sø00].

At times $\tau_k = 2k\pi/(\nu - \delta)$ (with k an integer), the propagator Eq. (4.3.7) reduces to that of a spin-spin Hamiltonian

$$U(\tau_k) \approx \exp\left(-i\frac{\eta^2\Omega^2}{\nu - \delta}J_y^2 A(\tau_k) - i\frac{\eta_r^2\Omega^2}{\nu_r - \delta}\tilde{J}_y^2 B(\tau_k)\right), \qquad (4.3.8)$$

with exact equality if $\nu(f_\nu - 1)/(\nu - \delta)$ is an integer, however, the approximation always has merit if $\frac{\nu_r - \delta}{\nu - \delta} >> 1$.

We apply the Hamiltonian Eq. (4.3.3) in the time-dependent Schrödinger equation in the interaction picture with interaction picture state ψ_I [Por04b, Kim09b]. We set the Rabi frequency such that

$$\Omega = \frac{\nu - |\delta|}{2\eta} \cdot (1 + \alpha) \cdot \mathcal{T}(t), \qquad (4.3.9)$$

with alpha being a small dimensionless number and

$$\mathcal{T}(t) = \begin{cases} \sin^2\left(\frac{\pi t}{2t_s}\right) & t < t_s \\ 1 & t_s < t < t_p - t_s \\ \cos^2\left(\pi\frac{t + t_s - t_p}{2t_s}\right) & t_p - t_s < t < t_p \\ 0 & \text{otherwise} \end{cases} \qquad (4.3.10)$$

is a ramping function with t_s being the ramping time and t_p is the length of the pulse. In the original MS paper [Sø99] α is zero, as this ensures a $\pi/2$ rotation in phase space, but small adjustments to the Rabi frequency must be made to compensate for the (usually) weaker mode splitting achieved with the Rydberg interaction.

We have simulated the coherent time evolution starting from each of the four two-qubit states ($|OO\rangle$, $|OI\rangle$, $|IO\rangle$ and $|II\rangle$), in combination with a thermal ensemble of oscillator states at temperatures ranging from $0\,\mu$K to $5\,\mu$K, see Fig. 4.3 for examples. For this simulation, we have set all Lamb-Dicke parameters to $\eta = 0.05$, the detunings are set to $\delta = \pm 0.975\nu$, the dressed interaction strength $W = 50$ GHz μm^6, the trap frequency is $\nu = 2\pi \times 100$ kHz and the distance between the atoms is set to $l = 3\,\mu$m. The resulting splitting fraction is $f_\nu = 1.1745$ and atoms are pushed a further $r_{\min} = 0.1719\,\mu$m apart. In order to account for the off-resonant phase accumulation in the relative mode of motion, which is much closer in frequency compared to the trapped ion case, we need $\alpha = 0.1333$.

Our simulation shows reliable creation of Bell states, at all temperatures starting from all four of the internal two-qubit states. Tracing out the vibrational states, we find fidelties of Bell state creation to be higher than 0.999 for all input states even at non-zero temperature, under the approximations given above. We expect both the anharmonicity of the trap and non-magic trapping of the Rydberg part [Boe18] to influence the fidelity of the entanglement mechanism negatively: We estimate the trap quality issues to reduce the fidelity of Bell state creation by $\sim 2\%$. Further we expect the finite life-time of the Rydberg-dressed qubits, which

we estimate to influence the overall fidelity by $\sim 1\%$ for the $100S$ Rydberg level in rubidium-85. Additional losses and reductions in fidelity, due to neglected terms in the Hamiltonian are all below 1%, as they are all higher order in $\beta \sim 0.1$ or $\eta \sim 0.01$. By increasing the principal quantum number of the Rydberg level n of the dressed qubits, we expect these approximations to have a smaller effect on the overall fidelities, as $\beta \propto n^{-11/4}$. The lifetime of the Rydberg-dressed state will also increase [He90, Bra09, Bet09, ń17] as $\beta^{-2}n^3 \propto n^8\sqrt{n}$ by neglecting black body radiation, which of course limits the lifetime, but is not detrimental to this analysis, and can be reduced by means of a cryostat. This leaves only the quality of the traps as a significant source of errors, which can not simply be reduced by a change of the dressing parameter, and we expect this will be the limiting factor.

4.4 Conclusions

Recent years have seen many implementations of single atom traps, like optical tweezers [Lab16, Bar16, Kau12], holographic trapping [Xu10, Nog14], photonic crystals trapping [Yu14], cavity trapping [Pin00, Ye99], magneto optical traps [Yoo07] or magnetic microtraps [Wan16, Boe18]. Both magnetic microtraps and optical tweezer arrays [Lab16, Bar16] can be very tight with frequencies in the $10-100$kHz and the separation of two trap sites is on the μm scale. This development of tight single-atom traps with high filling factor forms the main motivation of this paper to investigate the MS gate for dressed Rydberg atoms. An interesting future development would be to employ a trapped ion crystal to mediate interactions between atomic qubits. This would combine long-range Coulomb interactions with the favorable scaling properties of neutral quantum devices [Sec16].

In this paper, we have shown that it should be possible to implement a Mølmer-Sørensen gate between two atoms trapped in tweezers. Combined with single qubit gates, the MS gate forms a universal set of quantum gates that has been implemented in trapped ions with very high fidelity [Sø99, Wan01, Sø00]. Our work shows, that it should be possible to extend its use to neutral atomic systems, that have much better scalability prospects. We have shown that, by appropriate choices of Rydberg level and dressing parameters, it is possible to create maximally entangled states with qubits consisting of Rydberg-dressed atoms in a Boltzmann-distributed statistical mixture of oscillator states, with experimentally realistic laser parameters, and we have quantified the order of magnitude of the errors. Besides the quantum gate described in this work, the scheme may be beneficial for the creation of atomic quantum simulators of quantum spin models [Wei10]. Here the tweezer setup offers in particular the benefit of creating nearly arbitrary trapping geometries [Gam20].

During the preparation of this paper, we became aware of a related work by Gambetta et al. [Gam20], which focuses on many-body interactions in tweezer arrays. Our work has been conducted independently of Gambetta et al. and focuses instead on two-body interactions.

Acknowledgments

Three-level rate equations in cold, disordered Rydberg gases

R. V. Skannrup, T. v Weerden, Y. vd Werf, T. Johri, E. J. D. Vredenbregt and
S. J. J. M. F. Kokkelmans

Abstract

We have investigated formation of structures of Rydberg atoms excited from
a disordered gas of ultra-cold atoms, using rate equations for two-photon
Rydberg excitation in a single atom without eliminating the intermediate state.
We have explored the validity range of these rate equations and defined a
simple measure to determine, whether our model is applicable for a given set
of laser parameters. We have applied these rate equations in Monte Carlo
simulations of ultra-cold gases, for different laser beam profiles, and compared
these simulations to experimental observations and find a general agreement.

5.1 Introduction

Highly excited atoms, generally referred to as Rydberg atoms, show extreme features such as long life times and strong dipole interactions, first observed in 1981 [Rai81]. As a result of these strong interactions, a Rydberg atom will block its neighbors from being excited, as the Rydberg level is moved out of resonance with the excitation laser. This blockade effect, first observed in 2009 [Urb09], has been proposed [Jak00b, Luk01b] as the mechanism for a two q-bit quantum gate, specifically a CNOT gate first demonstrated in 2010 [Ise10b]. Rydberg atoms have also been proposed as a many-body spin model quantum simulator [Wei10], and realized [Lab16]. In addition, the opposite mechanism, known as facilitation, is also possible [Les14, Les13, Val16], and is characterized by resonant excitation of Rydberg atoms at specific distances from existing Rydberg atoms. An in depth review of quantum information with Rydberg atoms is available [Saf10b].

Properties of Rydberg ensembles are often studied through measuring counting statistics such as the Mandel Q-parameter and spectra [Man79, Sch14, Mal14]. From these results different phase transitions can be recognized, for instance between a facilitation and blockade regime, which was already predicted for systems in equilibrium [Wei08a]. Another method to study Rydberg atoms is by measuring spatial correlations through spatial imaging [Sch12, Hi3]. Often the three-level system is simplified to a two-level system, which is only possible if a large laser detuning is used [Sha80, Bri07]. However, no matter how simple an atom description is, the state space grows exponentially in the number of atoms (just like with qubits) and one must still find a way to make many-body calculations feasible. We translate the problem to a Markov process with a limited amount of possible transitions, characterized by transition rates, and then employ Monte Carlo techniques as done in [Ate07b].

This research was done with a specific experiment, described in [Eng14, Bij14], in mind, though it is not limited to describing this. In our lab in Eindhoven University of Technology the setup can trap rubidium atoms in a magneto-optical trap (MOT) and excite these to Rydberg states. The excitation region can be varied at will by means of a spatial light modulator (SLM) with good control of both shape and dimensionality. The excitation region does not have to be continuous or convex, but we will limit the work presented here to one and two dimensional boxes, as this is of more general value.

In order to describe the versatile experimental excitation conditions, we develop a Monte Carlo model based on three-level atoms capable of covering the range of laser parameters and excitation volume geometries available to the experiment. The (de-)excitation probabilities of the Monte Carlo simulation are based on rate equations, where the detunings and Rabi frequencies of both the Rydberg and intermediate states are tunable in the model. In addition to the laser parameters, also the choice of intermediate and Rydberg state is kept free, by having the spontaneous decay rates of both states and Van der Waals coefficient of the Rydberg as input parameters. The resulting single-atom rate equations go beyond a simple effective two-level treatment and are applicable to both resonant and off-resonant excitations. We have checked the validity of the model and set limits to the validity range. This general rate equation description of the single atom, dependent on the internal states of the surrounding atoms, can then be used to
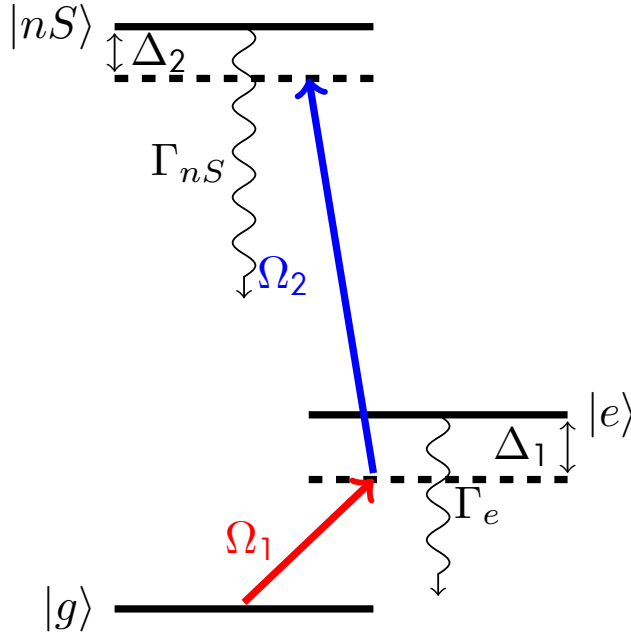
Figure 5.1: *Three level excitation scheme. A red laser (red) excites from the ground state $|g\rangle$ to an intermediate state $|e\rangle$ and is detuned by Δ_r. Another laser will excite from this intermediate level to the Rydberg level $|r\rangle$ and is detuned by Δ_b.*

describe the entire cloud in our Monte Carlo simulation, which we use to explain our experimental observations.

This paper is structured into seven sections. In section 5.2 we will derive the (de-) excitation rates for a single atom influenced by lasers as indicated Figure 5.1, and in section 5.3 we investigate the limits to the rate equation model (RE) in depth. In section 5.4 we investigate the differences in a Monte Carlo simulation, stemming from the three sets of rates. In section 5.6 we draw conclusions on this work.

5.2 Rate equations

We base our approach on N three level atoms with the Hamiltonian of the ith atom in the interaction picture given by

$$H^i = \frac{\hbar}{2}\bigg(-\Delta_1|e_i\rangle\langle e_i| - \Delta_2|r_i\rangle\langle r_i|$$
$$+ \Omega_1|g_i\rangle\langle e_i| + \Omega_2|e_i\rangle\langle r_i|\bigg) + \text{H.C.} \tag{5.2.1}$$

with $|e_i\rangle$ ($|r_i\rangle$) the ith atom being in the intermediate (Rydberg) state. Other authors have used similar rate equation models for two-level [Les14, Gï4] or
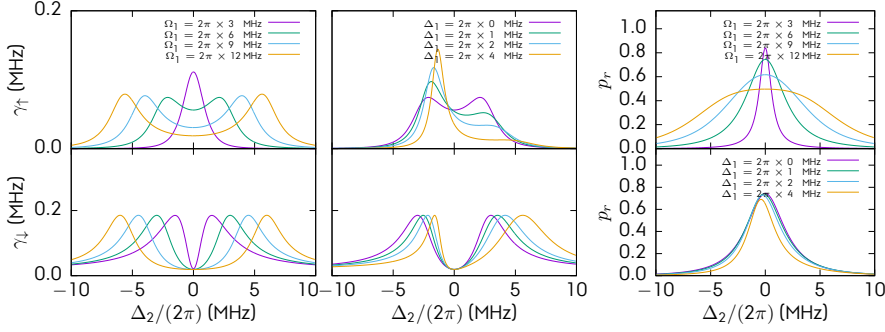
Figure 5.2: *Excitation rates (top) and deexcitation rates (bottom) vs blue detuning Δ_2, for different sets of laser parameters. Left column: Varying red Rabi frequency Ω_1, with constant blue Rabi frequency $\Omega_2 = 2\pi \times 0.4$ MHz and red detuning $\Delta_1 = 2\pi \times 0$ MHz. Middle column: Varying red detuning Δ_1, with constant blue Rabi frequency $\Omega_2 = 2\pi \times 0.4$ MHz and red Rabi frequency $\Omega_1 = 2\pi \times 6$ MHz. Right column: Steady state Rydberg populations, while varying red Rabi frequency (top) or red detuning (bottom). Other parameters are as in the corresponding (de-)excitation column.*

three-level [Ate07a, Ate07b, Hee12, Ate11] atoms. In [Ate07a, Ate07b, Hee12] an effective two-level system is achieved by fixing the intermediate level detuning at zero. Our three-level atom rate equation model allows for both the Rydberg and intermediate level detunings to be freely chosen input parameters, as well as both Rabi frequencies and the spontaneous decay rates. Further, we treat in some detail the limits of this free choice in the next section.

 We will base our calculations on rubidium-85, with the intermediate state being $5P_{3/2}$ and the Rydberg state $100S_{1/2}$ unless otherwise specified. These states have spontaneous decay rates $\Gamma_e = 2\pi \times 6.07$ MHz for the intermediate state and $\Gamma_r = 2\pi \times 0.003$ MHz for the Rydberg state. We call the laser associated with subscript 1 the probe laser and the one associated with subscript 2 the coupling laser. The interactions between atoms are given by

$$H_{\text{int}}^i = \frac{1}{2} \sum_{j \neq i}^{N} \frac{C_6}{r_{ij}^6} |r_j\rangle |r_i\rangle \langle r_i| \langle r_j|, \tag{5.2.2}$$

where r_{ij} is the distance between atoms i and j and C_6 is the Van der Waals coefficient scaling as the principal quantum number of the Rydberg state $|r\rangle$ to the power of 11. Since we apply the frozen gas approximation, we can assume the r_{ij}s to stay constant and the terms of H_{int}^i can be evaluated only once. The state of the system determines what terms to be included at any given time. We will assume that each atom can be modeled independently, with only an effective shift in local coupling detuning due to the interactions between Rydberg atoms. The entire effect of H_{int}^i is then captured by modifying the coupling detuning

$$\Delta_2 \to \Delta_2 + \frac{1}{\hbar} \langle s | H_{\text{int}}^i | s \rangle = \Delta_{\text{eff}}^i(s), \tag{5.2.3}$$

where $|s\rangle$ is the state of the full N atom system, if atom i is excited.

Using these we find the master equation (ME) of atom i in Lindblad form

$$\frac{d}{dt}\rho = -\frac{i}{\hbar}[H^i(s), \rho] + \mathcal{L}(\rho), \qquad (5.2.4)$$

where $H^i(s)$ given by eq. (5.2.1) with the replacement eq. (5.2.3) and Liouvillian

$$\mathcal{L}(\rho) = \Gamma_e |e_i\rangle\langle g_i| \rho |g_i\rangle\langle e_i| - \frac{\Gamma_e}{2}\{\rho, |e_i\rangle\langle e_i|\}$$
$$+ \Gamma_r |r_i\rangle\langle e_i| \rho |e_i\rangle\langle r_i| - \frac{\Gamma_r}{2}\{\rho, |r_i\rangle\langle r_i|\}, \qquad (5.2.5)$$

and $H^i(s)$ being the Hamiltonian in eq. (5.2.1) with Δ_2 replaced by the state dependent effective detuning eq. (5.2.3).

Rewriting the density matrix of a single atom in vector form, the effective time evolution operator is

$$\dot{\boldsymbol{\rho}} = \mathcal{R}\boldsymbol{\rho} = \begin{pmatrix} \mathcal{R}_p & L \\ L^T & \mathcal{R}_c \end{pmatrix} \boldsymbol{\rho}, \qquad (5.2.6)$$

with $\boldsymbol{\rho}^T = (\rho_{gg}, \rho_{ee}, \rho_{rr}, \rho_{ge}, \rho_{er}, \rho_{gr}, \rho_{eg}, \rho_{re}, \rho_{rg})$, $\mathcal{R}_p$ is a 3×3 matrix taking population to populations, $\mathcal{R}_c$ is a 6×6 matrix taking coherences to coherences and L is a 3×6 matrix taking coherences to populations. Adiabatically removing the coherences, we can write the optical Bloch equations

$$\dot{\boldsymbol{p}} = \left(\mathcal{R}_p - L\mathcal{R}_c^{-1}L^T\right)\boldsymbol{p} = Q\,\boldsymbol{p}, \qquad (5.2.7)$$

where $\boldsymbol{p} = (p_g, p_e, p_r)^T$ are the populations (ρ_{gg}, ρ_{ee} and ρ_{rr}) of the ith atom. Our analysis has shown that, for laser parameters where adiabatic elimination of the coherences is valid, the elements of Q solely associated with the dynamics between p_g and p_e are larger than those associated with dynamics of p_r by two or three orders of magnitude. We will call the terms associated with the dynamics of p_r the 'small' terms of Q.

The general solution to such a homogeneous system of coupled differential equations is known

$$\boldsymbol{p} = \sum_k \boldsymbol{v}_k \exp\left(-\lambda_k t\right), \qquad (5.2.8)$$

with λ_k ($\boldsymbol{v}_k$) the eigenvalues (-vectors) of Q, and the sum running over all eigenvalues. At sufficiently long time, all but one (non-zero) eigenvalues have dampened out, and we know that $\dot{p}_r = \alpha \dot{p}_e$, where $|\alpha| \gtrsim 1$, since only one eigenvector contributes to the derivative.

From this we can express p_e in terms of p_r and Q

$$p_e = \frac{(0, 1, 0) \, Q \, (1, 0, 0)^T}{(0, 1, 0) \, Q \, (-1, 1, 0)^T} \, (1 - p_r), \qquad (5.2.9)$$

be neglecting the small terms of Q

69

We define excitation rate $\gamma_\uparrow$ and deexcitation rate $\gamma_\downarrow$, such that

$$\dot{p}_r = \gamma_\uparrow(p_g + p_e) - \gamma_\downarrow p_r = \gamma_\uparrow(1 - p_r) - \gamma_\downarrow p_r, \tag{5.2.10}$$

which can be found by substituting eq. (5.2.9) into eq. (5.2.7) to get

$$\gamma_\uparrow = (0, -\xi, 1) \, Q \, (1, 0, 0)^T \tag{5.2.11}$$

$$\gamma_\downarrow = (0, 0, 1) \, Q \, (\xi - 1, -\xi, 1)^T. \tag{5.2.12}$$

with

$$\xi = \frac{(0, 1, 0), Q \, (-1, 0, 1)^T}{(0, 1, 0) \, Q \, (-1, 1, 0)^T}. \tag{5.2.13}$$

For the steady state solution the time derivative is the null-vector, and we get

$$p_r^\infty = \frac{\gamma_\uparrow}{\gamma_\uparrow + \gamma_\downarrow}, \tag{5.2.14}$$

In Fig. 5.2 we show the derived (de-) excitation rates versus the blue laser detuning Δ_2 for a variety of laser parameters. In the left and middle column only a single of the three remaining controllable parameters is varied and the others are kept constant at $\Omega_1 = 2\pi \times 6$ MHz, $\Delta_1 = 0$ MHz and $\Omega_2 = 2\pi \times 0.4$ MHz. In the right most column the corresponding steady state populations are shown. We observe that the excitation rates show the general features we expect, like Autler-Townes splitting into two Lorentzian peaks for $\Omega_1 > \Gamma_e$ and tend to 0 for large Rydberg detuning Δ_2. For small Ω_1, the two Lorentzian peaks merge, as expected. For large intermediate state detuning Δ_1, the center of the largest peak shifts towards larger Rydberg detuning by a value of $\Delta_1/2$ and the peak to peak distance is $\sqrt{\Omega_1^2 + \Omega_2^2 + \Delta_1^2}$. Further, the ratio between the maximal height of the two peaks tends to zero. These features are easily explained from the eigenvalues and -states of the Hamiltonian (5.2.1). For the deexcitation rates we generally observe the same with two important addenda. First, for large Rydberg detuning Δ_2, the de-excitation rate does not go to zero, but rather Γ_r, as expected. Secondly, for small Rydberg detuning, the de-exitation also approaches the spontaneous decay rate Γ_r. This happens as the de-excitation rate only has an effect on the Rydberg state, which for zero detuning has an overlap with a dark state of the Hamiltonian (5.2.1) larger than 0.99, meaning that the lasers have no influence on the de-excitation rate in this case, reducing the de-excitation rate to the spontaneous decay rate.

The Rydberg populations, as shown in the rightmost column of Fig. 5.2, are found using eq. (5.2.14). Increasing the red Rabi frequency Ω_1 beyond the intermediate state spontaneous decay rate Γ_e broadens and lowers the Rydberg transition resonance, as Autler-Townes splitting affects the excitation rate. Increasing the intermediate state detuning, lowers and narrows the Rydberg transition resonance, but only slightly, as well as giving a slight shift to the resonance.

5.3 Rate equation validity

Going back to eq. (5.2.6) and considering the adiabatic elimination of the co-herences, we know that $\mathcal{R}$, has nine complex eigenvalues $v_1, \ldots, v_9$ and the
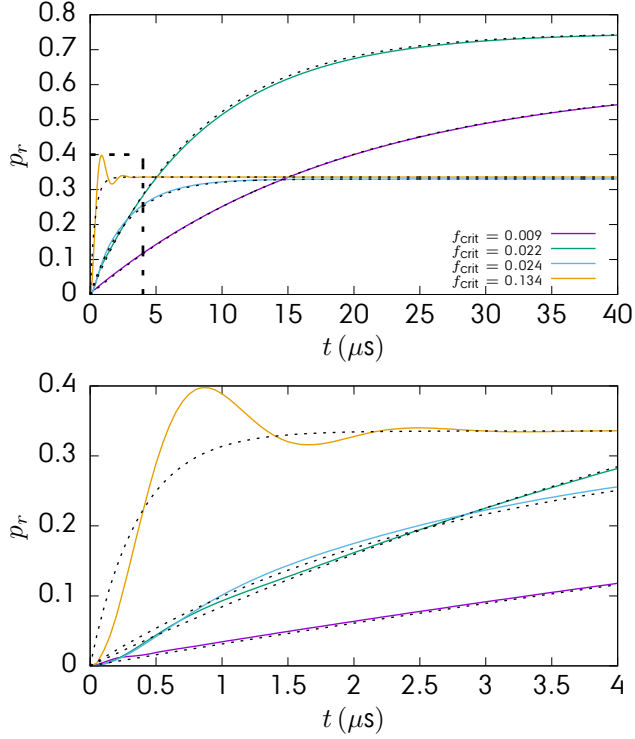
Figure 5.3: *Numerical solutions to the optical Bloch equation (solid) and rate equation approximations (dotted) versus time for different critical fractions f_{rm}. Bottom plot shows a magnification indicated by the dashed square. Lines with small critical fraction show good agreement between rate equations and optical Bloch equations, whereas the large critical fraction line only shows good agreement with final population value.*

coherence only part $\mathcal{R}_c$ six complex eigenvalues $k_1, \ldots, k_6$, which determine the time scale of the dampening of the coherences. This time scale has to be short, in order to support adiabatic elimination of the coherences. Of the eigenvalues $v_1, \ldots, v_9$, only three have eigenvectors with non-zero populations of the intermediate state, and of these only one is always real valued, we call this v_1. In addition one eigenvalue, which we call v_9, is always zero.

We define the dampening time scales for eigenvalue v as $\tau_v = \frac{-1}{\Re(v)}$, and make shorthands for the three most important

$$\tau_0 = \tau_{v_1} \tag{5.3.1}$$

$$\tau_1 = \max(\tau_{v_2}, \ldots, \tau_{v_8}) \tag{5.3.2}$$

$$\tau_2 = \max(\tau_{k_1}, \ldots, \tau_{k_6}). \tag{5.3.3}$$

Since τ_0 is, in general, larger than τ_1, it is the time scale on which higher order dynamics of the system dampens out and only the steady state solution remains. On top of this the coherences dampen out on the time scale τ_2.
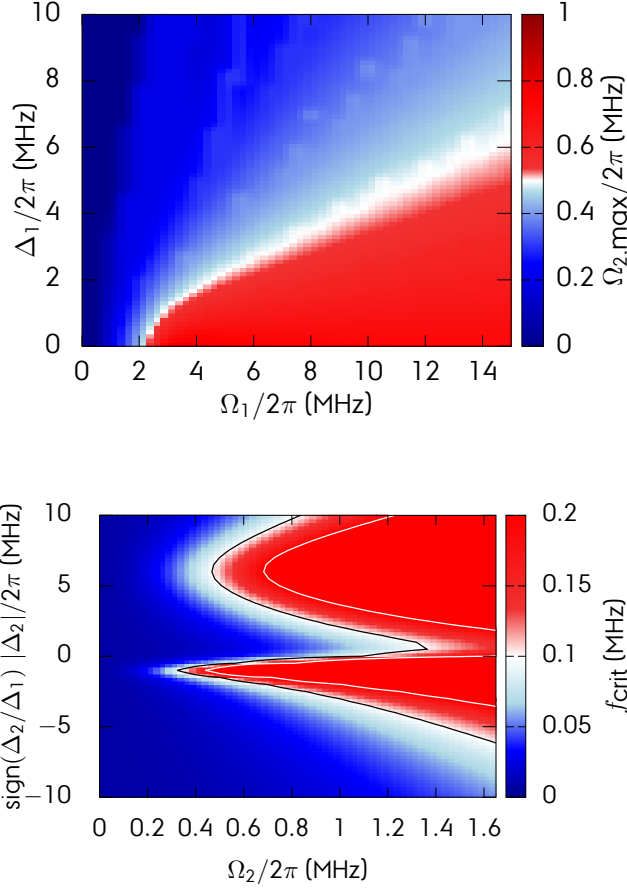
Figure 5.4: *Top: Maximal allowed blue Rabi frequency Ω_2 versus red Rabi frequency Ω_1 and red detuning Δ_1. This value is found as the largest blue Rabi frequency for which the critical fraction is smaller than 0.1 for all (positive) blue detunings Δ_2. Bottom: Critical fraction f_{crit} in the Ω_2-Δ_2 plane for $\Omega_1 = 2\pi \times 5$ MHz and $\Delta_1 = 2\pi \times 5$ MHz. Black contour line is at $f_{crit} = 0.1$ and white at $f_{crit} = 0.2$. We generally require that $f_{crit} < 0.1$. Note that the positive detunings allow for larger Ω_2, but since the sign is dependent on the ratio between the detunings, we can always choose positive for a given experiment.*

The rate equation model is dependent on there being a clear distinction between the dynamics on the long time scale τ_0 and the shorter time scales τ_1 and τ_2, and This means that we now have conditions for the validity of the rate equation model

$$\tau_0 >> \max(\tau_1, \tau_2) \tag{5.3.4}$$

$$t >> \tau_1, \tag{5.3.5}$$

where t is the simulation run time. For practical purposes, we will assume this to be satisfied if

$$f_{\text{crit}} = \frac{\max(\tau_1, \tau_2)}{\tau_0} < 0.1, \tag{5.3.6}$$

which we call the critical fraction. Fig. 5.3 shows a comparison between our rate equation model (dotted) and the optical Bloch equations (solid) for different critical fraction values. The agreement between solid and dotted lines is clearly dependent on the critical fraction. Of special note is the rather bad agreement between the solid and dotted lines for critical fraction larger than 0.1, which we choose as the practical limit.

We have searched the parameter space to satisfy these conditions, and the requirements are in general quite lax for reasonable red laser parameters, see Fig. 5.4. For any given combination of red Rabi frequency and detuning, we find the critical fraction in the Ω_2-Δ_2 plane, and determine the maximal allowed blue Rabi frequency $\Omega_{2,\max}$ as the largest value of Ω_2 for which the critical fraction is smaller than 0.1 for all (positive) blue detunings Δ_2.

The maximal blue Rabi frequency is dependent on the relative sign of blue detuning to red detuning, and we can find blue Rabi frequency limits Ω_b^+ and Ω_b^-, dependent on that sign, below which the rate equations always hold. This asymmetry is stemming from the asymmetry in the excitation due to the red laser. Since $\Omega_b^+ \geq \Omega_b^-$ is always the case, we can choose the sign of the red detuning such that we have the largest allowed range for Ω_b. However, if scanning the blue detuning across the resonance, the blue Rabi frequency has to be below Ω_b^-, as the limiting point is right below zero. It is worth noting though that for most detunings, the maximal blue Rabi frequency can be much larger than this limiting value, and it would be prudent for any experiment to determine the limiting values appropriate for the specific experiment.

5.4 Monte Carlo simulation

We have implemented our (de-)excitation rates in a kinetic Monte Carlo simulation, where we extract the values of interest as the average over many realizations. We will explore three different settings, first we consider a 1D regular lattice, secondly a random gas with a square quasi 2D excitation volume and finally we will compare to experimental measurements.

Each Monte Carlo realization is performed by, at time $t_0 = 0$, calculating (de-)excitation rates for all atoms and an exponentially distributed random time step dt, with mean value $1/\sum_i \gamma_{\updownarrow}^i$, with $\gamma_{\updownarrow}^i$ the excitation rate for atom i (deexcitation rate if atom i is already excited). We then randomly pick an atom with probability
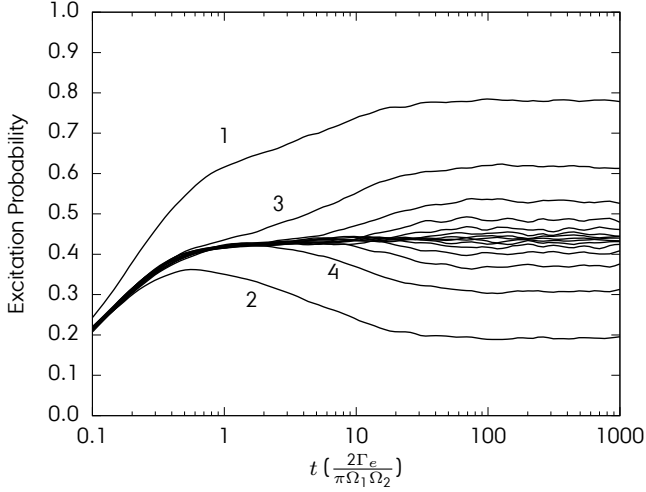
Figure 5.5: *Time dependence of excitation probability in the 1D lattice with 30 lattice sites. Labels denote lattice site. Probability is calculated as the number Monte Carlo realizations with a Rydberg excitation at a site divided by the total number of realizations for every time step.*
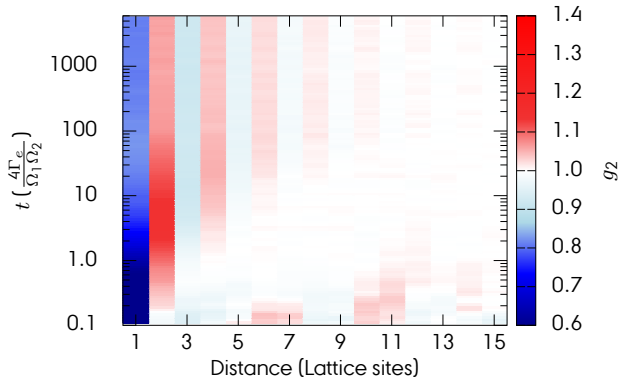

Figure 5.6: *Time dependence of the g_2 function for a 1D lattice with 30 lattice sites. Nearest neighbors are never Rydberg pairs, but for times larger the equilibration time $T = 4\Gamma_e/\Omega_1\Omega_2$ Rydberg excitations start to come in pairs separated by one atom and at $10T$ the crystal consists of 3 excitations. The correlation length scales as $t^{1/3}$, but saturates at $t \sim 100T$.*

proportional to the $\gamma_\uparrow^i$. This atom is then (de-)excited and the time is set to $t_1 = t_0 + dt$. This procedure is then repeated until the time exceeds the simulation time $t_{\text{end}} < t_{\text{end}-1} + dt$. At prespecified times, we save the state of the system for our analysis. The output of the Monte Carlo simulation is the average over all realizations.

For our 1D lattice simulation, the individual lattice sites are identifiable and we therefore explore the time evolution of the excitation probability of the individual sites. This requires many realizations to converge and we therefore perform 6000 realizations for the simulation.

We consider a string of 30 atoms placed at regular distance $l = 16.3\,\mu$m with laser parameters $\Omega_1 = \Gamma_e/2$, $\Omega_2 = \Gamma_e/10$, $\Delta_1 = \Delta_2 = 0$. This results in a nearest neighbor interaction strength $V_{nn} = 2\Omega_1$ for the $100S$ state and corresponds to the work done in [Hï3]. Our work is consistent with their result, but for a slightly larger correlation length due to the fully interacting system.

On time scales on the order of the steady-state equilibration time for a single atom T, the system reaches a $1 - e^{-1}$ fraction of its final Rydberg population, but this is distributed over many single atom excitations. At such small time scales, only the edge atoms have a larger than average Rydberg probability, as they only have neighbors on one side, see Fig. 5.5. On time scales of $3T$, we observe the first formation of small local crystalline structures with correlation lengths larger than 1 lattice constant and growing as $t^{1/3}$, see Fig. 5.6, consisting of two Rydberg excitations separated by a single unexcited lattice site. These structures are not all consistent with a global crystal, as they have formed at random positions in the lattice and could lead to domains in the final state. At this time, the enhanced Rydberg probability of the edge sites leads to suppression of the Rydberg probability of their neighbors. This effect is the beginning of the global crystal structure.

These small crystals will continuously form and melt in the lattice at random positions, but as time passes, fewer and fewer sites not consistent with a larger crystal will be available, and at time scales of $10T$ the average crystal formation will contain three Rydberg atoms. As the process continues, the crystal forming on the edge grows, as there is no room for excitation hopping, and the average crystal size increases. At large time scales ($\sim 100T$), a global crystal has formed by spanning the entire lattice, and the correlation length does not increase further.

We move on to our quasi 2D random gas, which we will use to model the conditions in a magneto optical trap (MOT), and consider three statistical properties: Average Rydberg count $\langle N_{\text{Ryd}} \rangle$, Mandel Q-parameter and second order spatial correlation g_2. We perform each Monte Carlo realization with a total simulation time $t_{\text{end}} = 250\,\mu$s, a total number of atoms N_{tot} equal to the integral of the atomic density in the laser volume. The total number of realizations is 2500 for every set of parameters. Additionally, we assume the gas to be cold enough that we can ignore all atomic motion.

We excite to the $99S$ state and use laser parameters according to our experimental setup: $\Omega_1 = 2\pi \times 4\,$MHz, $\Omega_2 = 2\pi \times 0.5\,$MHz, $\Delta_1 = -2\pi \times 9\,$MHz and the blue laser detuning Δ_2 is variable. The red laser intersects a Gaussian blue sheet with waist $\sigma_{\text{blue}} = 7\,\mu$m. Due to the thickness of the blue sheet, we do not expect the second order correlation function g_2 to be zero inside the blockade radius,
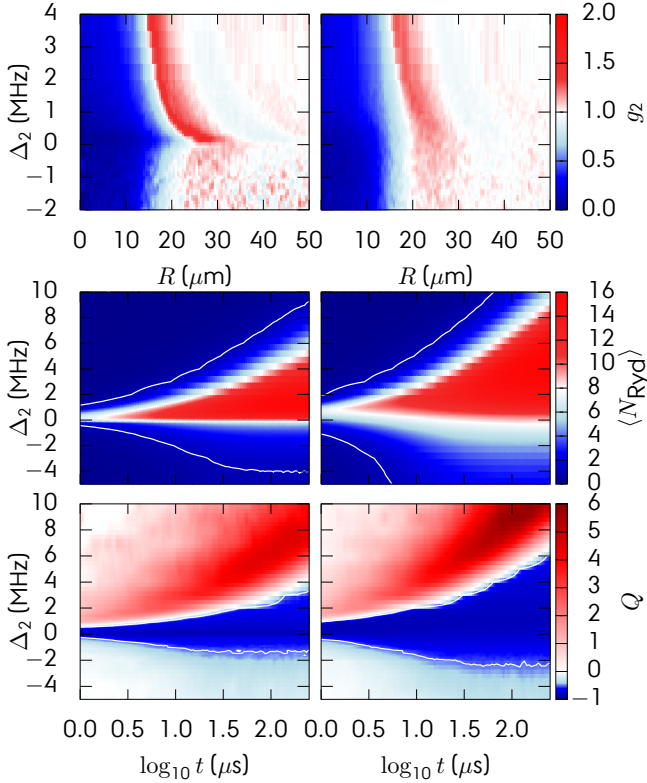
Figure 5.7: *Statistical measures of Rydberg excitation for a Gaussian profile red laser beam (left) and a uniform square laser beam (right). Both simulations have $\Omega_1 = 2\pi \times 4$ MHz, $\Omega_2 = 2\pi \times 0.5$ MHz and $\Delta_1 = -2\pi \times 9$ MHz and the red laser intersects a Gaussian blue sheet with waist $\sigma_{blue} = 7\ \mu m$. On the left hand side the simulation is carried out with a Gaussian profile red laser with waist $\sigma_{red} = 25\ \mu m$ and the right hand side a square box with side length $l = \sqrt{2\pi}\ 25\ \mu m$, this ensures that the total power of the two lasers is the same. Top: g_2 map. In both cases we observe clear blockade for small distances R followed by a uniform distribution for negative blue detuning ($\Delta_2 < 0$) and strong facilitation for positive blue detuning. Middle: Average Rydberg count across all realizations. White contours mark $\langle N_{Ryd} \rangle = 1$. Large Rydberg populations do not appear for large negative detuning and appear explosively but delayed for positive detunings. Note that the square geometry has about half the number of atoms in the excitation volume and hence twice the Rydberg fraction. Bottom: Mandel Q-parameter. Dark blue is $Q < -1/2$, the deeply subpoissonian regime. For positive detuning $Q > 0$, we are in the superpoissonian regime (red).*

but strongly suppressed, since we only explore the correlations in the projection on the blue laser plane. In Fig. 5.7, we show results from two different red laser geometries, realizable in our experiment by means of a spatial light modulator,
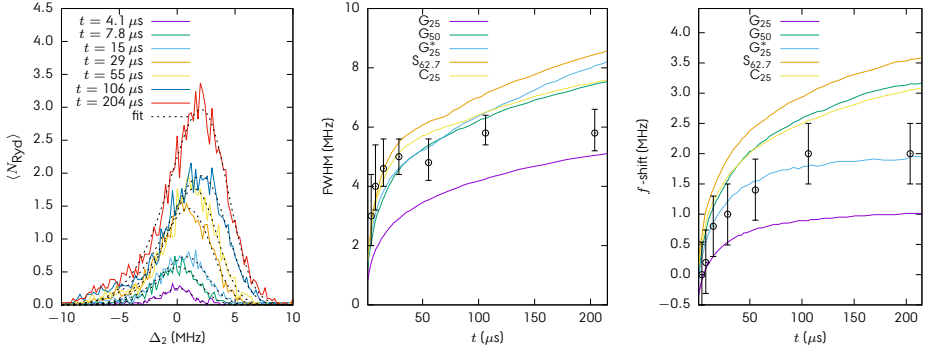
Figure 5.8: *Left: Rydberg spectra in experiment (solid) with laser parameters $\Omega_1 = 2\pi \times 4$ MHz, $\Omega_2 = 2\pi \times 0.5$ MHz and $\Delta_1 = -2\pi \times 9$ MHz and the red Gaussian profiled laser, with waist $\sigma_{red} = 25\,\mu m$, intersects a Gaussian profile blue sheet with waist $\sigma_{blue} = 7\,\mu m$, corresponding to the simulations in Fig. 5.7. Dashed curves are skew-Gaussian fits. Middle: Full width half max of the experimental spectrum (circles), errorbars determined from fit, and simulation (solid) of Gaussian (G), square (S) or circular (C) laser beam profiles with the characteristic length scale (std for Gaussian, side length for square and radius for circular) denoted by subscript. The star (*) denotes simulation with twice the red laser intensity ($\Omega_1 \rightarrow \sqrt{2}\Omega_1$). Right: Frequency shift of the experimental spectrum (circles), errorbars determined from fit and frequency drift of the blue laser. Solid curves represent the same simulations as in the middle plot. The overall comparison between experiment and simulation show general agreement for both FWHM and frequency shift.*

a Gaussian beam profile with waist $\sigma_{red} = 25\,\mu m$ (left in Fig. 5.7) and a square beam profile of uniform intensity with side length $l = \sqrt{2\pi}\,25\,\mu m$ (right in Fig. 5.7). These shapes ensure the two lasers output the same power, but the Gaussian excitation volume has about twice the number of atoms compared to the square geometry. Our model is not limited to these laser shapes and parameters, but they show the essential features. Since the blockade radius R_{block}, for the given parameter and $\Delta_2 = 0$, is $20.9\,\mu m$, we expect the system to be completely filled at $N_{Ryd} = (l/R_{block})^2 \approx 9$ for the square beam profile and slightly before that for the Gaussian beam profile, we call this number the jamming count N_{Jam}.

We start by generating N_{tot} random 3D coordinates in the laser volume, and we calculate the laser parameters at each coordinate as well as the distances between all pairs of atoms. With these parameters in place at the beginning of each realization it is easy to evaluate the (de-)excitation rates at each atom on the fly.

For any specific realization we are only interested in the Rydberg count and distribution at a number of prespecified time steps, therefore we only carry the binary information of Rydberg state or ground state for each atom, as well as the atom positions. This will let us determine both the Rydberg-Rydberg interaction strength at each coordinate from the predetermined atomic distances, for use in determining the rates, and is sufficient to calculate the aforementioned statistical

measures we are interested in for the total ensemble of realizations, see Fig. 5.7.

Analysis of the Monte Carlo simulations shows features usually associated with the Rydberg-Rydberg interaction, but also illustrates a clear dependence on excitation geometry. The location of the first excitation is much more likely to occur near the center of the excitation volume for the Gaussian profile beam. For negative detunings this leads to even stronger blockade as not only is the effective detuning larger, but the Rabi frequency is also lower. For positive detunings, however, the facilitation rings become narrower. The gradient of the laser intensity also leads to a tighter distribution of excitations, as excitation too far from the center is unlikely, limiting the number of excitations in the volume.

From the Mandel Q-parameter, see Fig. 5.7 (bottom), we can identify three regimes of interest: Firstly, the (weakly sub)poissonian (light blue) regime where $-1/2 < Q < 0$, found for very low blue laser detunings Δ_2. Secondly, the deeply subpoissonian (dark blue) regime where $Q < -1/2$, found for small absolute values of Δ_2. And thirdly, the superpoissonian (red) regime where $Q > 0$, found for large positive Δ_2.

For negative blue laser detunings, the Mandel Q-parameter gradually decreases over time from 0 to its final value. This happens as atoms are excited to the Rydberg state and exclude parts of the volume. For very negative detunings, only a few Rydberg excitations exist at any given time and the Q-parameter stays relatively high, since the jamming limit is never reached. This is again reflected in the average Rydberg count, which is very low compared to the jamming count N_{Jam}.

For detunings nearer to zero, the number of Rydberg excitations increases over time and the jamming limit is reached, resulting in deeply subpoissonian counting statistics. The subpoissonian regime is reached somewhat before the jamming count, since the reduction in the excitation volume is significant when $N_{\text{Ryd}} \geq \sqrt{N_{\text{Jam}}}$.

For positive blue laser detunings, an initial Rydberg excitation, called the seeding excitation, results in a ring of resonant excitation around the seed at the distance $R = (C_6/\Delta_2)^{1/6}$, called the facilitation distance R_{fac}. The seeding excitation occurs with low probability for large detunings, but after seeding more Rydberg atoms are quickly excited on resonance. This results in superpoissonian counting statistics, as a cascade of Rydberg excitations spreads from the seed. We see this in the steep slope of the average Rydberg count for positive detuning coinciding with very large Mandel Q-parameter. However, the system quickly fills up, reaching the jamming limit resulting in a drop to negative Q and the strongly subpoissonian regime.

The second order correlation functions g_2 at time $t = 250\,\mu\text{s}$ for the Gaussian (left) and square (right) beam profiles are seen in Fig. 5.7 (top). For negative blue laser detuning, the region in the immediate vicinity of a Rydberg excitation ($R \lesssim R_{\text{block}} = 21\,\mu\text{m}$) shows very reduced values of g_2. Around R_{block}, the g_2 gradually climbs to 1, with only a slight overshoot. This behavior is the same for both geometries and consistent with the blockade effect. The nonzero value for short distances is due to the thickness of the excitation volume, as we only consider the correlations in the plane parallel to the blue laser sheet.

For positive blue laser detuning the blockade effect is still clearly visible for small distances, but at the facilitation distance $R_{\text{fac}} \approx (C_6/\hbar\Delta_2)^{1/6}$ there is a strong

signal from the facilitation region followed by a dip from the blockade effect of the facilitated excitations. This feature is significantly sharper for the Gaussian geometry consistent with a narrower facilitation region due to the drop off in laser intensity. At about $2R_{\text{fac}}$, a faint signal from the secondary facilitation peak is visible for both the Gaussian and the square beam profiles.

At very limited blue laser detunings ($|\Delta_2| \lesssim 0.5$ MHz) the g_2-function resulting from the Gaussian beam profile shows a cusp that is not present in case of a square beam profile. This cusp is in part due to the sharpening of the facilitation peak in the Gaussian profile case and in part due to the tighter packing of Rydberg excitations for the Gaussian beam profile. This leads to a crystalline locking of the Rydberg excitations in the relatively small volume of peak laser intensity.

5.5 Experimental validation

Rydberg excitation was studied experimentally using a setup described previously [Eng14, Bij14]. In short, ^{85}Rb atoms are trapped and cooled in a standard magneto-optical trap, resulting in typical atomic densities of $10^{16}/\text{m}^3$ and temperatures of 0.2 mK. To create Rydberg atoms from the cooled sample, the 780nm trapping laser beams are suddenly switched off, after which a separate 780 nm and a 479 nm laser beam are flashed on for a variable amount of time, which drive the $5S, F = 2 \rightarrow 5P_{3/2}, F = 3$ and $5P_{3/2}, F = 3 \rightarrow 99S$ transitions in ^{85}Rb. The red laser beam is referenced to the atomic transition frequency by a saturated absorption scheme, and detuned approximately 9 MHz below resonance. The frequency of the blue laser can be scanned in a range of tens of MHz centered on the two-photon resonance condition and is referenced to a commercial ultra-stable cavity (Stable Laser Systems). The linewidths of the two laser beams are below 1 MHz but otherwise not accurately known.

The red laser beam can be spatially shaped using a spatial light modulator [Bij14] in various ways but in the experiments reported here the spatial shape was a single Gaussian with a rms radius of 25 μm. This shaped red beam crosses the blue beam at the center of the MOT, where the rms sizes of the blue beam are 7 μm $\times$1.8 mm. Typical excitation times are in the μs range. The powers of the laser beams were adjusted to provide nominal Rabi frequencies of $\Omega_1 \approx 4$ MHz and $\Omega_2 \approx 0.5$ MHz.

Rydberg atoms created by this excitation sequence were detected using field ionization. An electric field of several kV/m strength is turned on which ionizes any Rydberg atoms present and pushes the resulting ions towards a dual microchannel-plate detector (GIDS GmbH) [Eng14]. The current produced by the detector is fed through a transimpedance amplifier and then sampled by a digital oscilloscope (Agilent DSO 054A). The integral of the digitized signal over a period of the experimental cycle is taken as proportional to the number of Rydberg atoms produced.

Experimentally observed spectra are shown in Fig. 5.8 (left), and fitted with a skew Gaussian. From this fit the derived parameters of full width half max (FWHM) (middle) and frequency shift (f-shift) (right) are determined and plotted (circles). The errorbars on the FWHM values are determined from the 95% confidence limit of the fitting parameters (fitting error). The f-shift errorbars are determined as the

root of the sum of the fitting error squared and the measurement error squared. The derived parameters from the experiment are compared to simulation (solid). We show here derived parameters for both the Gaussian and the square laser profile simulations of Fig. 5.7 as well as those from a simulation with the same Gaussian laser profile, but twice the intensity, *ie.* $\Omega_1 \to \sqrt{2}\Omega_1$.

Direct comparison between the experimental (see Fig. 5.8, left) and simulated (Fig. 5.7, middle) spectra shows a general agreement. Far from resonance ($|\Delta_2| \gtrsim$ 8 MHz) the experimental Rydberg count is suppressed at all times. For negative Rydberg detuning ($\Delta_2 \lesssim -2$ MHz) we see suppression of the increase in Rydberg count over time, consistent with the existing Rydberg atoms in the volume blocking excitation of additional Rydberg atoms. Nearing zero detuning ($|\Delta_2| \lesssim 2$ MHz) the Rydberg count grows fast and the peak shifts towards higher detunings with time. This means that, especially at later times, the peak is shifted to large Rydberg detuning ($\Delta_2 \gtrsim 2$ MHz). At these large detunings, we observe almost no Rydberg atoms at small times, but with increasing time this changes as facilitation shifts the Rydberg levels of unexcited atoms into resonance. This is all in agreement with the simulation results presented in Fig. 5.7.

For both experimental data and simulation we observe that both the FWHM and f-shift, derived from the spectra in Fig. 5.8, values rise quickly and then level out after about 50 μs. The precise shape of the excitation volume and laser profile have little influence on the behavior of the FWHM value, and we can generally explain experimental observations without knowledge of the exact excitation volume geometry. Similarly, the f-shift shows some dependence on the laser profile, but this can be explained from the small dependence of Rydberg count on geometry to influence the f-shift.

5.6 Conclusions

We have derived rate equations for excitations of the Rydberg state in three-level atoms starting from the master equation. Our approach does not assume vanishing populations in the intermediate state and are therefore valid for a wide range of laser parameters, in principle whenever the three-level approximation of the atom is valid.

Our rate equation model agrees with the master equation, provided that only one eigenvalue has not dampened out. We have investigated and described the validity range of our approach, and determined criteria that provide sufficient insight into whether our model is valid or a full solution of the master equation is required.

We have made a Monte Carlo implementation of our (de-)excitation rates, and explored different excitation geometries and laser parameters. In this paper we have reported on 1D lattice simulations, with parameters corresponding to previous theoretical work published in [Hï3], and found our results to be consistent with literature. We explored the dynamics of self assembly of the resulting 1D Rydberg crystal, and the time evolution of the second order correlation function g_2 and site dependent excitation probability.

We further explored 2D settings, where we considered the effect of the laser beam profile by comparing a Gaussian profile to a square of uniform intensity

with sharp edges. We found that the beam profile has significant influence on the resulting excitation pattern and that a Gaussian profile in general will result in sharper features in the g_2-map, but at the cost of lower excitation counts.

We have compared our model to experimentally observed Rydberg spectra at several time steps and found a general agreement for the spectral shapes and derived parameters FWHM and f-shift. We did not see any significant dependence on excitation volume geometry in the time dependence of FWHM, but the geometry dependence of the Rydberg count may result in a slight geometry dependence of the f-shift.

Acknowledgments

Controlled Quantum Plasmas Created from Rydberg Crystals

R. V. Skannrup, E. J. D. Vredenbregt and S. J. J. M. F. Kokkelmans

Abstract

Rydberg atoms, made by exciting (alkali) atoms to high principal quantum number n, interact very strongly via dipole interactions or long range van der Waals interactions and have been proposed for quantum simulation. We investigate how such a system can be used to simulate one dimensional chemistry and insulator-conductor crossovers and as a source for degenerate electrons. Starting from a one dimensional Rydberg crystal, the electrons will, if excited highly enough, have enough kinetic energy to pass through the potential barrier between the atoms, and the system can transition into an ordered conductor. We study a 1D model, where we find crossovers between insulators and conductors and bound states of 1D molecules, as well as universal scaling of the lengths and energies, dependent on principal quantum number n.

6.1   Introduction

Characterized by having large principal quantum number n, highly excited Rydberg atoms are on the front of research today [Saf10a, Sha18, Saf16b, Lim13, Bro16, Hel16]. Extreme properties, such as van der Waals coefficient scaling as n^{11} and blockade [Rob05] or facilitation [Wei08b] of nearby excitations at distances of micrometers make Rydberg atoms not only interesting but also a valuable tool in the atomic toolbox. Magnetically trapped ground state atoms can be excited to trapped Rydberg atoms with identical trapping conditions for ground and Rydberg state [Boe18]. Strong interactions, combined with long life times, versatile trapping conditions and single site addressability [Boe18] make Rydberg atoms an ideal platform for quantum simulation [Wei10, Saf10a].

Due to the strong van der Waals interactions between the Rydberg atoms, the gas can crystallize [Bij11, Poh10], or be excited in a regular pattern[Bij15]. The regularity of such a Rydberg lattice limits disorder induced heating, which in turn limits the velocity of the ionic cores, allowing for a frozen gas treatment of the system. Thus Rydberg atoms allow precise control over interparticle distance, spins and principal quantum number, making the system ideal for studying quantum systems with carefully designed geometries that are not readily found in nature.

In a highly excited Rydberg gas the atoms are known to spontaneously ionize [SV13, Poh03]. The first electrons are lost, but eventually the positive charge from the ionic cores becomes so strong that additional ionized electrons are bound to the ion structure. This leaves a system, where the number of valence electrons is smaller than the number of cores. Such a system is known as an ultracold plasma, since the cores can be assumed motionless at the short time scales, where such systems exist. When the spacing between the cores becomes comparable to the electron de Broglie wavelength, we have to consider the quantum nature of the plasma [Bon10]. This gives structure to the spatial electron distribution and we have to consider the degeneracy of the electronic states. This is a quantum plasma, other examples of quantum plasmas are valence electrons in metals, ionized matter in the interior of very heavy stellar objects and the quark-gluon plasma in the early universe. Investigating quantum plasmas is therefore of interest to both fundamental and applied physics. For atoms with high principal quantum number, the electron wavefunction has a larger extent and we can enter the quantum plasma regime in more dilute gases. The principal quantum number therefore acts as a control parameter to go from Rydberg crystal to a quantum plasma.

We solve the electronic system, sketched in Fig. 6.1, using tools from few-body physics, as a simple model for Rydberg crystal excitations into the quantum plasma regime. We have focused on and compared the results from Stochastic Variation (SV) [Suz03] and Numerical Integration of the 1D Schrödinger equation (NI). We have had a special focus on investigating the feasibility of simulation quantum plasmas and the scalability of the simulated systems using these methods. We neglect (hyper) fine structure or spin-orbit coupling.

Exotic materials such as carbon nanotubes [Cha07, Egg98, Boc99, Ped03], organic conductors [Sch98, Zwi00, Lor02], quantum Hall edge states [Cha03], and semiconductor quantum wires [B87], as well as transition metal oxides [Hu,02], confined atomic gases [Mon98, Rec03, Mor05] and certain polymers [Bar13] can
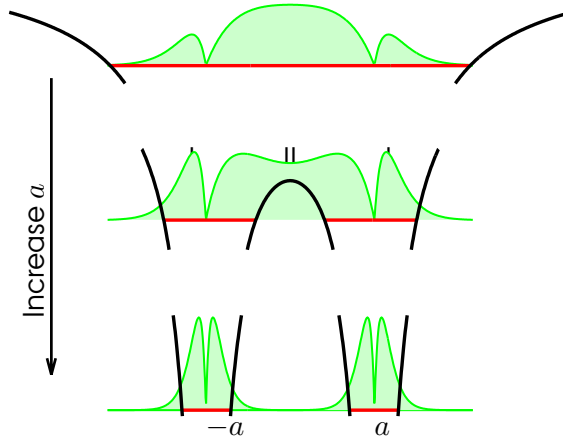
Figure 6.1: *Model potential (black) with idealized typical wavefunctions (green). The wavefunctions all represent the ground state at different distances between the ionic cores a. Top: The wavefunction can be seen as a part outside the core structure and a part between the cores. The wavefunction approaches zero at the cores, this puts strong constraints on the state and has a significant influence on the energies, as we will show. Middle: Central barrier starts to suppress the state between the cores. Bottom: There are no electronic states shared between the atoms. Features in the wavefunction at small a and low E reappear at large a and high E, which are captured by scaling relations dependent on principal quantum number n.*

greatly restrict the movement of electrons towards a quasi 1D nature. In hydrogen-like atoms in magnetic fields with field strengths $B \gtrsim 10^6$T [Lou16, Has61, Wun81], this is also the case, but we will show that the field strength needed, when dealing with Rydberg atoms, is much weaker.

In recent years the 1D Coulomb system has been theoretically studied by several authors [Lou16, Loo15, Bal17]. Loudon [Lou16] focuses on the hydrogen atom, and treats the subjects of regularization and experimental realization extensively. Ball, Loos and Gill [Loo15, Bal17] treat the subject of 1D chemistry with no regularization and describe the lowest chemical states of several systems.

This paper contains four sections in addition to this introduction. In section 6.2 we will present a way to reduce Coulomb systems to quasi 1D based on the approach of [Lou16], as well as a regularization of the Coulomb potential to avoid some of the unnatural behavior discussed in literature. In section 6.3 we discuss the consequences of the regularization and present results of 1D systems with a single electron in the potential from two to five ionic cores as well as a periodic lattice. We find approximations for the energies at small and large distance between the cores and find scaling relations for the system. In section 6.4 we present results of a system with two electrons and two ionic cores. Again we will present approximate expressions for energies of the system at small and large distance between the

cores and discuss some of the unique features of the system. In section 6.5 we conclude on our work and discuss the future perspectives of this work.

6.2 Quantum Plasma Model

We develop a 1D toy model for quantum plasmas, and make the case for the 1D model by initially considering a hydrogen atom in a uniform magnetic field of strength B pointing in the z direction. We write the vector potential in cylindrical coordinates as $\boldsymbol{A} = (0, \frac{1}{2}B\rho, 0)^T$, where ρ is the radial distance. Using minimal coupling we find the cylindrical coordinate Hamiltonian in atomic units, which we will use throughout this paper,

$$
\begin{aligned}
H_{\text{cyl}} =& \frac{1}{2} \left(i\nabla - \boldsymbol{A} \right)^2 - \frac{1}{\sqrt{\rho^2 + z^2}} + \hat{\boldsymbol{s}} \cdot \boldsymbol{B} \\
=& \frac{-1}{2} \left(\frac{\partial^2}{\partial z^2} + \frac{1}{\rho} \frac{\partial^\rho}{\partial\rho^\rho} \frac{\partial^\rho}{\partial+^\rho} \frac{1}{\rho^2} \frac{\partial^2}{\partial\phi^2} \right) \\
&+ \frac{1}{2} \frac{B^2}{4} \rho^2 - \frac{i}{2} B\rho \frac{\partial^\phi}{\partial-^\phi} \frac{1}{\sqrt{\rho^2 + z^2}} + s_z B,
\end{aligned}
\tag{6.2.1}
$$

where ϕ is the angle around the z-axis and $\hat{s}$ is the electron spin operator. Assuming a wave function of the form

$$
\psi = R(\rho, z)e^{il\phi},
\tag{6.2.2}
$$

we can rewrite eq. (6.2.3) as

$$
\begin{aligned}
H_{\text{cyl}} =& \frac{-1}{2} \left(\frac{\partial^2}{\partial z^2} + \frac{1}{\rho} \frac{\partial^\rho}{\partial\rho^\rho} \frac{\partial^\rho}{\partial-^\rho} \frac{l^2}{\rho^2} \right) \\
&+ \frac{1}{2} \frac{B^2}{4} \rho^2 - \frac{1}{2} Bl - \frac{1}{\sqrt{\rho^2 + z^2}} + \hat{s}_z B.
\end{aligned}
\tag{6.2.3}
$$

This Hamiltonian has a harmonic oscillator part in the radial direction, which becomes dominant over the Coulomb potential at large ρ. This happens at $\rho \sim 2B^{-2/3}$, which decreases with the magnitude of the magnetic field. If this distance is well inside the classical orbital radius of the electron, expressed in terms of the Bohr radius as $a_0 >> 2B^{-2/3}$, the Coulomb potential merely acts as a perturbation to the harmonic oscillator potential. The magnetic field needed to confine the ground state of hydrogen to a quasi 1D geometry is then (in SI units)

$$
B_1 >> \sqrt{\frac{2m}{\pi\epsilon_0 a_0^3}} \approx 660 \, \text{kT}.
\tag{6.2.4}
$$

However, our quantum plasma model is derived from an ultracold crystal of highly excited Rydberg atoms, which can be created and studied at timescales short enough to satisfy the frozen gas approximation where it is assumed that there is not enough time for the atomic cores to move significantly. Since the classical orbital radius of an electron in a hydrogen atom scales as the principal quantum

number n squared, the magnetic field dominates the electronic motion if the magnetic field has a strength above

$$B_n \approx \frac{B_1}{n^3}. \tag{6.2.5}$$

Therefore, to confine the electron in a highly excited Rydberg atom, well within current experimental capabilities [Ska20], where $n \sim 100$ to a quasi 1D geometry, we only need magnetic fields in the 10 Tesla range. Though still very strong magnetic fields, this is significantly lower than the aforementioned 600 kT needed for ground state atoms.

Since Rydberg atoms can be excited in specified patterns using a Spatial Light Modulator (SLM) to project the pattern into a cold atomic cloud [Bij15], or by exciting magnetically trapped atoms [Boe18], we propose using crystals of Rydberg atoms, which are very sensitive to external fields to explore the electron behavior in a quasi 1D geometry.

Assuming the magnetic field to be dominant, we can use separation of variables and first order perturbation theory to estimate the energy of the radial system from the harmonic ground state dependent on z

$$
\begin{aligned}
E_{\text{rad}} &= \frac{B}{2} - B \int_0^\infty \frac{e^{-\frac{B}{2}\rho^2}}{\sqrt{\rho^2 + z^2}} \rho \, d\rho \\
&= \frac{B}{2} - \begin{cases} \sqrt{\frac{B\pi}{2}} & \text{for } z^2 << \frac{1}{B} \\ \frac{1}{\sqrt{z^2}} & \text{for } z^2 >> \frac{1}{B}, \end{cases}
\end{aligned} \tag{6.2.6}
$$

which allows us to separate the Schrödinger equation into a radial, an angular and a longitudinal part and assume wavefunctions of the form

$$\psi = K_n(z) L_h^l(\rho) e^{il\phi}, \tag{6.2.7}$$

where n, h and l are appropriate quantum numbers. The extent of the radial wavefunction L_h^l is limited to a few oscillator lengths $\sqrt{B^{-1}}$, and we are not interested in the dynamics close to the nuclei, as this is well understood [Boe18], and we will assume the electrons to be in the radial ground state. However, our large z solutions have to be able to circumvent the nuclei, which means removing the singularities at the nuclei. Therefore we introduce a regularization of the 1D Coulomb potential, which smoothly cuts off the potential on length scales comparable to the extent of the radial wavefunction

$$\frac{1}{\sqrt{z^2}} \to \frac{1}{\sqrt{z^2 + \epsilon^2}}, \tag{6.2.8}$$

where $\epsilon \approx \sqrt{B^{-1}}$. This potential, however, allows for an unnatural, deeply bound state near the ionic cores, as discussed by Loudon and Haines [Hai69, Lou59]. To avoid having to deal with this state, we reintroduce the singularities at the nuclei in a controllable manner by means of a δ-function of strength λ, which penalizes the deeply bound states, but does not significantly influence the "natural" states of the system

$$V_\epsilon(z) = \frac{-1}{\sqrt{z^2 + \epsilon^2}} + \lambda\delta(z). \tag{6.2.9}$$

Our specific choice of regularization uses $\epsilon = 10^{-2}$ and $\lambda = 1/(2\epsilon) = 50$, for reasons discussed in Section 6.3.

We apply the frozen gas approximation to the ultracold Rydberg crystal, as the time scale of the electronic dynamics is much shorter than that of the core dynamics, and place cores at distinct and controllable locations separated by a length $2a$. The model Hamiltonian for a single electron in an N ion potential, known as a Coulomb comb, is

$$H = T + \sum_{m=-N/2}^{N/2} V_\epsilon(z - 2ma), \tag{6.2.10}$$

where T is the kinetic energy operator, which we extend to two electron calculations using the model Hamiltonian

$$H = \sum_i H_i - \sum_{j>i} V_\epsilon^+(z_i - z_j), \tag{6.2.11}$$

where H_i is the single electron Hamiltonian of the ith electron eq. (6.2.10) and V_ϵ^+, representing electron-electron repulsion, is the same as V_ϵ, but with λ replaced by $-\lambda$.

6.3 One electron two ionic cores

For a single electron in a 1D Coulomb comb, the Schrödinger equation with the Hamiltonian eq. (6.2.10) can be solved directly by piecewise numerical integration, when λ is either 0 or ∞, see fig. 6.2. These values of λ are particularly easy to use in a numerical integration method, as they can be implemented by an appropriate choice of boundary conditions for the single electron wave function on the site of the ionic core. As can be seen in fig. 6.2, the energy and even the number of electronic states is highly dependent on this choice of boundary condition.

For $\lambda = 0$, we observe in Fig. 6.2, like ref. [Lou59, Lou16], a set of states, which are locally asymmetric around the core sites, with energies that do not conform to the Rydberg energies at large separation a; we call these 1D specific states. We also observe the deeply bound states, which is not visible in fig. 6.2. The wave functions of these deeply bound states peak sharply at the core sites and are not possible states. When $\lambda = \infty$, which implies that the wave function must be zero at the core sites. However, the other states of the system are also affected, when λ is increased, and the 1D specific states are not available, when $\lambda = \infty$. For both $\lambda = 0$ and $\lambda = \infty$, we observe a series of bound states, the first of which have a mean distance between the ions of around 2.2 for $\lambda = \infty$, which is about three times the distance between the nuclei in 3D H_2, and around 3 for $\lambda = 0$.

In addition, the boundary conditions associated with large λ prevent the electrons from circumventing the cores, a behavior which is intrinsically unphysical and must be remedied in order to be comparable to any future experiment, as even the best quasi 1D Coulomb comb is fully 3D near the cores.

To remove the deeply bound states, while not introducing boundary conditions at the core sites, we have chosen to work with a value for the λ-parameter
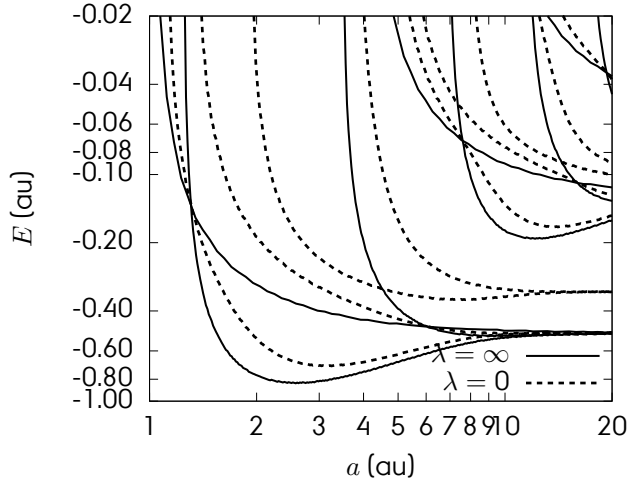
Figure 6.2: *Energy spectra of a single electron in the potential of two cores of unitary charge vs core separation. Solid curves are the spectra of the model with $\lambda = \infty$ and dotted curves are calculated using $\lambda = 0$, both with $\epsilon = 10^{-2}$. The spectra differ significantly and it is clear that the λ-parameter plays an important role in the model. The deeply bound states of [Lou59, Lou16] for $\lambda = 0$ are not visible.*

that is strong enough to effectively penalize the deeply bound states, while not significantly influencing the 1D specific states. A logical choice for the value of the parameter is

$$\lambda = \frac{1}{2\epsilon}, \tag{6.3.1}$$

as this will, according to the virial theorem, penalize the deeply bound state with an energy corresponding to its binding energy, in the limit of vanishing ϵ.

We have found the eigenstates of the Hamiltonian eq. (6.2.10) with $\epsilon = 10^{-2}$ and $\lambda = 50$ using stochastic variation (SV) on correlated Gaussians, which is useful for finding the lowest eigenstates of a system with a large parameter space and many local minima [Suz03]. The energies of the system can be seen in fig. 6.3. As can be seen in the figure, the 1D specific states, except the deeply bound state, are still present for large distances between the cores. The bound states of the system are still present and binding, with a core distance of the lowest energy state of 2.2, similar to that of $\lambda = \infty$ in fig. 6.2.

The noise in the energies presented in fig. 6.3 is due to the nature of the variational approach we have taken to find the eigenstates of the Hamiltonian. The figure only represents upper bounds for the individual energy level, and our model has not been able to fully converge on all levels. However, the noise is somewhat amplified by the logarithmic axes of the figure.

Our implementation of the SV method provides us with the eigenstates of the Hamiltonian eq. (6.2.10) expanded in a Gaussian basis, which allows us to calculate the wave function and a range of quantum mechanical observables. In
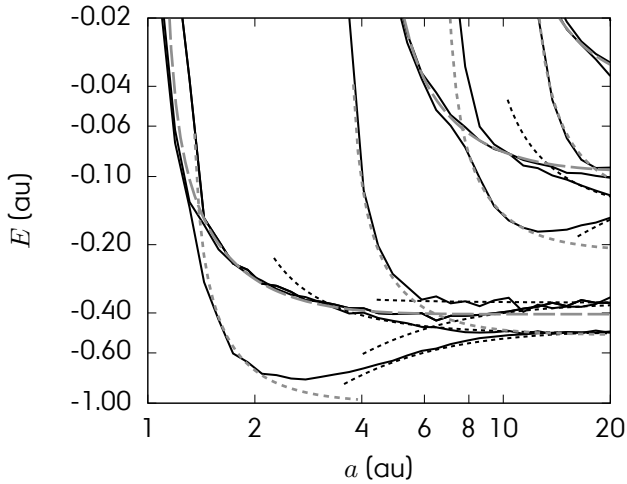
Figure 6.3: *Energy of a single electron in the potential of two cores of unitary charge (black solid) vs core separation. We see both the 1D specific states that do not conform to the Rydberg formula at large a as well as the more familiar states, which do line up with the Rydberg energies at large a. In the large a limit the curves are described by permanent dipole interactions (black dotted), and in the small separation limit the unbinding states are described by Yukawa curves (gray dashed) corresponding to Debye shielding. For the binding states the energies are dominated by a strong increase in kinetic energy for decreasing a. This is described by a Yukawa potential with the addition of a a^{-3} curve and an energy offset (gray dotted).*

fig. 6.4 we plot the root-mean-square (rms) value of the electron's z coordinate. Since the $\langle r \rangle$ of an electron in a symmetric potential is always 0, the rms value is identical to the standard deviation in the electron position. We will use the rms value as an estimate for the mean position of the electron.

By comparing the energies in fig. 6.3 with the mean position of the electron in fig. 6.4, we notice that the binding states are characterized by rms z-values less than a, *ie.* the electron is located between the cores. Since the ionic cores constitute (weak) potential barriers, the electron is more or less confined to the area between the cores. This means that as the distance between the cores decreases, the curvature of the wave function, and hence the kinetic energy of the electron, increases rapidly. When the distance between the ionic cores is smaller than 2, the energy of all states with the electron situated between the cores is positive and the electron is forced outside of the Coulomb comb.

If we, as a simple estimate, ignore the change in electron energy due to the potential barrier between the ionic cores, we find that the kinetic energy of the confined electron will decrease with distance between the cores cubed. This is seen in fig. 6.3, where the grey dotted lines match up with the energies of the
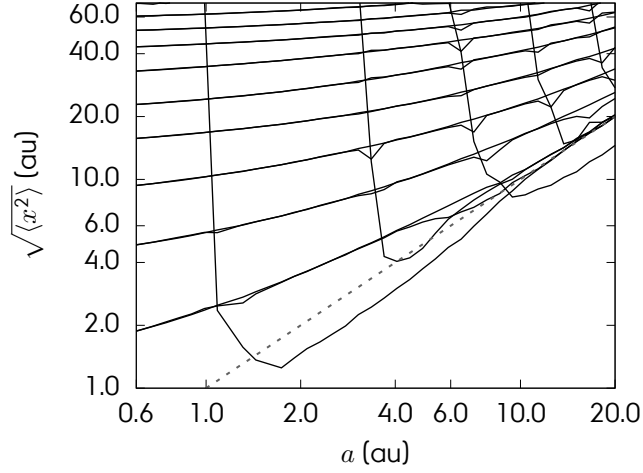
90

Figure 6.4: *Root-mean-square values of the position of a single electron in the potential of two cores of unitary charge, with $\epsilon = 10^{-2}$ and $\lambda = 50$. Dashed line is $\sqrt{z^2} = a$, corresponding to the placement of the ionic cores. For small core separations a, the electron is predominantly situated outside the cores, but from $a \approx 1.5$ on, some electronic states exist, with the electron situated between the cores.*

bound states and are determined by

$$\Upsilon(a) = 2E_{n_\infty} + \frac{\exp\left[-a/l_{n_\infty}\right]}{a} + \frac{G_{n_\infty}}{a^3}, \tag{6.3.2}$$

where E_{n_∞} is an energy offset (found to be equal to the energy of the state at infinite separation), l_{n_∞} is the quantum Debye screening length, which we will discuss shortly, and G_{n_∞} is a constant, all of which are dependent on the principal quantum number of the state at infinite distance between the ionic cores n_∞. This increase in kinetic energy only occurs for states, where the electron is located between the cores (region II in fig. 6.1). For these states, the third term in eq. (6.3.2) is dominant and, since it is an effect due to the geometry of the system and blocks the electron from entering the space between the cores, we call this the geometric blocking term. We have determined G_{n_∞} for the first few states and found that it scales as

$$G_{n_\infty} \sim \left(n_\infty{}^2 \mp \frac{n_\infty}{2}\right)^3 \sim n_\infty^6, \tag{6.3.3}$$

with the sign of the second term dependent on the global symmetry of the state. Disregarding the interaction energy of the ionic cores, the first state, where the electron is located between the cores, becomes energetically favorable at $a = \frac{1}{2}$. We can determine a length scale

$$L_{n_\infty} = 2\sqrt[3]{G_{n_\infty}} \sim 2n_\infty{}^2 \mp n_\infty, \tag{6.3.4}$$

at which it becomes energetically possible for the electron to be located between the ionic cores. This sets a length scale for the system as a whole.
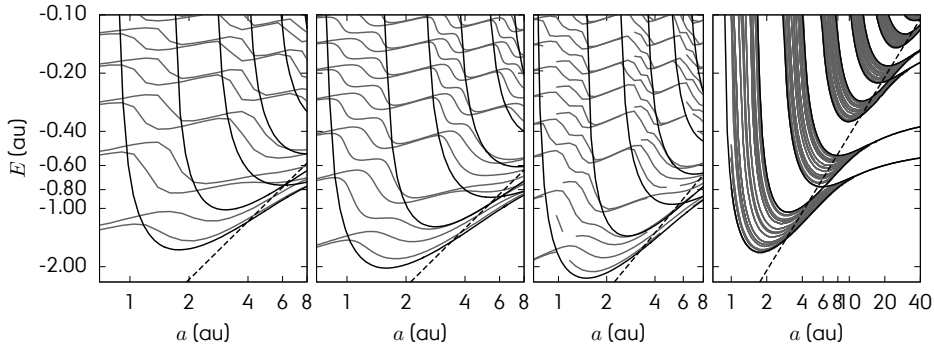

Figure 6.5: *Energies in systems with 3 (a), 4 (b), 5 (c) core systems and a periodic lattice (d). Interaction energy between the cores has been subtracted for comparison. For the non periodic lattices (a, b and c), states, where the electron is located between the cores, only become energetically available inside the energy bands of a periodic lattice (d), indicated by solid black lines. In all subfigures, dashed black indicate the maximal potential inside the core structure. Some points are missing due to the resolution that was attainable in the simulation. The shape of the potential in (d) $V_{periodic}$ is modeled as the center-most inner region of an $N = 100$ ion regular lattice, with an offset such that the potential at 0 is $V_{periodic}(0) = -4/a$.*

The second term in eq. (6.3.2) is a Yukawa potential, which describes the interaction between two charged particles, where the charge is screened at lengths larger than the Debye length l_{n_∞}. When the electron is situated between the cores, is free to find the optimally screening wavefunction, and the screening length for these states is, independently of the state, equal to 1. This screening is a feature of plasmas, where the charges can move around, such that a test charge will not experience the full Coulomb potential of nearby charges, but rather a screened Yukawa potential. This is not the case, when the electron is not located between the cores.

For states, where the electron is not located between the cores, we do not see geometric blocking, as the electron wave function can be redistributed, thereby minimizing the increase in kinetic energy of the system. However, for these states, the charges of the cores are not as efficiently screened, and we have to consider the state dependence of the quantum Debye length l_{n_∞}. As can be seen from the gray dashed lines in Fig. 6.3, which are described by

$$Y(a) = E_{n_\infty} + \frac{\exp\left[-a/l_{n_\infty}\right]}{a}, \tag{6.3.5}$$

where the constants are the same as in eq. (6.3.2). However, for states, where the electron is not located in the area between the cores, the quantum Debye length is strongly dependent on the principal quantum number n_∞, as counted at infinite

distance between the cores. Again we find the same length scale dependence on n_∞ as in eq. (6.3.4), as can be seen in fig. 6.3, where gray dashed lines follow the Yukawa potential eq. (6.3.5) with Debye length

$$l_{n_\infty} = 2n_\infty{}^2 \mp n_\infty = L_{n_\infty}. \tag{6.3.6}$$

This provides a universal scaling for the 1D quantum plasma system, which works well for states, where the electron is located between the ionic cores and states where the electron is located outside the ionic structure.

Finally, using the rms value of the electron coordinate, shown in fig. 6.4, we can determine the permanent dipole moment D of the core-electron system in the presence of a charged ionic core as

$$D_n(a) = \sqrt{\langle z^2 \rangle} - a, \tag{6.3.7}$$

which is dependent on the distance between the ionic cores a and the principal quantum number n. For states where the electron is located between the ionic cores, this results in a negative dipole moment and thus an attractive force between the cores. For states with the electron on the outside of the core structure, on the other hand, the dipole moment is positive, leading to a repulsive force between the cores. Thus, we find the energy of the system at large distances as a multipole expansion

$$E_n(a) = E_{n_\infty} + \frac{D_n(a)}{a^2}, \tag{6.3.8}$$

where $E_n(a)$ is the energy of the nth state at core distance a and E_{n_∞} is the energy at infinite distance between the cores. This expansion is shown with black, dashed curves in fig. 6.3, and predicts the simulated curves well.

For states where the electron is located between the cores and the energy of the electron is large enough to pass over the potential barrier between the cores, we can assume that the electron density is equal to the inverse distance between the cores $1/a$, in 1D. This yields the plasma parameter, equal to the number of electrons within a Debye length, as

$$\Lambda \sim \frac{2n_\infty^2 \mp n_\infty}{a}. \tag{6.3.9}$$

For $n_\infty = 1$ this is never larger than 1, since the energy of states, where the electron is located between the cores, is positive, when $a < 1$. Therefore the system is in the regime of strongly coupled plasmas. However, for excited states, the scaling relation found in eq. (6.3.4) still holds, and both the Debye length and the distance between the core, where a higher excited electronic state is energetically available, increase at the same rate and the parameter Λ will asymptotically approach 1 as n_∞ increases.

Increasing the number of ionic cores in the system, which leads to a more natural net surplus of charge [SV13, Poh03], has a few insights to be revealed, as can be seen in fig. 6.5, where such systems are shown. The interaction energy between the ionic cores has been subtracted to make the subfigures comparable. Due to

limitations in the simulation, a few points are missing from fig. 6.5 d, this is not a physical phenomenon, but rather a flaw in the simulation.

Fig. 6.5 shows the energies of aperiodic systems with 3, 4 or 5 ionic cores (a through c) as well as the energy bands found using a periodic lattice where the shape matches the center most area of a 100 core potential (d). The energies of the aperiodic systems show two different trends; one is a relatively stable increase with a corresponding to the 2 core states, where the electron is located outside the ionic core structure. This is most noticeable outside the energy bands. The other is a strong drop in energy corresponding to the 2 core states, where the electron is located between the cores. For systems with N cores, there are $N-1$ areas between the cores, and in fig. 6.5 we indeed observe exactly $N-1$ states, where the electron is located between the cores.

The most striking feature of fig. 6.5, is that the states, where the electron is located between the cores, fill up the bands of the periodic lattice (subfigure d, and indicated by black solid lines in a through c) one state at a time, when adjusted for the energy offset associated with the number of cores. Also indicated in the figure, by black dashed lines, is the maximal height of the summed Coulomb potential between the ionic cores, *ie.* the height of the potential between the first and second core. For energies higher than what is indicated by these lines, the electron is free to travel across the entire core structure.

This is essentially an atomic scale conductor, constructed from the ground up, using a finite size 1D Coulomb lattice. This could provide helpful insights into the formation of energy bands and the insulator-conductor crossover.

6.4   Two electrons two ionic cores

Increasing the number of electrons in the calculation presents a new set of problems. First and foremost is the treatment of symmetry in the system, which for a single electron is limited to parity symmetry. For two electrons, however, we also have to consider exchange symmetry of the electrons. To facilitate this, we use Jacobi coordinates, that is a center-of-mass (COM) coordinate R and a relative coordinate r, indicating the distance between the two electrons. We can then express the unsymmetrized wave function of the electrons as a function of the Jacobi coordinates

$$\psi(r, R). \tag{6.4.1}$$

We build the symmetrized two-electron wave functions from eq. (6.4.1)

$$\psi_{SS}(r, R) = \psi(r, R) + \psi(-r, R) + \psi(r, -R) + \psi(-r, -R)$$
$$\psi_{SA}(r, R) = \psi(r, R) - \psi(-r, R) - \psi(r, -R) + \psi(-r, -R)$$
$$\psi_{AS}(r, R) = \psi(r, R) + \psi(-r, R) - \psi(r, -R) - \psi(-r, -R)$$
$$\psi_{AA}(r, R) = \psi(r, R) - \psi(-r, R) + \psi(r, -R) - \psi(-r, -R), \tag{6.4.2}$$

where the subscripts are S (A) for (a)symmetric, the first subscript indicates symmetry under parity and the second indicates symmetry under particle exchange.

Applying the parity P and exchange χ operators to the unsymmetrized two-electron wave function, we get

$$P\psi(r, R) = \psi(-r, -R)$$
$$\chi\psi(r, R) = \psi(-r, R)$$
$$P\chi\psi(r, R) = \chi P\psi(r, R) = \psi(r, -R). \tag{6.4.3}$$

Due to the Coulomb interaction between the electrons, the wave function is always zero when $r = 0$ and the energy of the state is unchanged under sign flip of the r coordinate, therefore symmetry considerations only concern what happens, when R is replaced with $-R$. For the symmetrized wave functions in eq. (6.4.2) we find

$$\psi_{SS}(r, -R) = \quad \psi_{SS}(r, R)$$
$$\psi_{SA}(r, -R) = -\psi_{SA}(r, R)$$
$$\psi_{AS}(r, -R) = -\psi_{AS}(r, R)$$
$$\psi_{AA}(r, -R) = \quad \psi_{AA}(r, R). \tag{6.4.4}$$

Thus the symmetry considerations of the two-electron system boil down to R-symmetric (ψ_{SS} and ψ_{AA}) and R-asymmetric (ψ_{SA} and ψ_{AS}) states, whereas r-symmetry does not influence energy.
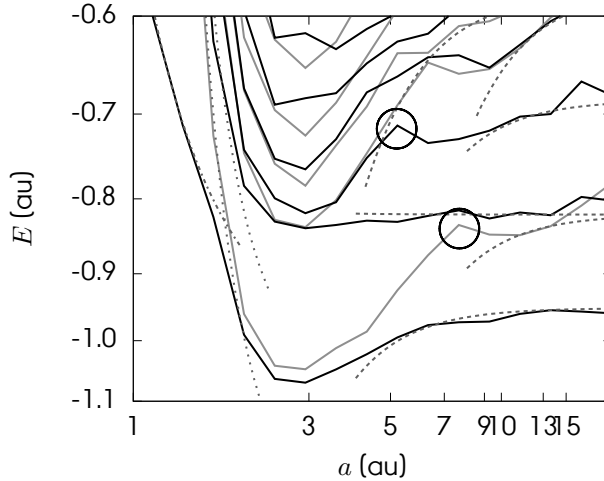
Figure 6.6: *Spectrum of two interacting 1D hydrogen atoms Black curves are R-symmetric states, gray curves are R-asymmetric states. No states with two electrons in the central region appear due to the strong Coulomb repulsion between them. Grey dots are the geometric blocking and gray dot-dash are Debye shielding. Grey dashes are permanent dipole interaction. Dark circles indicate examples of cusps in energy. The jaggedness of the curves is due to limitations on computational power.*

Taking these symmetry considerations into account, we show the energies of the 1D two-electron-two-core system in fig. 6.6. Solid black curves are R-symmetric

and solid gray are R-asymmetric. The jaggedness of the lines is due to limitations in computation time. In the limit of large distance between the cores a, the system will form two independent 1D atoms from an electron and a core each.

At small core-to-core distances a, the electrons can not be located between the cores for the same reasons as in the single electron case. Due to the Coulomb interaction between the electrons, the electrons are located at opposite ends of the core structure. This can only happen for R-symmetric states, as the electron center of mass is in the center of the core structure. In fig. 6.6 we see that the lowest (and R-symmetric) state follows the Yukawa potential (gray dash-dot) of a screened Coulomb system. However, for R-asymmetric states the center of mass of the electrons does not lie in the center of the core structure, and one electron is located between the cores, whereas the other is located outside the cores. These states are only allowed, when the distance between the cores is large enough to avoid the geometric blocking discussed in the single electron case. Since one electron is located outside the core structure, though, the quantum Debye length of these states is no longer unity for all states, but rather the natural scale of the system L_{n_∞}. Combining this with eq. (6.3.2), we get

$$\Upsilon_2(a) = 2E_{n_\infty} + \frac{\exp\left[-a/L_{n_\infty}\right]}{a} + \frac{G_{n_\infty}^{(2)}}{a^3}, \tag{6.4.5}$$

where $G_{n_\infty}^{(2)} \sim 2G_{n_\infty}$ is the two electron equivalent of G_{n_∞}. These Yukawa approximations are shown (for the first few states only to avoid confusing the figure) by the grey dotted curves in fig. 6.6.

For large distances between the cores, the system behaves as two permanent dipoles, as the electrons do not easily cross the core sites and we can approximate the energy by

$$E_n(a) = En_\infty + \frac{D_n^1(a)D_n^2(a)}{a^3}, \tag{6.4.6}$$

where D_n^i is the dipole moment of the individual 1D atom. A fair approximation can be achieved using the dipole moments from the single electron case (eq. (6.3.7)), as seen in the gray dashed lines in fig. 6.6.

One final feature of the energies seen in fig. 6.6 is the cusp (examples indicated by circles) in energy for some states, most clearly visible for the lowest R-asymmetric state around $a = 7$. We will call the distance, where the cusp is centered (for a given state) the cusp distance (for that state). For states, where the cusp exists, this means that a second local minimum exists in energy, resulting in a second stability point for the bound state of the system. This is a feature of 1D that we can not expect to see in a system of higher dimensionality, as the electrons can more freely circumvent the ionic cores.

The cusp only appears for states, where the center of mass of the electrons is moved away from the core center of mass, which means it is only there for R-asymmetric states and certain excited R-symmetric states. Since the probability of finding the electrons at equal but opposite distances from the core center of mass is zero, along with the strong Coulomb interaction between them, only one electron can be located between the cores for a smaller than the cusp distance. When a is larger than the cusp distance, the wavefunction of the second electron

can partially spill into the area between the cores, giving a small probability of finding both electrons between the cores. This spilling happens smoothly and we therefore see this appearing as a small perturbation to the state, rather than a new state entering the picture. For states where the electron wave function is not zero for $R = 0$, this transition happens more gradually and we do not see the cusp in energy.

6.5   Conclusion and outlook

In this paper we have presented a 1D toy model for the exploration of quantum plasmas. We have argued for the possibility of using Rydberg atoms in strong magnetic fields to explore the field of 1D Coulomb systems, due to the strong effect of the magnetic field along with the pin point accuracy of Rydberg excitation in atomic clouds.

 We have explored the system using a regularized potential, which, while not significantly influencing the energies of the states, allows the electrons to circumvent the ions. This removes some of the most unnatural consequences of the 1D treatment, previously discussed in literature.

 We have presented expressions for the state dependent quantum Debye length and found natural scaling for the system, which describes all length scales of the system. This length scale also describes the strength of the geometric blocking effect, where a rise in kinetic energy forces the electron out of the area between the ionic cores. This effect is also present in systems with more electrons, and repeats at larger core distances for the second electron. We have shown useful expressions for approximating the energies of both one and two electron systems, beyond the regimes discussed in this paper, with multipole expansions in the large core distance limit. Further, we presented results of systems with multiple ionic cores as well as a periodic lattice, and showed that the energy bands of the system is an emergent feature, building up slowly and visible in even the smallest 1D systems.

 This work has been somewhat limited in the achievable size of the simulated system. Of the two methods used, direct numerical integration of the Schrödinger equation has yielded the best results in the single electron case, but is difficult to scale up in number of simulated electrons. The SV method, on the other hand, is easy to scale up, but has suffered from the singularities intrinsic to the 1D treatment. We believe that, despite the mediocre results, the SV method is the best way forward, when expanding the system to 2- or 3D. Scaling up in 1D, however, the SV method could benefit from basis functions that are specifically designed for that purpose, but it has not been the intention of this paper to find such basis functions. Future work should focus on expanding the number of electrons in the simulation, but increasing both energy resolution as well as convergence would be of great interest.

 As of right now, it is perhaps not feasible to explore the regime experimentally, but with increasing principal quantum number in state of the art Rydberg experiments, the required magnetic field strengths can be brought within experimental reach. It would be of extreme interest to see experimental exploration of a quasi 1D Coulomb regime.

Acknowledgments

Acknowledgement

This thesis represents the culmination of a lifelong interest in physics and the realisation of a dream I have held since childhood. It would not have been possible for me to achieve this without the help and support of people around me, and of course the financial support of FOM, which about halfway through my PhD became part of NWO.

First of all I would like to thank Servaas and Edgar for giving me the opportunity and for the huge amount of work they have put into the roles as supervisors. Servaas, you have not only supplied fruitful discussions on the research and supported my work, but also provided a great working environment. Always a happy face at group meetings. I also appreciate your annual christmas lunches, bringing your PhD students together in your home. Both I and Christina enjoyed that very much, and we almost miss making 6 litres of risalamande for you and your children. I would also like to thank you for attending our wedding and for the speech you gave at the occasion. Edgar, thank you for your stern reading of my manuscripts without which, most would not have been of the quality they are or perhaps even published. Your feedback has always been quick and precise, giving me a solid base to work from.

I would also like to thank the technical staff at CQT, especially Iman, who has put up with my chats over the morning coffee for several years, and was always happy to talk over the state of the universe or some cool equipment you were building at those early hours before the rest of our colleges showed up. Though I have no expertise in electronics, I believe those morning chats gave me at least a minimal insight into the art and craft of electronic designs. Thank you to Harry and Marco, who were my "victims", when Iman was out. And also to Eddie for your tales of hunting and trips to "Schiesskino", and Ton whom I could still be talking to over coffee to this day. My thanks go out to Betty, for handling all the office tasks and paperwork. For finding my first home and putting up with my slobby travel permits.

Of course my time at CQT would not have been the same without my fellow PhD students. Together, we spent many Thursday evenings at the Caroussel, trying to win the pub quiz, though I think third place was the best we ever achieved. In my first weeks, I went to Durham with Steinar and Gijs, the two experienced PhD students in the group, who introduced me to life with paid lunch, drinks and Dutch card games. Though, we worked on unrelated subjects I think you both were part of what made my time at CQT special. Steinar, we pranked each other and sometimes you deviced something truly devilish, but your conscience always got the better of you, when you thought you crossed the line. I hope you had as much fun as I did. Gijs, you introduced me to the real Dutch cuisine of kapsalon, though

I never quite understood your preference for the place that got Mark sick. Starting their PhDs roughly at the time as me were Wouter, Jasper and my experimental counterpart Tarun. Wouter, you were always up for a drink Thursdays and I think you were part of the life and soul of our merry band of PhD students. Jasper, you always tried to get me to join the soccer team. I hope you have had more success with your new house. I will forever associate the name Jasper with cats and pizzas. Tarun, you were responsible for the experimental part of our project, and I was sad that it didn't work out. We have shared posters at many conferences, trying to encompass two rapidly diverting subprojects. I think we both experienced both the sinking feeling of failure and the joy of success of the project during our time working together. Thomas, though your computer was blowing hot air across my desk all the time, I think you were a great office buddy. Marc, Jim and Wiebe, the experimental people one could pull a prank on, when you were in the lab. Silvia, Denise, Paul and Victor, Servaases new crew. I hope you will have as much fun in the future as we did, when I was there. May the Carrousel quiz master smile at you all.

My thanks also go out to my family. To my mum, dad, my sister Anne Christine and her family, who nurtured my interest in physics since I was young. Thank you for supporting my dreams and for pushing me forward. I felt comfortable going abroad for my PhD, knowing that I would always find a good time and a place to sleep, when I went home to for holidays and family occasions. Both me and Christina looked forward to your visits.

Christina, before I left for Eindhoven, I asked you if it was ok. Had I known at the time how many tears both of us would shed, saying goodbye on the train stations in Aarhus and Eindhoven, I would probably not have left. Thank you for saying yes to me leaving, thanking for saying yes to moving to Eindhoven with me and finally thank you for saying yes to me on the 12th of August 2017. Without you, I would not have made it, tak.

Bibliography

[Aas16]   D. Aasen, M. Hell, R. V. Mishmash, A. Higginbotham *et al.*, *Milestones Toward Majorana-Based Quantum Computing*, Phys. Rev. X **6**, 031016 (2016), doi:10.1103/PhysRevX.6.031016.

[Alb15]   T. Albash, T. Rønnow, M. Troyer and D. Lidar, *Reexamining classical and quantum models for the D-Wave One processor*, The European Physical Journal Special Topics **224**, 111 (2015), ISSN 1951-6401, doi: 10.1140/epjst/e2015-02346-0.

[Aru19]   F. Arute, K. Arya, R. Babbush, D. Bacon *et al.*, *Quantum supremacy using a programmable superconducting processor*, Nature **574**, 505 (2019), ISSN 1476-4687, doi:10.1038/s41586-019-1666-5.

[Ate07a]   C. Ates, T. Pohl, T. Pattard and J. M. Rost, *Antiblockade in Rydberg Excitation of an Ultracold Lattice Gas*, Phys. Rev. Lett. **98**, 023002 (2007), doi:10.1103/PhysRevLett.98.023002.

[Ate07b]   C. Ates, T. Pohl, T. Pattard and J. M. Rost, *Many-body theory of excitation dynamics in an ultracold Rydberg gas*, Phys. Rev. A **76**, 013413 (2007).

[Ate11]   C. Ates, S. Sevinçli and T. Pohl, *Electromagnetically induced transparency in strongly interacting Rydberg gases*, Phys. Rev. A **83**, 041802 (2011), doi:10.1103/PhysRevA.83.041802.

[Bá87]   L. Bányai, I. Galbraith, C. Ell and H. Haug, *Excitons and biexcitons in semiconductor quantum wires*, Phys. Rev. B **36**, 6099 (1987), doi:10.1103/PhysRevB.36.6099.

[Bal16]   C. J. Ballance, T. P. Harty, N. M. Linke, M. A. Sepiol and D. M. Lucas, *High-Fidelity Quantum Logic Gates Using Trapped-Ion Hyperfine Qubits*, Phys. Rev. Lett. **117**, 060504 (2016), doi:10.1103/PhysRevLett.117.060504.

[Bal17]   C. J. Ball, P.-F. Loos and P. M. W. Gill, *Molecular electronic structure in one-dimensional Coulomb systems*, Phys. Chem. Chem. Phys. **19**, 3987 (2017), doi:10.1039/C6CP06801D.

[Bar95]   A. Barenco, C. H. Bennett, R. Cleve, D. P. DiVincenzo *et al.*, *Elementary gates for quantum computation*, Phys. Rev. A **52**, 3457 (1995), doi: 10.1103/PhysRevA.52.3457.

[Bar13] W. Barford, *Excitons in Conjugated Polymers: A Tale of Two Particles*, The Journal of Physical Chemistry A **117**, 2665 (2013), doi:10.1021/jp310110r. PMID: 23427996.

[Bar16] D. Barredo, S. de Léséleuc, V. Lienhard, T. Lahaye and A. Browaeys, *An atom-by-atom assembler of defect-free arbitrary two-dimensional atomic arrays*, Science **354**, 1021 (2016), ISSN 0036-8075, doi:10.1126/science.aah3778.

[Bea03] S. Beauregard, *Circuit for Shor's Algorithm Using 2N+3 Qubits*, Quantum Info. Comput. **3**, 175 (2003), ISSN 1533-7146.

[Bel13] M. A. Bellos, R. Carollo, J. Banerjee, E. E. Eyler, P. L. Gould and W. C. Stwalley, *Excitation of Weakly Bound Molecules to Trilobitelike Rydberg States*, Phys. Rev. Lett. **111**, 053001 (2013), doi:10.1103/PhysRevLett.111.053001.

[Ben08] J. Benhelm, G. Kirchmair, C. F. Roos and R. Blatt, *Towards fault-tolerant quantum computing with trapped ions*, Nature Physics **4**, 463 EP (2008).

[Ber97] E. Bernstein and U. Vazirani, *Quantum Complexity Theory*, SIAM Journal on Computing **26**, 1411 (1997), doi:10.1137/S0097539796300921.

[Bet09] I. I. Beterov, I. I. Ryabtsev, D. B. Tretyakov and V. M. Entin, *Quasiclassical calculations of blackbody-radiation-induced depopulation rates and effective lifetimes of Rydberg nS, nP, and nD alkali-metal atoms with $n \leq 80$*, Phys. Rev. A **79**, 052504 (2009), doi:10.1103/PhysRevA.79.052504.

[Bet15] I. I. Beterov and M. Saffman, *Rydberg blockade, Förster resonances, and quantum state measurements with different atomic species*, Phys. Rev. A **92**, 042710 (2015), doi:10.1103/PhysRevA.92.042710.

[Bij11] R. M. W. van Bijnen, S. Smit, K. A. H. van Leeuwen, E. J. D. Vredenbregt and S. J. J. M. F. Kokkelmans, *Adiabatic formation of Rydberg crystals with chirped laser pulses*, Journal of Physics B: Atomic, Molecular and Optical Physics **44**, 184008 (2011).

[Bij13] R. van Bijnen, *Quantum Engineering with Ultracold Atoms*, Ph.D. thesis, Eindhoven University of Technology (2013).

[Bij14] R. M. W. van Bijnen, C. Ravensbergen, D. Bakker, G. J. Dijk, S. Kokkelmans and E. Vredenbregt, *Patterned Rydberg excitation and ionisation with a spatial light modulator*, New Journal of Physics **17** (2014), doi:10.1088/1367-2630/17/2/023045.

[Bij15] R. M. W. van Bijnen, C. Ravensbergen, D. J. Bakker, G. J. Dijk, S. J. J. M. F. Kokkelmans and E. J. D. Vredenbregt, *Patterned Rydberg excitation and ionization with a spatial light modulator*, New Journal of Physics **17**, 023045 (2015), doi:10.1088/1367-2630/17/2/023045.

[Boc99] M. Bockrath, D. H. Cobden, J. Lu, A. G. Rinzler, R. E. Smalley, L. Balents and
P. L. McEuen, *Luttinger-liquid behaviour in carbon nanotubes*, Nature
397, 598 EP (1999).

[Boe18] A. G. Boetes, R. V. Skannrup, J. Naber, S. J. J. M. F. Kokkelmans and R. J. C.
Spreeuw, *Trapping of Rydberg atoms in tight magnetic microtraps*, Phys.
Rev. A **97**, 013430 (2018), doi:10.1103/PhysRevA.97.013430.

[Boi02] C. Boisseau, I. Simbotin and R. Côté, *Macrodimers: Ultralong Range
Rydberg Molecules*, Phys. Rev. Lett. **88**, 133004 (2002), doi:10.1103/
PhysRevLett.88.133004.

[Boi18] S. Boixo, S. V. Isakov, V. N. Smelyanskiy, R. Babbush *et al.*, *Characteriz-
ing quantum supremacy in near-term devices*, Nature Physics **14**, 595
(2018), ISSN 1745-2481, doi:10.1038/s41567-018-0124-x.

[Bon10] M. Bonitz, N. Horning and L. P., *Introduction to Complex Plasmas*,
Springer Berlin Heidelberg (2010), ISBN 9783642105913, doi:10.1007/
978-3-642-10592-0.

[Boo15] D. Booth, S. T. Rittenhouse, J. Yang, H. R. Sadeghpour and J. P. Shaffer,
*Production of trilobite Rydberg molecule dimers with kilo-Debye perma-
nent electric dipole moments*, Science **348**, 99 (2015), ISSN 0036-8075,
doi:10.1126/science.1260722.

[Bra03] B. Bransden, C. Joachain and T. Plivier, *Physics of Atoms and Molecules*,
Pearson Education, Prentice Hall (2003), ISBN 9780582356924.

[Bra09] D. B. Branden, T. Juhasz, T. Mahlokozera, C. Vesa *et al.*, *Radiative life-
time measurements of rubidium Rydberg states*, Journal of Physics
B: Atomic, Molecular and Optical Physics **43**, 015002 (2009), doi:
10.1088/0953-4075/43/1/015002.

[Bre00] K.-H. Brenner, *Method for designing arbitrary two-dimensional continu-
ous phase elements*, Opt. Lett. **25**, 31 (2000), doi:10.1364/OL.25.000031.

[Bri07] E. Brion, L. H. Pedersen and K. Mølmer, *Adiabatic elimination in a lambda
system*, Journal of Physics A: Mathematical and Theoretical **40**, 1033
(2007), ISSN 1751-8121.

[Bro16] A. Browaeys, D. Barredo and T. Lahaye, *Experimental investigations of
dipole–dipole interactions between a few Rydberg atoms*, Journal of
Physics B: Atomic, Molecular and Optical Physics **49**, 152001 (2016).

[Bru15a] G. D. Bruce, T. Harte, D. Bowman, P. Ireland, J. Keeling and D. Casset-
tari, *Phase-engineered Light Patterns for Ultracold Atom Experiments*,
in *2015 European Conference on Lasers and Electro-Optics - European
Quantum Electronics Conference*, Optical Society of America (2015).

[Bru15b] G. D. Bruce, M. Y. H. Johnson, E. Cormack, D. A. W. Richards, J. Mayoh
and D. Cassettari, *Feedback-enhanced algorithm for aberration correc-
tion of holographic atom traps*, Journal of Physics B: Atomic, Molecular

and Optical Physics **48**, 115303 (2015), doi:10.1088/0953-4075/48/11/115303.

[Büc07] H. P. Büchler, A. Micheli and P. Zoller, *Three-body interactions with cold polar?molecules*, Nature Physics **3**, 726 (2007), ISSN 1745-2481, doi:10.1038/nphys678.

[Car12] J. D. Carter, O. Cherry and J. D. D. Martin, *Electric-field sensing near the surface microstructure of an atom chip using cold Rydberg atoms*, Phys. Rev. A **86**, 053401 (2012), doi:10.1103/PhysRevA.86.053401.

[CGm] *Correlated Gaussian Method in Quantum Mechanics*, `https://en.wikibooks.org/wiki/Correlated_Gaussian_method_in_Quantum_Mechanics`. Accessed: 2019-03-27.

[Cha03] A. M. Chang, *Chiral Luttinger liquids at the fractional quantum Hall edge*, Rev. Mod. Phys. **75**, 1449 (2003), doi:10.1103/RevModPhys.75.1449.

[Cha07] J.-C. Charlier, X. Blase and S. Roche, *Electronic and transport properties of nanotubes*, Rev. Mod. Phys. **79**, 677 (2007), doi:10.1103/RevModPhys.79.677.

[Che16] L. W. Cheuk, M. A. Nichols, K. R. Lawrence, M. Okan *et al.*, *Observation of spatial charge and spin correlations in the 2D Fermi-Hubbard model*, Science **353**, 1260 (2016), ISSN 0036-8075, doi:10.1126/science.aag3349.

[Cho05] J. H. Choi, J. R. Guest, A. P. Povilus, E. Hansis and G. Raithel, *Magnetic Trapping of Long-Lived Cold Rydberg Atoms*, Phys. Rev. Lett. **95**, 243001 (2005), doi:10.1103/PhysRevLett.95.243001.

[Cir95] J. I. Cirac and P. Zoller, *Quantum Computations with Cold Trapped Ions*, Phys. Rev. Lett. **74**, 4091 (1995), doi:10.1103/PhysRevLett.74.4091.

[Cir12] J. I. Cirac and P. Zoller, *Goals and opportunities in quantum simulation*, Nature Physics **8**, 264 EP (2012).

[Col89] N. Collings, W. A. Crossland, P. J. Ayliffe, D. G. Vass and I. Underwood, *Evolutionary development of advanced liquid crystal spatial light modulators*, Appl. Opt. **28**, 4740 (1989), doi:10.1364/AO.28.004740.

[Cop17] B. J. Copeland, *The Modern History of Computing*, in E. N. Zalta (ed.) *The Stanford Encyclopedia of Philosophy*, Metaphysics Research Lab, Stanford University, winter 2017 edn. (2017).

[Dav02] T. Davis, *2D magnetic traps for ultra-cold atoms: a simple theory using complex numbers*, The European Physical Journal D - Atomic, Molecular, Optical and Plasma Physics **18**, 27 (2002), ISSN 1434-6079, doi:10.1140/e10053-002-0003-x.

[Deg17] C. L. Degen, F. Reinhard and P. Cappellaro, *Quantum sensing*, Rev. Mod. Phys. **89**, 035002 (2017), doi:10.1103/RevModPhys.89.035002.

[Deu85]   D. Deutsch and R. Penrose, *Quantum theory, the Church-Turing principle and the universal quantum computer*, Proceedings of the Royal Society of London. A. Mathematical and Physical Sciences **400**, 97 (1985), doi: 10.1098/rspa.1985.0070.

[DiV00]   D. P. DiVincenzo, *The Physical Implementation of Quantum Computation*, Fortschritte der Physik **48**, 771 (2000), doi:10.1002/1521-3978(200009)48:9/11<771::AID-PROP771>3.0.CO;2-E.

[Dun18]   A. Dunsworth, R. Barends, Y. Chen, Z. Chen *et al.*, *A method for building low loss multi-layer wiring for superconducting microwave devices*, Applied Physics Letters **112**, 063502 (2018), doi:10.1063/1.5014033.

[Egg98]   R. Egger and A. Gogolin, *Correlated transport and non-Fermi-liquid behavior in single-wall carbon nanotubes*, The European Physical Journal B - Condensed Matter and Complex Systems **3**, 281 (1998), ISSN 1434-6036, doi:10.1007/s100510050315.

[Eng14]   W. Engelen, E. Smakman, D. Bakker, O. Luiten and E. Vredenbregt, *Effective temperature of an ultracold electron source based on near-threshold photoionization*, Ultramicroscopy **136**, 73 (2014), ISSN 0304-3991, doi:https://doi.org/10.1016/j.ultramic.2013.07.017.

[Fey82]   R. P. Feynman, *Simulating physics with computers*, International Journal of Theoretical Physics **21**, 467 (1982), ISSN 1572-9575, doi:10.1007/BF02650179.

[Fin94]   A. Finnila, M. Gomez, C. Sebenik, C. Stenson and J. Doll, *Quantum annealing: A new method for minimizing multidimensional functions*, Chemical Physics Letters **219**, 343 (1994), ISSN 0009-2614, doi:https://doi.org/10.1016/0009-2614(94)00117-0.

[fla17]   *Quantum Technologies Flagship Intermediate Report* (2017). Https://ec.europa.eu/digital-single-market/en/news/intermediate-report-quantum-flagship-high-level-expert-group.

[Fol00]   R. Folman, P. Krüger, D. Cassettari, B. Hessmo, T. Maier and J. Schmiedmayer, *Controlling Cold Atoms using Nanofabricated Surfaces: Atom Chips*, Phys. Rev. Lett. **84**, 4749 (2000), doi:10.1103/PhysRevLett.84.4749.

[Fol02]   R. Folman, P. Krüger, J. Schmiedmayer, J. Denschlag and C. Henkel, *Microscopic Atom Optics: From Wires to an Atom Chip*, in B. Bederson and H. Walther (eds.) *Advances In Atomic, Molecular, and Optical Physics*, vol. 48, Academic Press, pp. 263–356 (2002), doi:10.1016/S1049-250X(02)80011-8.

[For99]   L. Fortnow and J. Rogers, *Complexity Limitations on Quantum Computation*, Journal of Computer and System Sciences **59**, 240 (1999), ISSN 0022-0000, doi:https://doi.org/10.1006/jcss.1999.1651.

[Fre06] T. Freeth, Y. Bitsakis, X. Moussas, J. H. Seiradakis *et al.*, *Decoding the ancient Greek astronomical calculator known as the Antikythera Mechanism*, Nature **444**, 587 (2006), ISSN 1476-4687, doi:10.1038/nature05357.

[Fri08] A. Friedenauer, H. Schmitz, J. T. Glueckert, D. Porras and T. Schaetz, *Simulating a quantum magnet with trapped?ions*, Nature Physics **4**, 757 EP (2008).

[Fu18] X. Fu, M. A. Rol, C. C. Bultink, J. van Someren *et al.*, *A Microarchitecture for a Superconducting Quantum Processor*, IEEE Micro **38**, 40 (2018), ISSN 0272-1732, doi:10.1109/MM.2018.032271060.

[Gï4] M. Gärttner, S. Whitlock, D. W. Schönleber and J. Evers, *Semianalytical model for nonlinear absorption in strongly interacting Rydberg gases*, Phys. Rev. A **89**, 063407 (2014), doi:10.1103/PhysRevA.89.063407.

[Gae16] J. P. Gaebler, T. R. Tan, Y. Lin, Y. Wan *et al.*, *High-Fidelity Universal Gate Set for $^9\mathrm{Be}^+$ Ion Qubits*, Phys. Rev. Lett. **117**, 060505 (2016), doi:10.1103/PhysRevLett.117.060505.

[Gal94] T. F. Gallagher, *Rydberg Atoms*, Cambridge Monographs on Atomic, Molecular and Chemical Physics, Cambridge University Press, 1st edn. (1994), ISBN 521021669, doi:10.1017/CBO9780511524530.

[Gal05] T. Gallagher, *Rydberg Atoms*, Cambridge Monographs on Atomic, Molecular and Chemical Physics, Cambridge University Press (2005), ISBN 9780521021661.

[Gam20] F. M. Gambetta, W. Li, F. Schmidt-Kaler and I. Lesanovsky, *Engineering NonBinary Rydberg Interactions via Phonons in an Optical Lattice*, Phys. Rev. Lett. **124**, 043402 (2020), doi:10.1103/PhysRevLett.124.043402.

[GC10] J. Graham-Cumming, *Let's build Babbage's ultimate mechanical computer*, New Scientist (2010).

[Geo14] I. M. Georgescu, S. Ashhab and F. Nori, *Quantum simulation*, Rev. Mod. Phys. **86**, 153 (2014), doi:10.1103/RevModPhys.86.153.

[Ger06] R. Gerritsma and R. J. C. Spreeuw, *Topological constraints on magneto-static traps*, Phys. Rev. A **74**, 043405 (2006), doi:10.1103/PhysRevA.74.043405.

[Ger10] R. Gerritsma, G. Kirchmair, F. Zähringer, E. Solano, R. Blatt and C. F. Roos, *Quantum simulation of the Dirac equation*, Nature **463**, 68 EP (2010).

[Gne09] Y. Gnedin, A. Mihajlov, L. Ignjatović, N. Sakan *et al.*, *Rydberg atoms in astrophysics*, New Astronomy Reviews **53**, 259 (2009), ISSN 1387-6473, doi:https://doi.org/10.1016/j.newar.2009.07.003. Proceedings of the VII Serbian Conference on Spectral Line Shapes (VII SCSLSA) held in Zrenjanin, Serbia June 15th-19th 2009.

[Gre91] C. H. Greene and M. Aymar, *Spin-orbit effects in the heavy alkaline-earth atoms*, Phys. Rev. A **44**, 1773 (1991), doi:10.1103/PhysRevA.44.1773.

[Gri03] D. G. Grier, *A revolution in optical manipulation*, Nature **424**, 810 (2003), ISSN 1476-4687, doi:10.1038/nature01935.

[Gro96] L. K. Grover, *A Fast Quantum Mechanical Algorithm for Database Search*, in *Proceedings of the Twenty-eighth Annual ACM Symposium on Theory of Computing*, ACM, New York, NY, USA (1996), STOC '96, pp. 212–219, ISBN 0-89791-785-5, doi:10.1145/237814.237866.

[Gro97] L. K. Grover, *Quantum Mechanics Helps in Searching for a Needle in a Haystack*, Phys. Rev. Lett. **79**, 325 (1997), doi:10.1103/PhysRevLett.79.325.

[Gro99] L. K. Grover, *Quantum mechanical searching*, in *Proceedings of the 1999 Congress on Evolutionary Computation-CEC99 (Cat. No. 99TH8406)*, vol. 3 (1999), vol. 3, pp. 2255–2261 Vol. 3, doi:10.1109/CEC.1999.785555.

[Hï3] M. Höning, D. Muth, D. Petrosyan and M. Fleischhauer, *Steady-state crystallization of Rydberg excitations in an optically driven lattice gas*, Phys. Rev. A **87**, 023401 (2013), doi:10.1103/PhysRevA.87.023401.

[Hai69] L. K. Haines and D. H. Roberts, *One-Dimensional Hydrogen Atom*, American Journal of Physics **37**, 1145 (1969), doi:10.1119/1.1975232.

[Han14] A. M. Hankin, Y.-Y. Jau, L. P. Parazzoli, C. W. Chou, D. J. Armstrong, A. J. Landahl and G. W. Biedermann, *Two-atom Rydberg blockade using direct $6S$ to nP excitation*, Phys. Rev. A **89**, 033416 (2014), doi:10.1103/PhysRevA.89.033416.

[Har17] A. W. Harrow and A. Montanaro, *Quantum computational supremacy*, Nature **549**, 203 EP (2017).

[Har19] R. Harper and S. T. Flammia, *Fault-Tolerant Logical Gates in the IBM Quantum Experience*, Phys. Rev. Lett. **122**, 080504 (2019), doi:10.1103/PhysRevLett.122.080504.

[Has61] H. Hasegawa and R. Howard, *Optical absorption spectrum of hydrogenic atoms in a strong magnetic field*, Journal of Physics and Chemistry of Solids **21**, 179 (1961), ISSN 0022-3697, doi:https://doi.org/10.1016/0022-3697(61)90097-X.

[He90] X. He, B. Li, A. Chen and C. Zhang, *Model-potential calculation of lifetimes of Rydberg states of alkali atoms*, Journal of Physics B: Atomic, Molecular and Optical Physics **23**, 661 (1990), doi:10.1088/0953-4075/23/4/001.

[Hee12] K. P. Heeg, M. Gärttner and J. Evers, *Hybrid model for Rydberg gases including exact two-body correlations*, Phys. Rev. A **86**, 063421 (2012).

[Hel16]   S. Helmrich, A. Arias, N. Pehoviak and S. Whitlock, *Two-body interactions and decay of three-level Rydberg-dressed atoms*, Journal of Physics B: Atomic, Molecular and Optical Physics **49**, 03LT02 (2016).

[Hez06]   B. Hezel, I. Lesanovsky and P. Schmelcher, *Controlling Ultracold Rydberg Atoms in the Quantum Regime*, Phys. Rev. Lett. **97**, 223001 (2006), doi: 10.1103/PhysRevLett.97.223001.

[Hez07]   B. Hezel, I. Lesanovsky and P. Schmelcher, *Ultracold Rydberg atoms in a Ioffe-Pritchard trap*, Phys. Rev. A **76**, 053417 (2007), doi:10.1103/PhysRevA.76.053417.

[Hor90]   L. J. Hornbeck, *Deformable-Mirror Spatial Light Modulators* (1990), doi: 10.1117/12.962188.

[Hu,02]   Hu, Z., Knupfer, M., Kielwein, M., Rößler, U. K. *et al.*, *The electronic structure of the doped one-dimensional transition metal oxide Y2-xCaxBaNiO5 studied using X-ray absorption*, Eur. Phys. J. B **26**, 449 (2002), doi:10.1140/epjb/e20020113.

[Hua19]   W. Huang, C. H. Yang, K. W. Chan, T. Tanttu *et al.*, *Fidelity benchmarks for two-qubit gates in silicon*, Nature (2019), ISSN 1476-4687, doi:10.1038/s41586-019-1197-0.

[IMB]   *IMB Q Experience*, `https://quantumexperience.ng.bluemix.net/qx/editor`. Accessed: 12-4-2019.

[Ise10a] L. Isenhower, E. Urban, X. L. Zhang, A. T. Gill *et al.*, *Demonstration of a Neutral Atom Controlled-NOT Quantum Gate*, Phys. Rev. Lett. **104**, 010503 (2010), doi:10.1103/PhysRevLett.104.010503.

[Ise10b] L. Isenhower, E. Urban, X. L. Zhang, A. T. Gill *et al.*, *Demonstration of a Neutral Atom Controlled-NOT Quantum Gate*, Phys. Rev. Lett. **104**, 010503 (2010), doi:10.1103/PhysRevLett.104.010503.

[Jak00a] D. Jaksch, J. I. Cirac, P. Zoller, S. L. Rolston, R. Côté and M. D. Lukin, *Fast Quantum Gates for Neutral Atoms*, Phys. Rev. Lett. **85**, 2208 (2000), doi:10.1103/PhysRevLett.85.2208.

[Jak00b] D. Jaksch, J. I. Cirac, P. Zoller, S. L. Rolston, R. Côté and M. D. Lukin, *Fast Quantum Gates for Neutral Atoms*, Phys. Rev. Lett. **85**, 2208 (2000), doi:10.1103/PhysRevLett.85.2208.

[Jau15]   Y.-Y. Jau, A. M. Hankin, T. Keating, I. H. Deutsch and G. W. Biedermann, *Entangling atomic spins with a Rydberg-dressed spin-flip blockade*, Nature Physics **12**, 71 EP (2015). Article.

[Jon98]   J. A. Jones, M. Mosca and R. H. Hansen, *Implementation of a quantum search algorithm on a quantum computer*, Nature **393**, 344 (1998), ISSN 1476-4687, doi:10.1038/30687.

[Jur14] P. Jurcevic, B. P. Lanyon, P. Hauke, C. Hempel, P. Zoller, R. Blatt and C. F. Roos, *Quasiparticle engineering and entanglement propagation in a quantum many-body system*, Nature **511**, 202 EP (2014).

[Kan17] A. Kandala, A. Mezzacapo, K. Temme, M. Takita, M. Brink, J. M. Chow and J. M. Gambetta, *Hardware-efficient variational quantum eigensolver for small molecules and quantum magnets*, Nature **549**, 242 EP (2017).

[Kap16] M. Kaplan, G. Leurent, A. Leverrier and M. Naya-Plasencia, *Breaking Symmetric Cryptosystems Using Quantum Period Finding*, in M. Robshaw and J. Katz (eds.) *Advances in Cryptology – CRYPTO 2016*, Springer Berlin Heidelberg, Berlin, Heidelberg (2016), pp. 207–237, ISBN 978-3-662-53008-5.

[Kar17] T. Karzig, C. Knapp, R. M. Lutchyn, P. Bonderson *et al.*, *Scalable designs for quasiparticle-poisoning-protected topological quantum computation with Majorana zero modes*, Phys. Rev. B **95**, 235305 (2017), doi:10.1103/PhysRevB.95.235305.

[Kau12] A. M. Kaufman, B. J. Lester and C. A. Regal, *Cooling a Single Atom in an Optical Tweezer to Its Quantum Ground State*, Phys. Rev. X **2**, 041014 (2012), doi:10.1103/PhysRevX.2.041014.

[Kim09a] K. Kim, M.-S. Chang, R. Islam, S. Korenblit, L.-M. Duan and C. Monroe, *Entanglement and Tunable Spin-Spin Couplings between Trapped Ions Using Multiple Transverse Modes*, Phys. Rev. Lett. **103**, 120502 (2009), doi:10.1103/PhysRevLett.103.120502.

[Kim09b] K. Kim, M.-S. Chang, R. Islam, S. Korenblit, L.-M. Duan and C. Monroe, *Entanglement and Tunable Spin-Spin Couplings between Trapped Ions Using Multiple Transverse Modes*, Phys. Rev. Lett. **103**, 120502 (2009), doi:10.1103/PhysRevLett.103.120502.

[Kim10] K. Kim, M.-S. Chang, S. Korenblit, R. Islam *et al.*, *Quantum simulation of frustrated Ising spins with trapped ions*, Nature **465**, 590 EP (2010).

[Kir09a] G. Kirchmair, J. Benhelm, F. Zähringer, R. Gerritsma, C. F. Roos and R. Blatt, *Deterministic entanglement of ions in thermal states of motion*, New Journal of Physics **11**, 023002 (2009), doi:10.1088/1367-2630/11/2/023002.

[Kir09b] G. Kirchmair, J. Benhelm, F. Zähringer, R. Gerritsma, C. F. Roos and R. Blatt, *Deterministic entanglement of ions in thermal states of motion*, New Journal of Physics **11**, 023002 (2009).

[Kru02] A. Krug and A. Buchleitner, *Microwave ionization of alkali-metal Rydberg states in a realistic numerical experiment*, Phys. Rev. A **66**, 053416 (2002), doi:10.1103/PhysRevA.66.053416.

[Lab16] H. Labuhn, D. Barredo, S. Ravets, S. de Léséleuc, T. Macrì, T. Lahaye and A. Browaeys, *Tunable two-dimensional arrays of single Rydberg atoms for realizing quantum Ising models*, Nature **534**, 667 (2016), ISSN 0028-0836.

[Lad10]   T. D. Ladd, F. Jelezko, R. Laflamme, Y. Nakamura, C. Monroe and J. L. O'Brien, *Quantum computers*, Nature **464**, 45 EP (2010). Review Article.

[Lan91]   V. Lange, M. A. Khan, U. Eichmann and W. Sandner, *Rydberg states of the strontium ion*, Zeitschrift für Physik D Atoms, Molecules and Clusters **18**, 319 (1991), ISSN 1431-5866, doi:10.1007/BF01426593.

[Lan11]   B. P. Lanyon, C. Hempel, D. Nigg, M. Müller *et al.*, *Universal Digital Quantum Simulation with Trapped Ions*, Science **334**, 57 (2011), ISSN 0036-8075, doi:10.1126/science.1208001.

[LaR19]   R. LaRose, *Overview and Comparison of Gate Level Quantum Software Platforms*, Quantum **3**, 130 (2019), ISSN 2521-327X, doi:10.22331/q-2019-03-25-130.

[Lee16]   W. Lee, H. Kim and J. Ahn, *Three-Dimensional Dynamic Reconfiguration of Single-Atom Arrays Using Liquid-Crystal Spatial Light Modulator*, in *Conference on Lasers and Electro-Optics*, Optical Society of America (2016), p. FM2C.4, doi:10.1364/CLEO_QELS.2016.FM2C.4.

[Lei03]   D. Leibfried, B. DeMarco, V. Meyer, D. Lucas *et al.*, *Experimental demonstration of a robust, high-fidelity geometric two ion-qubit phase gate*, Nature **422**, 412 EP (2003).

[LeR70]   R. J. LeRoy and R. B. Bernstein, *Dissociation energies of diatomic molecules from vibrational spacings of higher levels: application to the halogens**, Chemical Physics Letters **5**, 42 (1970), ISSN 0009-2614, doi:https://doi.org/10.1016/0009-2614(70)80125-7.

[LeR74]   R. J. LeRoy, *Long-range potential coefficients from RKR turning points: C_6 and C_8 for $B(^3\Pi_{0u}{}^+)$-state Cl_3, Br_2, and I_2*, Canadian Journal of Physics **52**, 246 (1974), doi:10.1139/p74-035.

[Les05a] I. Lesanovsky and P. Schmelcher, *Magnetic Trapping of Ultracold Rydberg Atoms*, Phys. Rev. Lett. **95**, 053001 (2005), doi:10.1103/PhysRevLett.95.053001.

[Les05b] I. Lesanovsky and P. Schmelcher, *Quantum states of ultracold electronically excited atoms in a magnetic quadrupole trap*, Phys. Rev. A **72**, 053410 (2005), doi:10.1103/PhysRevA.72.053410.

[Les13]   I. Lesanovsky and J. P. Garrahan, *Kinetic Constraints, Hierarchical Relaxation, and Onset of Glassiness in Strongly Interacting and Dissipative Rydberg Gases*, Phys. Rev. Lett. **111**, 215305 (2013).

[Les14]   I. Lesanovsky and J. P. Garrahan, *Out-of-equilibrium structures in strongly interacting Rydberg gases with dissipation*, Phys. Rev. A **90**, 011603 (2014).

[Leu14]   V. Leung, D. Pijn, H. Schlatter, L. Torralbo-Campo *et al.*, *Magnetic-film atom chip with 10 μm period lattices of microtraps for quantum information science with Rydberg atoms*, Review of Scientific Instruments **85**, 053102 (2014).

[Li03] W. Li, I. Mourachko, M. W. Noel and T. F. Gallagher, *Millimeter-wave spectroscopy of cold Rb Rydberg atoms in a magneto-optical trap: Quantum defects of the ns, np, and nd series*, Phys. Rev. A **67**, 052502 (2003), doi:10.1103/PhysRevA.67.052502.

[Lim13] J. Lim, H.-g. Lee and J. Ahn, *Review of cold Rydberg atoms and their applications*, Journal of the Korean Physical Society **63**, 867 (2013), ISSN 1976-8524, doi:10.3938/jkps.63.867.

[Llo96] S. Lloyd, *Universal Quantum Simulators*, Science **273**, 1073 (1996), ISSN 00368075, 10959203.

[Lom00] S. J. J. Lomonaco (ed.), *Quantum Computation: A Grand Mathematical Challenge for the Twenty-First Century and the Millennium, Lecture Notes prepared for the American Mathematical Society short course on quantum computation held in Washington, DC January 17-18 2000*, vol. 58, American Mathematical Society (2000), ISBN 0821820842.

[Loo15] P.-F. Loos, C. J. Ball and P. M. W. Gill, *Chemistry in one dimension*, Phys. Chem. Chem. Phys. **17**, 3196 (2015), doi:10.1039/C4CP03571B.

[Lor02] T. Lorenz, M. Hofmann, M. Grüninger, A. Freimuth, G. S. Uhrig, M. Dumm and M. Dressel, *Evidence for spin-charge separation in quasi-one-dimensional organic conductors*, Nature **418**, 614 EP (2002).

[Lou59] R. Loudon, *One-Dimensional Hydrogen Atom*, American Journal of Physics **27**, 649 (1959), doi:10.1119/1.1934950.

[Lou16] R. Loudon, *One-dimensional hydrogen atom*, Proceedings of the Royal Society of London A: Mathematical, Physical and Engineering Sciences **472** (2016), ISSN 1364-5021, doi:10.1098/rspa.2015.0534.

[Luk01a] M. D. Lukin, M. Fleischhauer, R. Cote, L. M. Duan, D. Jaksch, J. I. Cirac and P. Zoller, *Dipole Blockade and Quantum Information Processing in Mesoscopic Atomic Ensembles*, Phys. Rev. Lett. **87**, 037901 (2001), doi:10.1103/PhysRevLett.87.037901.

[Luk01b] M. D. Lukin, M. Fleischhauer, R. Cote, L. M. Duan, D. Jaksch, J. I. Cirac and P. Zoller, *Dipole Blockade and Quantum Information Processing in Mesoscopic Atomic Ensembles*, Phys. Rev. Lett. **87**, 037901 (2001), doi:10.1103/PhysRevLett.87.037901.

[Lv16] H. Lv, W. Zuo, L. Zhao, H. Xu *et al.*, *Comparative study on atomic and molecular Rydberg-state excitation in strong infrared laser fields*, Phys. Rev. A **93**, 033415 (2016), doi:10.1103/PhysRevA.93.033415.

[Mal14] N. Malossi, M. M. Valado, S. Scotto, P. Huillery *et al.*, *Full Counting Statistics and Phase Diagram of a Dissipative Rydberg Gas*, Phys. Rev. Lett. **113**, 023006 (2014).

[Mal15] K. M. Maller, M. T. Lichtman, T. Xia, Y. Sun *et al.*, *Rydberg-blockade controlled-not gate and entanglement in a two-dimensional array of neutral-atom qubits*, Phys. Rev. A **92**, 022336 (2015), doi:10.1103/PhysRevA.92.022336.

[Man79] L. Mandel, *Sub-Poissonian photon statistics in resonance fluorescence*, Opt. Lett. **4**, 205 (1979), doi:10.1364/OL.4.000205.

[Mar94] M. Marinescu, H. R. Sadeghpour and A. Dalgarno, *Dispersion coefficients for alkali-metal dimers*, Phys. Rev. A **49**, 982 (1994), doi:10.1103/PhysRevA.49.982.

[May09a] M. Mayle, I. Lesanovsky and P. Schmelcher, *Exploiting the composite character of Rydberg atoms for cold-atom trapping*, Phys. Rev. A **79**, 041403R (2009), doi:10.1103/PhysRevA.79.041403.

[May09b] M. Mayle, I. Lesanovsky and P. Schmelcher, *Magnetic trapping of ultracold Rydberg atoms in low angular momentum states*, Phys. Rev. A **80**, 053410 (2009), doi:10.1103/PhysRevA.80.053410.

[McC16] J. R. McClean, J. Romero, R. Babbush and A. Aspuru-Guzik, *The theory of variational hybrid quantum-classical algorithms*, New Journal of Physics **18**, 023023 (2016), doi:10.1088/1367-2630/18/2/023023.

[McQ13] P. McQuillen, X. Zhang, T. Strickler, F. B. Dunning and T. C. Killian, *Imaging the evolution of an ultracold strontium Rydberg gas*, Phys. Rev. A **87**, 013407 (2013), doi:10.1103/PhysRevA.87.013407.

[Mit03] J. Mitroy and M. W. J. Bromley, *Semiempirical calculation of van der Waals coefficients for alkali-metal and alkaline-earth-metal atoms*, Phys. Rev. A **68**, 052714 (2003), doi:10.1103/PhysRevA.68.052714.

[Mon98] H. Monien, M. Linn and N. Elstner, *Trapped one-dimensional Bose gas as a Luttinger liquid*, Phys. Rev. A **58**, R3395 (1998), doi:10.1103/PhysRevA.58.R3395.

[Mor05] H. Moritz, T. Stöferle, K. Günter, M. Köhl and T. Esslinger, *Confinement Induced Molecules in a 1D Fermi Gas*, Phys. Rev. Lett. **94**, 210401 (2005), doi:10.1103/PhysRevLett.94.210401.

[Mül11] M. M. Müller, H. R. Haakh, T. Calarco, C. P. Koch and C. Henkel, *Prospects for fast Rydberg gates on an atom chip*, Quantum Information Processing **10**, 771 (2011), doi:10.1007/s11128-011-0296-0.

[ń17] M. Płodzień, G. Lochead, J. de Hond, N. J. van Druten and S. Kokkelmans, *Rydberg dressing of a one-dimensional Bose-Einstein condensate*, Phys. Rev. A **95**, 043606 (2017), doi:10.1103/PhysRevA.95.043606.

[Nab16] J. B. Naber, *Magnetic atom lattices for quantum information*, Ph.D. thesis, University of Amsterdam (2016). See chapter 2, section 2.3.2.

[Nei18]   C. Neill, P. Roushan, K. Kechedzhi, S. Boixo *et al.*, *A blueprint for demonstrating quantum supremacy with superconducting qubits*, Science **360**, 195 (2018), ISSN 0036-8075, doi:10.1126/science.aao4309.

[Nie11]   M. A. Nielsen and I. L. Chuang, *Quantum Computation and Quantum Information: 10th Anniversary Edition*, Cambridge University Press, New York, NY, USA, 10th edn. (2011), ISBN 1107002176, 9781107002173.

[Noe00]   M. W. Noel, W. M. Griffith and T. F. Gallagher, *Classical subharmonic resonances in microwave ionization of lithium Rydberg atoms*, Phys. Rev. A **62**, 063401 (2000), doi:10.1103/PhysRevA.62.063401.

[Nog14]   F. Nogrette, H. Labuhn, S. Ravets, D. Barredo *et al.*, *Single-Atom Trapping in Holographic 2D Arrays of Microtraps with Arbitrary Geometries*, Phys. Rev. X **4**, 021034 (2014), doi:10.1103/PhysRevX.4.021034.

[Ped03]   T. G. Pedersen, *Variational approach to excitons in carbon nanotubes*, Phys. Rev. B **67**, 073401 (2003), doi:10.1103/PhysRevB.67.073401.

[Per14]   A. Peruzzo, J. McClean, P. Shadbolt, M.-H. Yung *et al.*, *A variational eigenvalue solver on a photonic quantum processor*, Nature Communications **5**, 4213 EP (2014). Article.

[Pin00]   P. W. H. Pinkse, T. Fischer, P. Maunz and G. Rempe, *Trapping an atom with single photons*, Nature **404**, 365 EP (2000).

[Poh03]   T. Pohl, T. Pattard and J. M. Rost, *Plasma formation from ultracold Rydberg gases*, Phys. Rev. A **68**, 010703 (2003), doi:10.1103/PhysRevA.68.010703.

[Poh10]   T. Pohl, E. Demler and M. D. Lukin, *Dynamical Crystallization in the Dipole Blockade of Ultracold Atoms*, Phys. Rev. Lett. **104**, 043002 (2010), doi:10.1103/PhysRevLett.104.043002.

[Por04a] D. Porras and J. I. Cirac, *Effective Quantum Spin Systems with Trapped Ions*, Phys. Rev. Lett. **92**, 207901 (2004), doi:10.1103/PhysRevLett.92.207901.

[Por04b] D. Porras and J. I. Cirac, *Effective Quantum Spin Systems with Trapped Ions*, Phys. Rev. Lett. **92**, 207901 (2004), doi:10.1103/PhysRevLett.92.207901.

[Pre18]   J. Preskill, *Quantum Computing in the NISQ era and beyond*, Quantum **2**, 79 (2018), ISSN 2521-327X, doi:10.22331/q-2018-08-06-79.

[Pup08]   G. Pupillo, A. Griessner, A. Micheli, M. Ortner, D.-W. Wang and P. Zoller, *Cold Atoms and Molecules in Self-Assembled Dipolar Lattices*, Phys. Rev. Lett. **100**, 050402 (2008), doi:10.1103/PhysRevLett.100.050402.

[Qia13]   J. Qian, L. Zhou and W. Zhang, *Quantum phases of strongly interacting Rydberg atoms in triangular lattices*, Phys. Rev. A **87**, 063421 (2013), doi:10.1103/PhysRevA.87.063421.

[Qis]   *Qiskit AER | A high performance simulator framework for quantum circuits*, https://qiskit.org/aer. Accessed: 12-4-2019.

[Rai81]   J. M. Raimond, G. Vitrant and S. Haroche, *Spectral line broadening due to the interaction between very excited atoms: 'the dense Rydberg gas'*, Journal of Physics B: Atomic and Molecular Physics **14**, L655 (1981), ISSN 0022-3700.

[Raj11]   A. Rajaei, M. Houshmand and M. Rouhani, *Optimization of Combinational Logic Circuits Using NAND Gates and Genetic Programming*, in A. Gaspar-Cunha, R. Takahashi, G. Schaefer and L. Costa (eds.) *Soft Computing in Industrial Applications*, Springer Berlin Heidelberg, Berlin, Heidelberg (2011), pp. 405–414, ISBN 978-3-642-20505-7.

[Rec03]   A. Recati, P. O. Fedichev, W. Zwerger and P. Zoller, *Fermi one-dimensional quantum gas: Luttinger liquid approach and spin–charge separation*, Journal of Optics B: Quantum and Semiclassical Optics **5**, S55 (2003).

[Rei99]   J. Reichel, W. Hänsel and T. W. Hänsch, *Atomic Micromanipulation with Magnetic Surface Traps*, Phys. Rev. Lett. **83**, 3398 (1999), doi:10.1103/PhysRevLett.83.3398.

[Rei02]   J. Reichel, *Microchip traps and Bose–Einstein condensation*, Applied Physics B: Lasers and Optics **74**, 469 (2002), ISSN 0946-2171, doi:10.1007/s003400200861.

[Ric14]   P. Richerme, Z.-X. Gong, A. Lee, C. Senko *et al.*, *Non-local propagation of correlations in quantum systems with long-range interactions*, Nature **511**, 198 EP (2014).

[Riv78]   R. L. Rivest, A. Shamir and L. Adleman, *A Method for Obtaining Digital Signatures and Public-key Cryptosystems*, Commun. ACM **21**, 120 (1978), ISSN 0001-0782, doi:10.1145/359340.359342.

[Rob05]   F. Robicheaux and J. V. Hernández, *Many-body wave function in a dipole blockade configuration*, Phys. Rev. A **72**, 063403 (2005), doi:10.1103/PhysRevA.72.063403.

[Roo08]   C. F. Roos, *Ion trap quantum gates with amplitude-modulated laser beams*, New Journal of Physics **10**, 013002 (2008), doi:10.1088/1367-2630/10/1/013002.

[Sac00]   C. A. Sackett, D. Kielpinski, B. E. King, C. Langer *et al.*, *Experimental entanglement of four particles*, Nature **404**, 256 EP (2000).

[Saf10a]   M. Saffman, T. G. Walker and K. Mølmer, *Quantum information with Rydberg atoms*, Rev. Mod. Phys. **82**, 2313 (2010), doi:10.1103/RevModPhys.82.2313.

[Saf10b]   M. Saffman, T. G. Walker and K. Mølmer, *Quantum information with Rydberg atoms*, Rev. Mod. Phys. **82**, 2313 (2010), doi:10.1103/RevModPhys.82.2313.

[Saf16a] M. Saffman, *Quantum computing with atomic qubits and Rydberg interactions: progress and challenges*, Journal of Physics B: Atomic, Molecular and Optical Physics **49**, 202001 (2016).

[Saf16b] M. Saffman, *Quantum computing with atomic qubits and Rydberg interactions: progress and challenges*, Journal of Physics B-Atomic Molecular and Optical Physics **49** (2016), ISSN 0953-4075, doi:10.1088/0953-4075/49/20/202001.

[Sch98] A. Schwartz, M. Dressel, G. Grüner, V. Vescoli, L. Degiorgi and T. Giamarchi, *On-chain electrodynamics of metallic $(\mathrm{TMTSF})_2 X$ salts: Observation of Tomonaga-Luttinger liquid response*, Phys. Rev. B **58**, 1261 (1998), doi:10.1103/PhysRevB.58.1261.

[Sch07] U. Schmidt, I. Lesanovsky and P. Schmelcher, *Ultracold Rydberg atoms in a magneto-electric trap*, Journal of Physics B: Atomic, Molecular and Optical Physics **40**, 1003 (2007).

[Sch12] P. Schausz, M. Cheneau, M. Endres, T. Fukuhara *et al.*, *Observation of spatially ordered structures in a two-dimensional Rydberg gas*, Nature **491**, 87 (2012), ISSN 0028-0836.

[Sch14] H. Schempp, G. Günter, M. Robert-de Saint-Vincent, C. S. Hofmann *et al.*, *Full Counting Statistics of Laser Excited Rydberg Aggregates in a One-Dimensional Geometry*, Phys. Rev. Lett. **112**, 013002 (2014).

[Sea83] M. J. Seaton, *Quantum defect theory*, Reports on Progress in Physics **46**, 167 (1983), doi:10.1088/0034-4885/46/2/002.

[Sec16] T. Secker, R. Gerritsma, A. W. Glaetzle and A. Negretti, *Controlled long-range interactions between Rydberg atoms and ions*, Phys. Rev. A **94**, 013420 (2016), doi:10.1103/PhysRevA.94.013420.

[Sel18] A. Selyem, S. Fayard, T. W. Clark, A. S. Arnold, N. Radwell and S. Franke-Arnold, *Holographically controlled three-dimensional atomic population patterns*, Opt. Express **26**, 18513 (2018), doi:10.1364/OE.26.018513.

[Sha80] I. Shavitt and L. T. Redmon, *Quasidegenerate perturbation theories. A canonical van Vleck formalism and its relationship to other approaches*, The Journal of Chemical Physics **73**, 5711 (1980), ISSN 0021-9606, doi:10.1063/1.440050.

[Sha18] J. P. Shaffer, S. T. Rittenhouse and H. R. Sadeghpour, *Ultracold Rydberg molecules*, Nature Communications **9**, 1965 (2018), ISSN 2041-1723, doi:10.1038/s41467-018-04135-6.

[Shi14] S. W. Shin, G. Smith, J. A. Smolin and U. Vazirani, *How "Quantum" is the D-Wave Machine?* (2014).

[Sho94]   P. W. Shor, *Algorithms for quantum computation: discrete logarithms and factoring*, in *Proceedings 35th Annual Symposium on Foundations of Computer Science* (1994), pp. 124–134, doi:10.1109/SFCS.1994.365700.

[Sho99]   P. Shor, *Polynomial-Time Algorithms for Prime Factorization and Discrete Logarithms on a Quantum Computer*, SIAM Review **41**, 303 (1999), doi:10.1137/S0036144598347011.

[Sin04]   K. Singer, M. Reetz-Lamour, T. Amthor, L. G. Marcassa and M. Weidemüller, *Suppression of Excitation and Spectral Broadening Induced by Interactions in a Cold Gas of Rydberg Atoms*, Phys. Rev. Lett. **93**, 163001 (2004), doi:10.1103/PhysRevLett.93.163001.

[Sin05]   K. Singer, J. Stanojevic, M. Weidemüller and R. Côté, *Long-range interactions between alkali Rydberg atom pairs correlated to thens–ns,np–np andnd–nd asymptotes*, Journal of Physics B: Atomic, Molecular and Optical Physics **38**, S295 (2005), doi:10.1088/0953-4075/38/2/021.

[Sin08]   M. Singh, M. Volk, A. Akulshin, A. Sidorov, R. McLean and P. Hannaford, *One-dimensional lattice of permanent magnetic microtraps for ultracold atoms on an atom chip*, Journal of Physics B: Atomic, Molecular and Optical Physics **41**, 065301 (2008).

[Ska20]   R. Skannrup, T. van Weerden, Y. van der Werf, T. Johri, E. Vredenbregt and S. Kokkelmans, *Three-level rate equations in cold, disordered Rydberg gases*, Journal of Physics B: Atomic, Molecular and Optical Physics **53** (2020), ISSN 0953-4075, doi:10.1088/1361-6455/ab7525.

[Sø99]   A. Sørensen and K. Mølmer, *Quantum Computation with Ions in Thermal Motion*, Phys. Rev. Lett. **82**, 1971 (1999), doi:10.1103/PhysRevLett.82.1971.

[Sø00]   A. Sørensen and K. Mølmer, *Entanglement and quantum computation with ions in thermal motion*, Phys. Rev. A **62**, 022311 (2000), doi:10.1103/PhysRevA.62.022311.

[Ste76]   R. F. Stebbings, *High Rydberg Atoms: Newcomers to the Atomic Physics Scene*, Science **193**, 537 (1976), ISSN 0036-8075, doi:10.1126/science.193.4253.537.

[Ste96]   A. M. Steane, *Error Correcting Codes in Quantum Theory*, Phys. Rev. Lett. **77**, 793 (1996), doi:10.1103/PhysRevLett.77.793.

[Suz98]   Y. Suzuki, Y. S. K. Varga, M. Suzuki and K. Varga, *Stochastic Variational Approach to Quantum-Mechanical Few-Body Problems*, no. v. 54 in Lecture Notes in Physics Monographs, Springer (1998), ISBN 9783540651529.

[Suz03]   Y. Suzuki and K. Varga, *Stochastic Variational Approach to Quantum-Mechanical Few-Body Problems*, Lecture Notes in Physics Monographs, Springer Berlin Heidelberg (2003), ISBN 9783540495413.

[SV13]   M. Robert-de Saint-Vincent, C. S. Hofmann, H. Schempp, G. Günter, S. Whitlock and M. Weidemüller, *Spontaneous Avalanche Ionization of a Strongly Blockaded Rydberg Gas*, Phys. Rev. Lett. **110**, 045004 (2013), doi:10.1103/PhysRevLett.110.045004.

[The84]   C. E. Theodosiou, *Lifetimes of alkali-metal—atom Rydberg states*, Phys. Rev. A **30**, 2881 (1984), doi:10.1103/PhysRevA.30.2881.

[Tho10]   W. Thomson, Baron Kelvin, *NINETEENTH CENTURY CLOUDS OVER THE DYNAMICAL THEORY OF HEAT AND LIGHT*, Cambridge University Press, p. 486–527, Cambridge Library Collection - Physical Sciences (2010), doi:10.1017/CBO9780511694523.026.

[Top14]   T. Topcu and A. Derevianko, *Divalent Rydberg atoms in optical lattices: Intensity landscape and magic trapping*, Phys. Rev. A **89**, 023411 (2014), doi:10.1103/PhysRevA.89.023411.

[Tur37]   A. M. Turing, *On Computable Numbers, with an Application to the Entscheidungsproblem*, Proceedings of the London Mathematical Society **s2-42**, 230 (1937), doi:10.1112/plms/s2-42.1.230.

[Urb09]   E. Urban, T. A. Johnson, T. Henage, L. Isenhower, D. D. Yavuz, T. G. Walker and M. Saffman, *Observation of Rydberg blockade between two atoms*, Nat Phys **5**, 110 (2009), ISSN 1745-2473.

[Urv15]   A. Urvoy, F. Ripka, I. Lesanovsky, D. Booth, J. P. Shaffer, T. Pfau and R. Löw, *Strongly Correlated Growth of Rydberg Aggregates in a Vapor Cell*, Phys. Rev. Lett. **114**, 203002 (2015), doi:10.1103/PhysRevLett.114.203002.

[Val16]   M. M. Valado, C. Simonelli, M. D. Hoogerland, I. Lesanovsky *et al.*, *Experimental observation of controllable kinetic constraints in a cold atomic gas*, Phys. Rev. A **93**, 040701 (2016).

[Van01]   L. M. K. Vandersypen, M. Steffen, G. Breyta, C. S. Yannoni, M. H. Sherwood and I. L. Chuang, *Experimental realization of Shor's quantum factoring algorithm using nuclear magnetic resonance*, Nature **414**, 883 (2001), ISSN 1476-4687, doi:10.1038/414883a.

[Vil20]   B. Villalonga, D. Lyakh, S. Boixo, H. Neven *et al.*, *Establishing the quantum supremacy frontier with a 281 Pflop/s simulation*, Quantum Science and Technology **5**, 034003 (2020), doi:10.1088/2058-9565/ab7eeb.

[Wag10]   C. Wagner and N. Harned, *Lithography gets extreme*, Nature Photonics **4**, 24 EP (2010).

[Wal08]   T. G. Walker and M. Saffman, *Consequences of Zeeman degeneracy for the van der Waals blockade between Rydberg atoms*, Phys. Rev. A **77**, 032723 (2008), doi:10.1103/PhysRevA.77.032723.

[Wan01]   X. Wang, A. Sørensen and K. Mølmer, *Multibit Gates for Quantum Computing*, Phys. Rev. Lett. **86**, 3907 (2001), doi:10.1103/PhysRevLett.86.3907.

[Wan16]   Y. Wang, P. Surendran, S. Jose, T. Tran *et al.*, *Magnetic lattices for ultracold atoms and degenerate quantum gases*, Science Bulletin **61**, 1097 (2016), ISSN 2095-9273, doi:https://doi.org/10.1007/s11434-016-1123-x.

[Wan17]   Y. Wang, T. Tran, P. Surendran, I. Herrera *et al.*, *Trapping ultracold atoms in a sub-micron-period triangular magnetic lattice*, Phys. Rev. A **96**, 013630 (2017), doi:10.1103/PhysRevA.96.013630.

[Wee17]   T. H. P. van Weerden, *Spontaneous crystallization in a one-dimensional Rydberg system*, Master's thesis, Eindhoven University of Technology (2017).

[Wei08a] H. Weimer, R. Löw, T. Pfau and H. P. Büchler, *Quantum Critical Behavior in Strongly Interacting Rydberg Gases*, Phys. Rev. Lett. **101**, 250601 (2008), doi:10.1103/PhysRevLett.101.250601.

[Wei08b] H. Weimer, R. Löw, T. Pfau and H. P. Büchler, *Quantum Critical Behavior in Strongly Interacting Rydberg Gases*, Phys. Rev. Lett. **101**, 250601 (2008), doi:10.1103/PhysRevLett.101.250601.

[Wei10]   H. Weimer, M. Müller, I. Lesanovsky, P. Zoller and H. P. Büchler, *A Rydberg quantum simulator*, Nature Physics **6**, 382 (2010), ISSN 1745-2481, doi:10.1038/nphys1614.

[Wer17]   Y. van der Werf, *Spatial Structures and Strong Interactions in Ultracold Rydberg Gases*, Master's thesis, Eindhoven University of Technology (2017).

[Whi09]   S. Whitlock, R. Gerritsma, T. Fernholz and R. Spreeuw, *Two-dimensional array of microtraps with atomic shift register on a chip*, New Journal of Physics **11**, 023021 (2009).

[Wil10a] T. Wilk, A. Gaëtan, C. Evellin, J. Wolters, Y. Miroshnychenko, P. Grangier and A. Browaeys, *Entanglement of Two Individual Neutral Atoms Using Rydberg Blockade*, Physical Review Letters **104**, 010502+ (2010), doi:10.1103/physrevlett.104.010502.

[Wil10b] T. Wilk, A. Gaëtan, C. Evellin, J. Wolters, Y. Miroshnychenko, P. Grangier and A. Browaeys, *Entanglement of Two Individual Neutral Atoms Using Rydberg Blockade*, Phys. Rev. Lett. **104**, 010502 (2010), doi:10.1103/PhysRevLett.104.010502.

[Win98]   D. J. Wineland, C. Monroe, W. M. Itano, D. Leibfried, B. E. King and D. M. Meekhof, *Experimental Issues in Coherent Quantum-State Manipulation of Trapped Ions*, Journal of Research of the National Institute of Standards and Technology **103**, 259 (1998), doi:10.6028/jres.103.019.

[Wul06]   K. D. Wulff, D. G. Cole, R. L. Clark, R. DiLeonardo *et al.*, *Aberration correction in holographic optical tweezers*, Opt. Express **14**, 4169 (2006), doi:10.1364/OE.14.004169.

[Wun81] G. Wunner and H. Ruder, *Hydrogen atom in strong magnetic fields - Polynomial approximations for the magnetic-field dependence of the energy values*, aap **95**, 204 (1981).

[Xu10] P. Xu, X. He, J. Wang and M. Zhan, *Trapping a single atom in a blue detuned optical bottle beam trap*, Opt. Lett. **35**, 2164 (2010), doi:10.1364/OL.35.002164.

[Ye99] J. Ye, D. W. Vernooy and H. J. Kimble, *Trapping of Single Atoms in Cavity QED*, Phys. Rev. Lett. **83**, 4987 (1999), doi:10.1103/PhysRevLett.83.4987.

[Yoo07] S. Yoon, Y. Choi, S. Park, W. Ji, J.-H. Lee and K. An, *Characteristics of single-atom trapping in a magneto-optical trap with a high magnetic-field gradient*, Journal of Physics: Conference Series **80**, 012046 (2007).

[Yu14] S.-P. Yu, J. D. Hood, J. A. Muniz, M. J. Martin *et al.*, *Nanowire photonic crystal waveguides for single-atom trapping and strong light-matter interactions*, Applied Physics Letters **104**, 111103 (2014), doi:10.1063/1.4868975.

[Zha10] X. L. Zhang, L. Isenhower, A. T. Gill, T. G. Walker and M. Saffman, *Deterministic entanglement of two neutral atoms via Rydberg blockade*, Phys. Rev. A **82**, 030306 (2010), doi:10.1103/PhysRevA.82.030306.

[Zha11] S. Zhang, F. Robicheaux and M. Saffman, *Magic-wavelength optical traps for Rydberg atoms*, Phys. Rev. A **84**, 043408 (2011), doi:10.1103/PhysRevA.84.043408.

[Zha17] J. Zhang, G. Pagano, P. W. Hess, A. Kyprianidis *et al.*, *Observation of a many-body dynamical phase transition with a 53-qubit quantum simulator*, Nature **551**, 601 EP (2017).

[Zim79] M. L. Zimmerman, M. G. Littman, M. M. Kash and D. Kleppner, *Stark structure of the Rydberg states of alkali-metal atoms*, Phys. Rev. A **20**, 2251 (1979), doi:10.1103/PhysRevA.20.2251.

[Zup16] P. Zupancic, P. M. Preiss, R. Ma, A. Lukin *et al.*, *Ultra-precise holographic beam shaping for microscopic quantum control*, Opt. Express **24**, 13881 (2016), doi:10.1364/OE.24.013881.

[Zwi00] F. Zwick, W. Henderson, L. Degiorgi, M. Grioni, G. Gruner, L. K. Montgomery and V. Vescoli, *Optical and photoemission evidence for a Tomonaga-Luttinger liquid in the Bechgaard salts*, European Physical Journal B **13**, 503 (2000).

Curiculum vitæ

Rasmus Vestergaard Skannrup, born in Skanderborg on the 17th of December 1986

<table>
<tr>
<td>2007-2011</td>
<td>

Bachelor of Science in Physics
Aarhus University
Bachelor project: Space-time Geometry in the Vicinity of a Rotating Black Hole

</td>
</tr>
<tr>
<td>2011-2017</td>
<td>

Master of Science in Physics
Aarhus University
Master's thesis: Correlated Gaussian Approach to Cold Atoms in a One Dimensional Double Well Trap

</td>
</tr>
<tr>
<td>2014-2020</td>
<td>

PhD candidate
Coherence and Quantum Technology research group
Department of Applied Physics
Eindhoven University of Technology

</td>
</tr>
</table>

List of publications

Published

A. G. Boetes, R. V. Skannrup, J. Naber, S. J. J. M. F. Kokkelmans and R. J. C. Spreeuw, *Trapping of Rydberg atoms in tight magnetic microtraps*, Phys. Rev. A **97**, 013430 (2018).

R. V. Skannrup, T. van Weerden, Y. van der Werf, T. Johri, E. J. D. Vredenbregt and S. J. J. M. F. Kokkelmans, *Three-level rate equations in cold, disordered Rydberg gases*, Journal of Physics B: Atomic, Molecular and Optical Physics **53** (2020).

In preparation

R. V. Skannrup, R. Gerritsma and S. J. J. M. F. Kokkelmans, *Phonon-mediated spin-spin interactions between trapped Rydberg atoms*, submitted for publication in Phys. Rev. A (2020).

R. V. Skannrup, E. J. D. Vredenbregt and S. J. J. M. F. Kokkelmans *Controlled Quantum Plasmas Created from Rydberg Crystals*, in preparation.

Presentations

A. G. Boetes, R. V. Skannrup, J. Naber, S. J. J. M. F. Kokkelmans and R. J. C. Spreeuw, *Trapping of Rydberg atoms in tight magnetic microtraps*, presented at NNV AMO Lunteren 2017.

A. G. Boetes, R. V. Skannrup, J. Naber, S. J. J. M. F. Kokkelmans and R. J. C. Spreeuw, *Trapping of Rydberg atoms in tight magnetic microtraps*, presented at Physics@Veldhoven 2018.

Index

"

...There is another theory which states that this has already happened.

Douglas Adams

"